ADAPTIVE FEEDFORWARD CONTROL OF BROADBAND STRUCTURAL VIBRATION

by

Jeffrey S. Vipperman

Thesis submitted to the Faculty of the

Virginia Polytechnic Institute and State University

in partial fulfillment of the requirements for the degree of

Master of Science

in

Mechanical Engineering

APPROVED:

_____
Dr. Chris R. Fuller, Chairman

_____   _____
Dr. Ricardo A. Burdisso   Dr. Harry H. Robertshaw

June, 1992

Blacksburg, Virginia

LD

V566

ADAPTIVE FEEDFORWARD CONTROL OF BROADBAND STRUCTURAL VIBRATION

by

Jeffrey S. Vipperman

Committee Chairman: Chris R. Fuller
Mechanical Engineering

(ABSTRACT)

Active control of noise and vibration has been previously demonstrated in finite and infinite systems undergoing single and multiple-frequency excitations. Control of broadband noise and vibration has also been reported, but it tends to be limited to infinite and semi-infinite systems. Here, four new adaptive feedforward control algorithms were developed for attenuating the response generated by finite structural systems. The algorithms are based on the filtered-X Least Mean Square (LMS) adaptive algorithm. A system identification of the plant control loop is required to implement this algorithm. An autoregressive moving-average (ARMA) model was used for the system identification since it provides the most computationally-efficient means of representing the frequency response function (FRF) of a lightly-damped structure. In the first control system, an adaptive finite impulse response (FIR) or nonrecursive filter was used as the compensator. A second control approach was realized by employing a recursive compensator. These two algorithms were modified using an equation error minimization technique to form two additional control systems, which eliminate certain stability requirements of the ARMA system identification. Each algorithm was simulated and then demonstrated experimentally.

Lastly, an analysis of control system causality was developed to determine the importance of this topic with regard to controlling finite structural systems. A exemplary parametric study of one of the four control systems presented, will demonstrate the analytical tool by examining the effects of system damping, compensator order, and a time delay in the control path, which is responsible for acausal control solutions. It was determined that control is always achievable, despite a delay in the control path, and also that control system performance can be improved by increasing the order of the control compensator. Both of these results were verified experimentally.

Acknowledgements

I would like thank my major professor, Dr. Chris Fuller, for the opportunity to get this degree, his helpful suggestions, and most of all for providing such a stimulating project for me. Also, I express tremendous appreciation for Dr. Ricardo Burdisso for all of the help, patience, and information he has provided for me during the course of my research. I would also like to acknowledge Dr. Harry Robertshaw and Dr. Bill Baumann for their helpful discussions. Many thanks to fellow students for their assistance and friendship: Will Saunders, Robert Wynn, Rob Clark, Cathy Guigu, Bertrand Brevart, Chris White, and many others who are not named. Last, a very special thanks to my best friend Cori for her patience and support throughout my degree.

Contents

List of Figures

List of Tables

Chapter 1

Introduction

Over the past decade, active control methods have become recognized as a viable means of attenuating structural vibration and its associated sound radiation. The principle behind active control is adding "secondary" controlled source(s) in order to cancel the response generated by the "primary" or disturbance input. There are two basic control approaches: feedback and feedforward as shown in Figure 1.1. The error signal, e_k, in either system is formed from the superposition of the responses, d_k and y_k, from the disturbance and control inputs, respectively. Note that T_{ne} in Figures 1.1(a) and (b) represents the plant transfer function between the disturbance input and the error sensor. Likewise, T_{ce} represents the transfer function of the control loop from the plant. Feedback control (Figure 1.1(a)) is characterized by feeding one or more measured or estimated system states back through a compensator, G_c, to form the control signal, u_k [1, 2, 3]. An augmentation of the system natural properties allows control of both transient and steady-state disturbances. In feedforward control, the control input, u_k, is computed by passing a reference signal which is coherent to the disturbance signal through a compensator, G_c, and
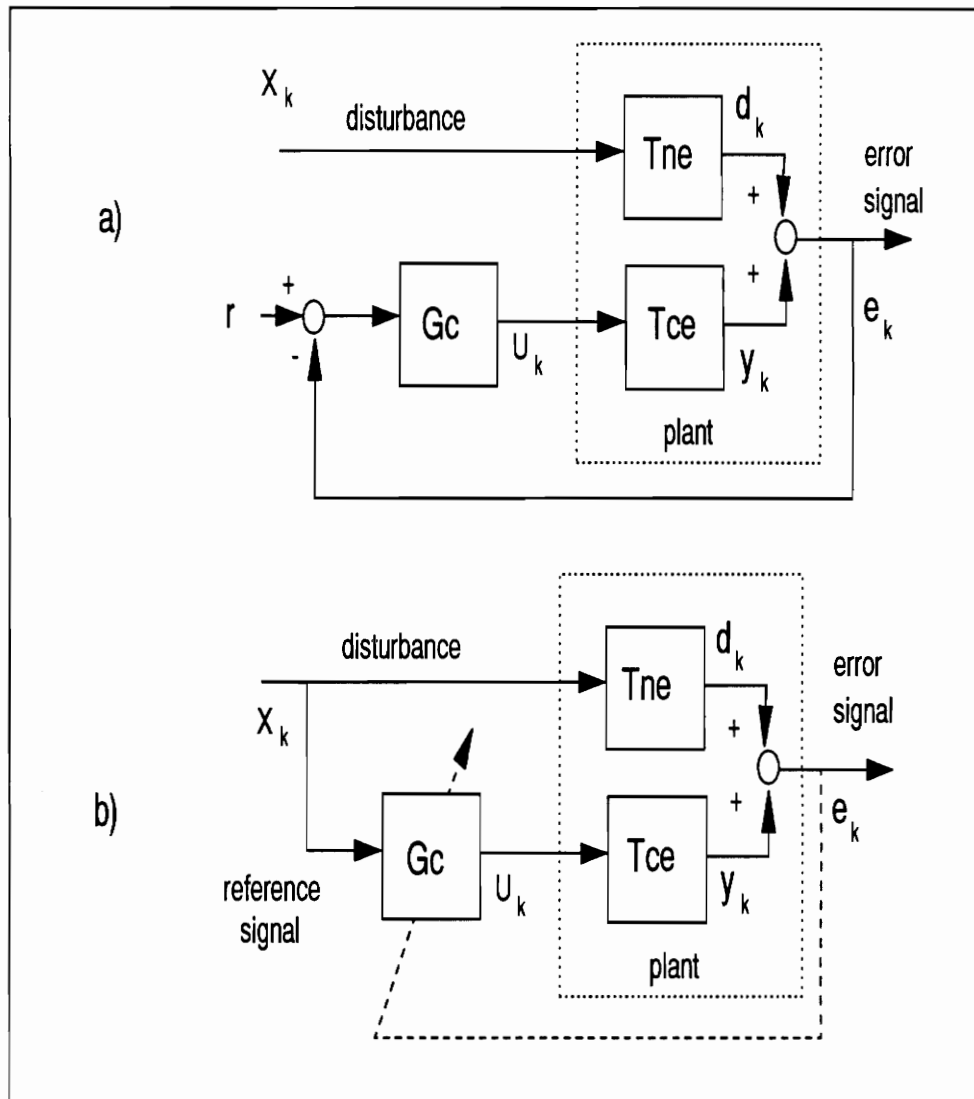
Figure 1.1: Schematic diagram of two basic control approaches: a) feedback only and b) adaptive feedforward.

into the structure (Figure 1.1(b)). The compensator is typically a linear digital filter which is typically designed by minimizing a quadratic cost function formed by squaring the error signal and taking its expectation. Often, as shown by the dashed arrow in Figure 1.1(b), the error signal is used in a recursion equation to adapt the coefficients of the compensator (in real time) until the minimum mean square error (MSE) is found. The sum of the mean-square values of the output of a number of sensors can also be used as the cost function in multi-input multi-output (MIMO) systems. Adaptive feedforward algorithms have proven successful for applications in which the disturbance is stationary such as single and multiple frequencies, and random inputs.

Initial application of feedforward control was to one-dimensional acoustics fields as summarized in the review article by Warnaka [4]. More recently the technique has been extended to multi-dimensional acoustic acoustic fields [5] as well as control of structurally radiated noise [6]. Feedforward least-mean-square (LMS) and recursive-least-mean-square (RLMS) adaptive algorithms have been applied on active control of bending motion in infinite or semi-infinite thin beams [7, 8, 9, 10, 11]. Recently, the simultaneous control of flexural and extensional waves in beams has been demonstrated by a multi-channel LMS approach, in conjunction with specialized piezoceramic transducers [12]. Most theoretical and experimental studies consider only single and multiple sinusoidal excitations. Applications of feedforward control for broad-band excitation are much more scarce and restricted for attenuating noise in ducts [13, 14, 15] and enclosures [16]. Broadband structural control has been demonstrated with feedback and state-space methods, where designs are typically based on damping augmentation (direct velocity feedback) or wave ab-

3

sorption [8]. Reports of feedforward, broadband structural control are scarce and are characterized using infinitely long structures that have no reflected power which occurs from boundary conditions [9]. Consequently, the response to the disturbance can be measured at a location on the structure before the error sensor, providing exact, apriori knowledge of the error signal to be cancelled. In addition, the previous implementations of feedforward, broadband controllers for noise and structural vibration have transfer functions between the control input and the error sensor which are relatively flat in magnitude response, allowing them to be easily represented by a fairly low-order finite impulse response (FIR) filter.

Here, four new adaptive single-input, single-output (SISO) feedforward control configurations for the active control of broad-band vibration for a finite structure are developed and investigated. Each control system is based on the filtered-X LMS algorithm where an autoregressive moving-average (ARMA) model is used for the system identification of the control loop. An ARMA model, often referred to as an infinite impulse response (IIR) digital filter, was used because its pole-zero structure provides the most compact means of representing a structural frequency response function (FRF), but it complicates the control system because IIR filters have certain stability requirements which must be met [17, 18]. The parameters of the ARMA model were found by forming a least-squares (LS) solution combined with a variation of the recursive least mean square (RLMS) algorithm [17, 19, 20].

In the first control system, an adaptive finite impulse response (FIR) (or nonrecursive) filter was used as the compensator. A second control structure differed

4

by using a recursive (IIR) filter for the compensator. Alternate configurations of these two systems provide two more control approaches which provide a means of eliminating the stability requirements of the ARMA system identification. These systems are based on the equation error minimization technique, [17, 19] where the error signal is filtered before minimizing it.

One important topic of broadband feedforward control is system causality. From Figure 1.1(b), an 'acausal' control system can result when the propagation time of the reference signal, x_k, through the compensator G_c and the control-loop T_{ce} exceeds the propagation time of x_k through the disturbance loop, T_{ne} [16, 21, 22, 23]. In this text, the *system* will be referred to as 'acausal' since the optimal control filter will have an output which is dependant upon future inputs, rendering the unit sample response [24] to be acausal. The delay or wave propagation time in the control response, y_k, will depend on the locations of the control actuator and error sensor, the signal processing time in G_c, and the dynamics of the additional control hardware (e.g. power amplifiers, filters, etc.). The delay in the disturbance response, d_k, will be dependent on the physics of T_{ne}. By careful selection of the sensor/actuator locations in order to delay the disturbance input with respect to the reference signal, a causal control system can often be achieved. Achieving causality is often difficult in active vibration control (AVC) because: 1) physical dimensions are usually limited, 2) Often the exact source of the disturbance is unknown, and 3) propagation times of the signals are extremely fast compared to acoustic waves in air. Early experiments suggested that causality was not a critical issue for finite structures since sufficient levels of control were achieved with a causal approximation of an acausal controller. An analytical tool was developed to investigate the effects of acausality of feedforward control systems applied to finite elastic systems.

5

Results from a numerical study on one of the control systems which investigated system damping, the order of the control compensator, and the effects of delaying the control signal input (simulating an acausal system) will be presented and compared to experimental observations.

The controllers were implemented in a digital signal processing (DSP) board and experimental results for a simply-supported beam are presented. The delay times through the disturbance and control paths to the error output were measured so that an additional delay could be introduced into the disturbance path, if needed, to guarantee that the controller would be causal. The control performance of the Filtered-X LMS Control Configuration was evaluated for different size adaptive FIR filters. The same analysis was repeated for an acausal control system, where the disturbance-path delay was removed.

This document is organized with the theoretical development of the control algorithms located in the first few chapters followed by the experimental investigations and causality analysis. Chapter 2 contains the theory of adaptive signal processing and how it is expanded to plant control using the filtered-X LMS algorithm. A simulation of each proposed control algorithm is also presented. Chapter 3 discusses the system identification of the control loop using a least-squares (LS) solution for an autoregressive moving-average (ARMA) model to model the plant. In chapter 4, the experimental design is presented along with a description of the test rig, followed by the experimental results which are contained in chapter 5. An analysis of control system causality was carried out in chapter 6 to determine the

influence of a control-path delay. A parametric study of various system parameters will be compared with observed experimental behavior. Finally, the conclusions from this research can be found in chapter 7 along with recommendations for improvement and further research of this topic. Information about how the plant and control algorithms were simulated is contained in Appendix A. Appendix B is included to provide detailed information on the integration of the transfer functions that comprise the causality analysis in chapter 6.

Chapter 2

Adaptive Signal Processing and Control

The availability of fast, affordable, digital signal processing (DSP) chips over the past decade has made applications using adaptive signal processing feasible. Adaptive signal processing has been applied in filter syntheses, plant modelling, noise cancellation and adaptive control [17]. The technique adds flexibility to a system by allowing it to respond or 'adapt' to changing conditions, making it beneficial for control applications where the operating environments and disturbances may change with time.

2.1   Adaptive FIR filters

Figure 2.1(a) shows a single-input, single-output (SISO) adaptive linear combiner, which is essentially a finite impulse response (FIR) filter with adaptable coefficients. The output of the filter u_k can be written as convolution of the unit sample response

of the filter, w_k, and the input sequence x_k as follows [24]

$$u_k = w_k * x_k = x_k * w_k \qquad (2.1)$$

where the $*$ operator denotes a convolution. The filter sample response is a finite, right-handed sequence such the equation (2.1) can be written as the following convolution sum [24]

$$u_k = \sum_{i=0}^{N} w_i x_{k-i} \qquad (2.2)$$

This convolution sum can also be conveniently written in terms of vectors as

$$u_k = \{W\}^T \{X\}_k = \{W\}\{X\}_k^T \qquad (2.3)$$

where

$N =$ order of the filter

$\{W\}^T = \{w_0, w_1, w_2, \ldots, w_{N-1}, w_N\}$

$\{X\}_k^T = \{x_k, x_{k-1}, x_{k-2}, \ldots, x_{k-N+1}, x_{k-N}\}$

If the adaptive filter is of adequate order, its output can closely match the desired signal, d_k, when there is high coherence function between the filter input x_k and d_k in Figure 2.1(b). In fact, the maximum achievable reduction of the error signal power is related to the coherence between x_k and d_k as follows [25]

$$\text{Max.Reduction(dB)} = 10 \log(\frac{1}{1 - \gamma_{xd}^2}) \qquad (2.4)$$

where γ_{xd}^2 is the coherence between the reference signal, x_k, and desired signal d_k. The reader should note that the filter required to meet the upper performance limit specified by equation (2.4) may not be physically realizable [25].

9
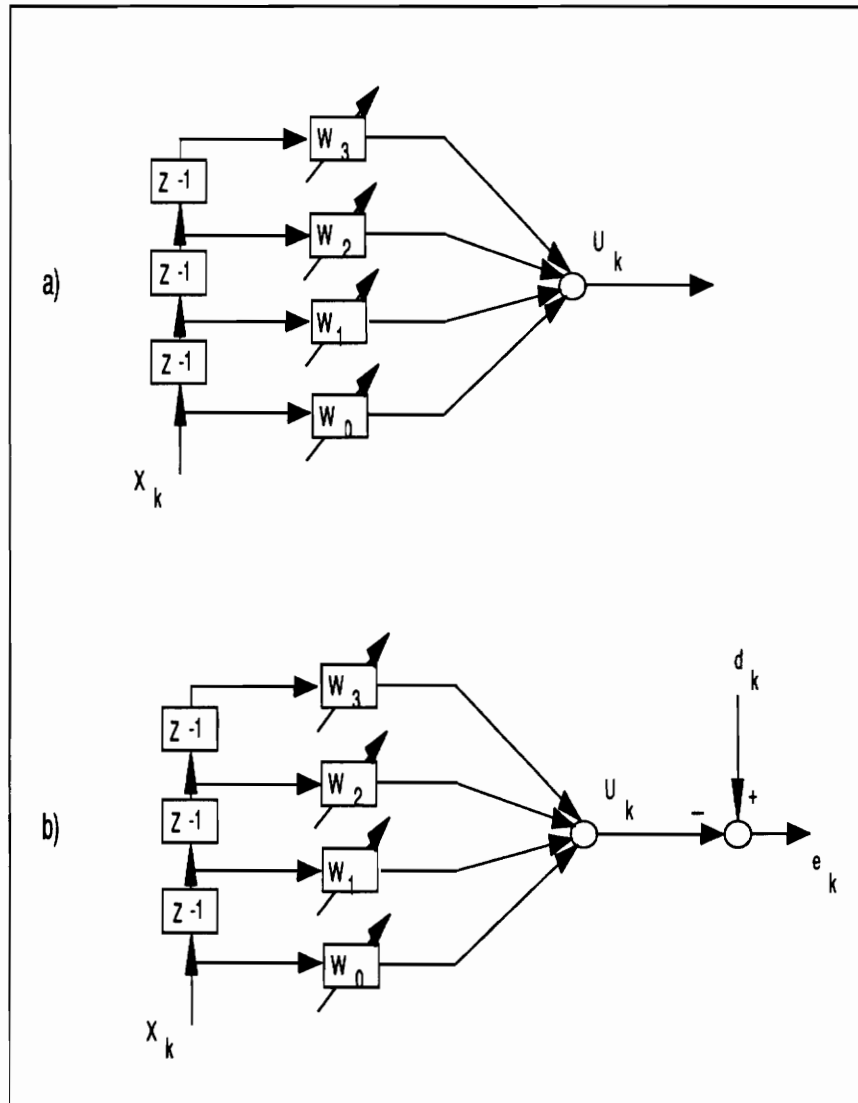
Figure 2.1: a) Adaptive FIR filter, b) Adaptive FIR configuration used to produce desired response, d_k from coherent input, x_k and drive the error, e_k to zero.

The error signal from Figure 2.1(b) can be written in terms of the desired response and the filter output as follows

$$e_k = d_k - y_k \tag{2.5}$$

$$e_k = d_k - \{W\}^T\{X\}_k \tag{2.6}$$

which goes to zero when the filter output matches the desired response. Assuming a stationary signal, the optimal weight vector, W^*, which minimizes the error signal can be found by first squaring equation (2.6) and taking the expected value to form a quadratic cost function, $\mathbf{C}$, in terms of the filter weights

$$\mathbf{C} = \mathbf{E}[e_k^2] \tag{2.7}$$

$$\mathbf{C} = \mathbf{E}[(d_k - \{W\}^T\{X\}_k)^2] \tag{2.8}$$

where $\mathbf{E}[\ ]$ denotes the expected value operator. An example of the performance surface for a two variable system described by equation (2.8) is shown in Figure 2.2 as a paraboloid. This function has a unique minimum which can be found by taking the partial derivative of equation (2.8) with respect to the weight vector and equating the result with zero

$$\frac{\partial \mathbf{C}}{\partial\{W\}} = \frac{\partial}{\partial\{W\}}\mathbf{E}[(d_k - \{W\}^T\{X\}_k)^2] \tag{2.9}$$

We now assume e_k to be stationary, allowing the partial to be moved inside the expectation operator

$$\frac{\partial \mathbf{C}}{\partial\{W\}} = 2\mathbf{E}[-d_k\{X\}_k + 2\{X\}_k\{X\}_k^T\{W\}] \tag{2.10}$$

$$0 = -\{P\} + [R]\{W\} \tag{2.11}$$

11

where

$\{P\}$ = the cross correlation vector between the filter input and output

$[R]$ = the input autocorrelation matrix

Equation (2.11) can now be solved for the optimal filter vector that will minimize the error signal

$$\{W\}^* = [R]^{-1}\{P\} \qquad (2.12)$$

Solving the linear system of equations in equation (2.12) can be computationally intensive, making a real-time implementation impractical. One solution is to create a recursion equation that will minimize the error signal, such as the method of steepest descent [17, 26]. Here, the filter weights are adapted by marching a small step along the negative gradient of the performance surface (like the one shown in Figure 2.2), until the minimum is found. That is,

$$\{W\}(k+1) \; = \; \{W\}(k) - \mu \nabla \mathbf{C} \qquad (2.13)$$

where

k = discrete time step

$\nabla \mathbf{C}$ = gradient vector of the cost function

μ = step size

The step size, μ, controls the stability and convergence rate of the update equation (2.13). The stability limits on μ can be computed from the largest eigenvalue of the input correlation matrix of equation (2.11). Therefore, a good estimate
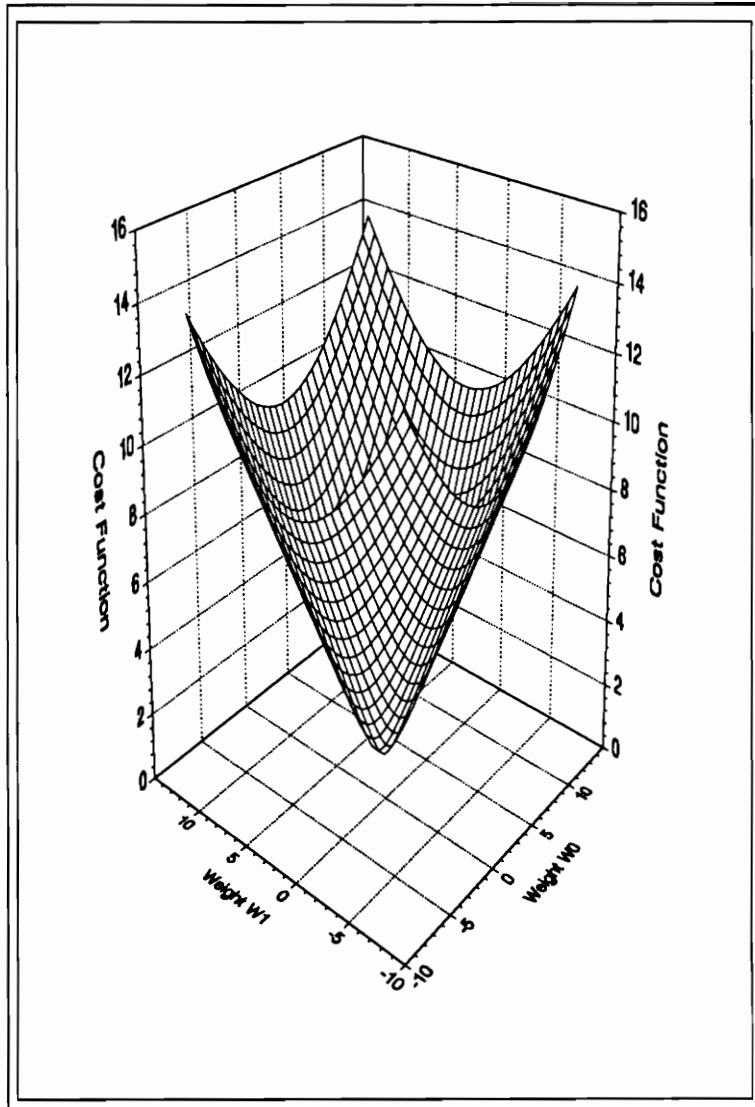
Figure 2.2: Quadratic performance surface of the cost function for two filter coefficients.

of the convergence parameter can be made from the power of the reference signal, x_k [17, 27].

The simplest and most popular method of steepest descent uses the Least Mean Square (LMS) algorithm. In the LMS algorithm, the gradient in equation (2.13) is approximated with the instantaneous values of the error and input signals as follows

$$\nabla \mathbf{C} = \frac{\partial \mathbf{C}}{\partial \{W\}} = 2\mathbf{E}[e_k \frac{\partial e_k}{\partial \{W\}}] \tag{2.14}$$

$$= 2\mathbf{E}[e_k \{-X\}_k] \tag{2.15}$$

$$\approx -2e_k \{X\}_k \tag{2.16}$$

Substituting equation (2.16) into equation (2.13) yields the final form of the weight update equation, known as the Widrow-Hoff LMS algorithm [26, 28]

$$\{W\}(k+1) = \{W\}(k) + 2\mu e_k \{X\}_k \tag{2.17}$$

or for a single coefficient, w_i,

$$w_i(k+1) = w_i(k) + 2\mu e_k x_{k-i} \tag{2.18}$$

The second term of equation (2.18), $2\mu e_k x_{k-i}$, represents the change in the ith filter coefficient, δw_i. Note that δw_i becomes smaller as the minimum is approached because the error signal is diminishing. For a constant rate of convergence, μ should increase as e_k decreases.

14

2.2 Adaptive IIR Filters Using Equation Error Minimization

Often FIR filters of practical length do not provide an adequate impulse response for the job at hand. The solution is to use infinite impulse response (IIR) filters like the one shown in Figure 2.3, which has both a feedforward and a feedback section. IIR filters are also referred to as autoregressive moving-average or ARMA models. Since the filter output is based on the input sequence as well as the past filter output values, the impulse response will be infinite in duration. The frequency response of an IIR filter is more easily shaped because it contains both poles and zeros. As long as the system order is known, an IIR filter can compactly and efficiently model transfer functions having the characteristic sharp resonance-peaks associated with lightly-damped structures. What can be represented with only a few coefficients in an IIR filter will often take hundreds of coefficients for an FIR [18], making the computational overhead impractical. The disadvantage of using IIR filters is that they have a certain stability requirement which must be met. This problem will be addressed after the filter equations are developed.

The filter output, y_k can be written in terms of the input x_k and the filter coefficients b_i and a_i that can be seen in Figure 2.3(a).

$$y_k = (a_0 + a_1 z^{-1} + \ldots + a_N z^{-N})x_k + (b_1 z^{-1} + \ldots + b_M z^{-M})y_k \qquad (2.19)$$

$$y_k = \frac{(a_0 + a_1 z^{-1} + \ldots + a_N z^{-N})}{1 - (b_1 z^{-1} + \ldots + b_M z^{-M})}x_k \qquad (2.20)$$

$$y_k = \frac{A(z)}{1 - B(z)}x_k \qquad (2.21)$$
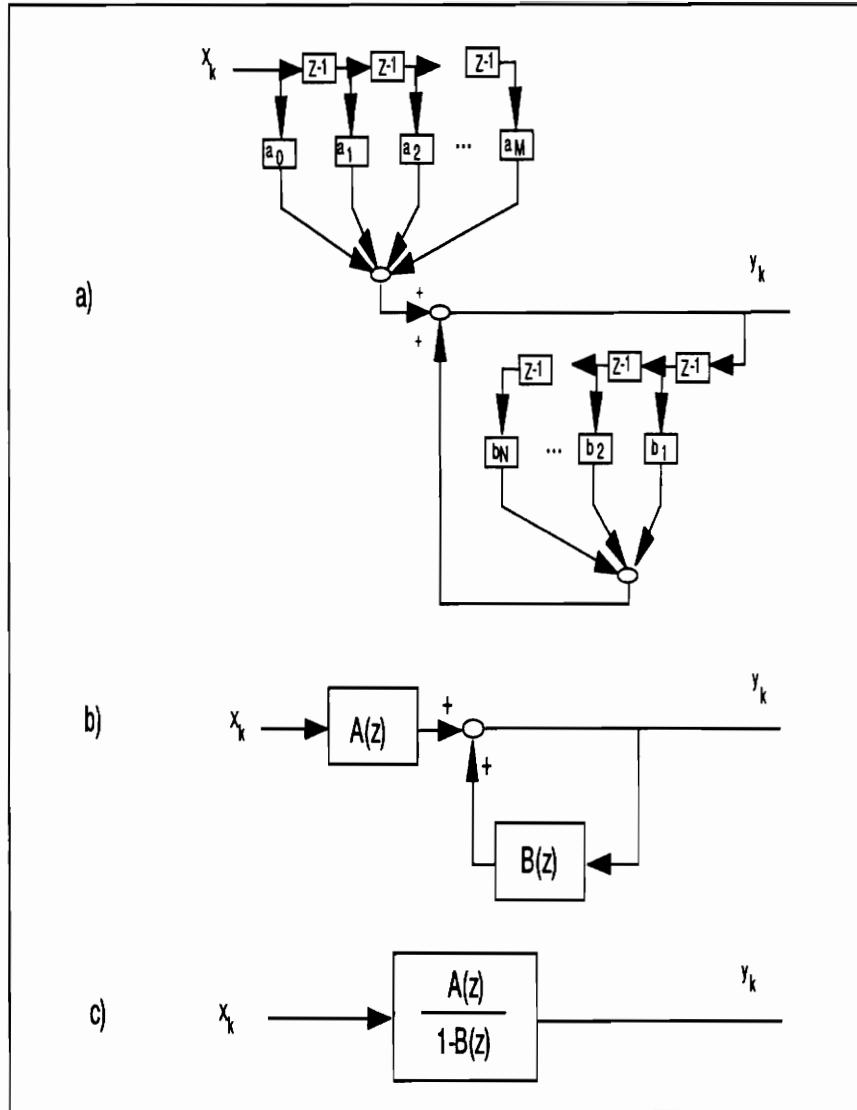
Figure 2.3: IIR filter a) Showing construction of feedforward and feedback sections with delay taps; b) simplified polynomial structure; c) ARMA transfer function of the IIR filter.

Each root of the filter poles must lie inside the unit circle in the complex z-plane or the filter output will not be bounded for a bounded input. The filter poles can be checked by factoring the polynomial $(1 - B(z))$ and ensuring that the modulus of each root is less than unity.

The LMS algorithm can be used to adapt recursive filters [15, 17, 19, 20, 29], but left in their conventional form, they pose some problems. First, the cost function is not a quadratic function of the filter weights, $A(z)$ and $B(z)$, meaning that the performance surface may have more than one minimum. Also, as mentioned, the poles of the filter $(1 - B(z))$ must remain inside the unit circle for the filter output to remain bounded. One solution to these problems is to use the equation error minimization technique for adapting IIR filters [17, 20, 29]. Shown in Figure 2.4 is an equation error adaptive IIR filter that can adaptively determine the coefficients of an ARMA model for an unknown plant. The output error is first filtered with the system poles, $(1 - B(z))$, before it is minimized, allowing the separation of the feedforward and feedback sections of the filter. Each section is then adapted as independent transversal filters, each having its own quadratic error surface. The output error signal is given as the difference between the plant output d_k, and the predicted plant response from the recursive filter, $\hat{y}_k$. That is,

$$e_k = d_k - \hat{y}_k \tag{2.22}$$

$$e_k = d_k - (\sum_{n=0}^{N_A} a_n x_{k-n} + \sum_{n=1}^{N_B} b_n \hat{y}_{k-n}) \tag{2.23}$$

where $(N_A + 1)$ is the number of feedforward coefficients and N_B is the number of feedback filter coefficients. Taking the z-transform [24] of both sides of equa-
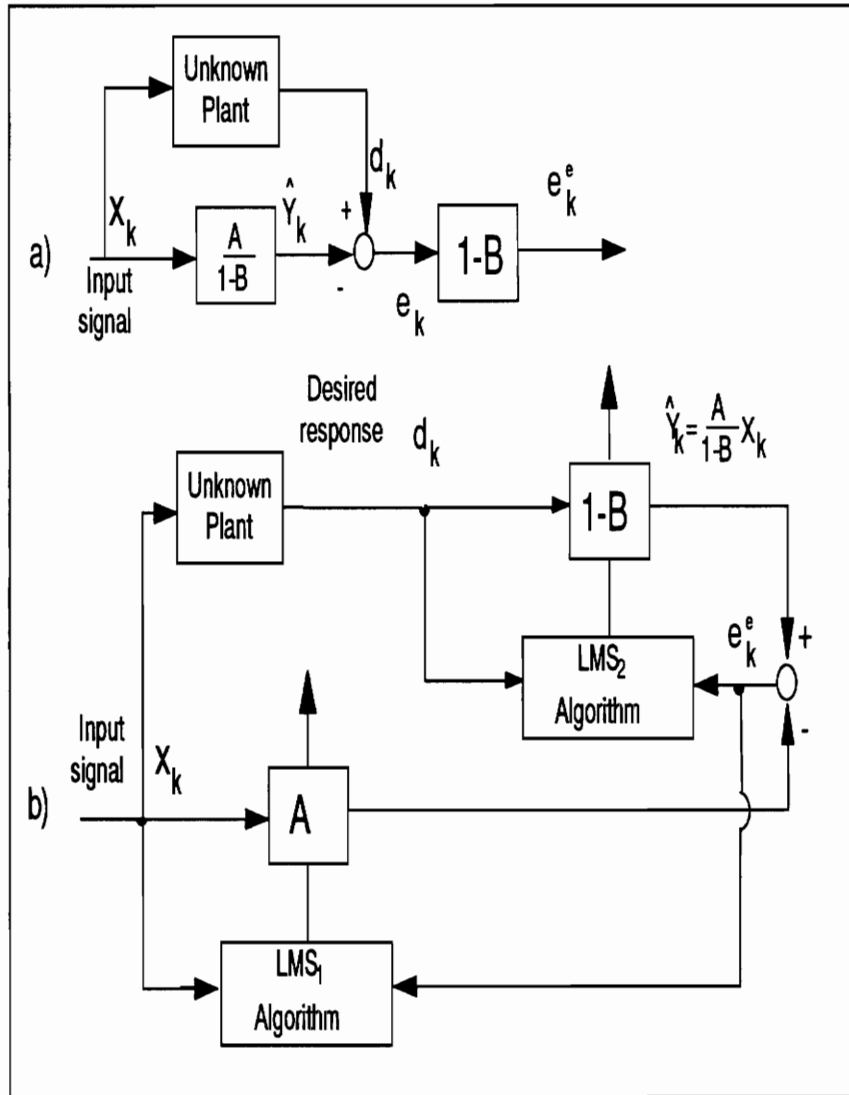
Figure 2.4: Schematic showing equation error adaptation of an IIR filter to produce a desired response, d_k.

tion (2.23) yields

$$\mathcal{Z}\{e_k\} = \mathcal{Z}\{d_k - \sum_{n=0}^{N_A} a_n x_{k-n} + \sum_{n=1}^{N_B} b_n \hat{y}_{k-n}\} \tag{2.24}$$

$$E(z) = D(z) - \frac{A(z)}{1 - B(z)} X(z) \tag{2.25}$$

where $\mathcal{Z}\{\}$ is the z-transform operator. Multiplying equation (2.25) by the poles of the filter, $(1 - B(z))$, the desired filtered equation error, $E^e(z)$, becomes

$$E^e(z) = D(z)(1 - B(z)) - A(z)X(z) \tag{2.26}$$

By taking the inverse z-transform of equation (2.26), the time domain difference equation for the equation error signal becomes

$$e_k^e = d_k - \sum_{n=1}^{N_B} b_n d_{k-n} - \sum_{n=0}^{N_A} a_n x_{k-n} \tag{2.27}$$

The cost function to be minimized is the expected mean-square-value (MSV) of e_k^e

$$\mathbf{C}(a_i, b_i) = \mathbf{E}[(e_k^e)^2] \tag{2.28}$$

$$\mathbf{C}(a_i, b_i) = \mathbf{E}[(d_k - \sum_{n=1}^{N_B} b_n d_{k-n} - \sum_{n=0}^{N_A} a_n x_{k-n})^2] \tag{2.29}$$

Equation (2.29) can be recognized as a quadratic function of the filter coefficients from both the zeros and the poles of the adaptive IIR filter. One can now perform a gradient search to update the filter coefficients a_i and b_i as described by equation (2.13). Again, the partial derivatives of the cost function are taken with respect each filter weight. The gradient and its instantaneous approximation for the coefficient b_i will be

$$\frac{\partial \mathbf{C}}{\partial b_i} = 2\mathbf{E}[e_k^e \frac{\partial e_k^e}{\partial b_i}]$$

$$= 2\mathbf{E}[e_k^e(-d_{k-i})]$$

19

$$\approx \quad -2e_k^e d_{k-i} \qquad\qquad (2.30)$$

where e_k^e is the instantaneous equation error from equation (2.27) and d_{k-i} is the desired response of the filter.

Similarly, the gradient for the numerator coefficients can be approximated as follows

$$\begin{aligned}
\frac{\partial \mathbf{C}}{\partial a_i} &= 2\mathbf{E}[e_k^e \frac{\partial e_k^e}{\partial a_i}] \\
&= 2\mathbf{E}[e_k^e(-x_{k-i})] \\
&\approx -2e_k^e x_{k-i} \qquad\qquad (2.31)
\end{aligned}$$

where x_k is the input disturbance sequence to the adaptive filter and desired plant, which is typically zero-mean, band-limited white noise.

Considering equation (2.13) with equations (2.30), and (2.31) we can construct the final form of the Widrow-Hoff equations for the system identification as follows

$$\begin{aligned}
b_i(k+1) &= b_i(k) + 2\mu_B e_k^e d_{k-i} \qquad\qquad (2.32) \\
a_i(k+1) &= a_i(k) + 2\mu_A e_k^e x_{k-i} \qquad\qquad (2.33)
\end{aligned}$$

where μ_A and μ_B are the convergence parameters used in updating the numerator and denominator coefficients, respectively. These parameters may differ since the two updating processes are independent.

20

The disadvantage of using Equation Error minimization technique is that minimizing the equation error does not always minimize the error signal itself. The literature suggests that using a filter of 'adequate' size to filter the error signal will cause the error signal itself to be reduced whenever the equation or filtered error signal is reduced [17].

Although the roots of $(1 - B(z))$ are not required to remain inside the unit circle in the z-complex plane during the equation error adaptation process, they must be stable before implementing the filter in the form shown in Figure 2.3. An unstable filter can be remedied using a technique called reciprocation [17], a process where each unstable root is reflected inside the unit circle by dividing it into unity. This process approximately preserves the magnitude information of the filters frequency response, but drastically alters the phase response. Stabilization of the filter in real-time can be aided by breaking the polynomial $(1 - B(z))$ into second order filter sections and configuring them into cascade form [29]. Then, the stability of each individual filter can be guaranteed by requiring the coefficients to remain inside the region of stability as shown in Ref. [17, pp.160–1]. However, the cascade form results in a much more complex system identification algorithm with an associated significant computational effort.

2.3 Filtered-X LMS Adaptive Control

Whenever LMS algorithm is applied in control applications, such as disturbance rejection in structures, the filtering effect of the controlled plant must be taken into

account before the gradient of equation (2.13) can be estimated. The net result, as will be seen later, is that the transfer function of the control-path must be estimated before implementing the adaptive controller. The resulting algorithm for plant control is referred to as the Filtered-X LMS algorithm [17, 30]. This algorithm is the basis of the four previously-mentioned control algorithms. In section 2.3.1, the two control systems which incorporate a nonrecursive compensator will be developed, followed by the development of the recursive control systems in section 2.3.2.

2.3.1 Nonrecursive FIR Compensator

2.3.1.1 Conventional Filtered-X LMS Configuration

A typical block diagram of a SISO filtered-x LMS control structure is shown in Figure 2.5. The plant output denoted as the error signal, e_k, is the combination of the response due to the disturbance input, x_k, and the control input, u_k. That is,

$$e_k = d_k + y_k \qquad (2.34)$$

where the subscript k indicates a signal sample at time t_k. The response due to the control input in equation (2.34) can be replaced in terms of the control sequence u_k as

$$e_k = d_k + T_{ce}(k) * u_k \qquad (2.35)$$

where $T_{ce}(k)$ is the unit sample response of the transfer function between the control input and its response at the error sensor, y_k. $T_{ce}(k)$ represents a causal, shift-invariant system such that the convolution can be found from the following

convolution sum [24]

$$T_{ce}(k) * u_k = \sum_{n=0}^{\infty} T_{ce}(n) u_{k-n} \qquad (2.36)$$

The control sequence, u_k, is obtained here by filtering a reference signal that is coherent to the disturbance signal through an adaptive FIR filter. It is assumed throughout this document that the reference signal is obtained by directly tapping from the disturbance signal as shown in Figure 2.5. Thus, the control sequence becomes

$$u_k = w_k * x_k \qquad (2.37)$$
$$u_k = \sum_{n=0}^{N} w_k x_{k-n} \qquad (2.38)$$

Replacing equation (2.37) into equation (2.35), the error output is given as

$$e_k = d_k + T_{ce}(k) * w_k * x_k \qquad (2.39)$$

Again, the LMS algorithm adapts the coefficients $w_i (i = 0, 1, \ldots, N)$ in order to minimize a quadratic cost function of the plant response. The the cost function is defined as

$$\mathbf{C}(w_i) = \mathbf{E}[e_k^2] \qquad (2.40)$$

Substituting equations (2.38) and (2.39) into equation (2.40) gives

$$\mathbf{C}(w_i) = \mathbf{E}[\{d_k + T_{ce}(k) * (\sum_{i=0}^{N} w_i x_{k-i})\}^2] \qquad (2.41)$$

The cost function, and thus the error signal, is again minimized using a

23
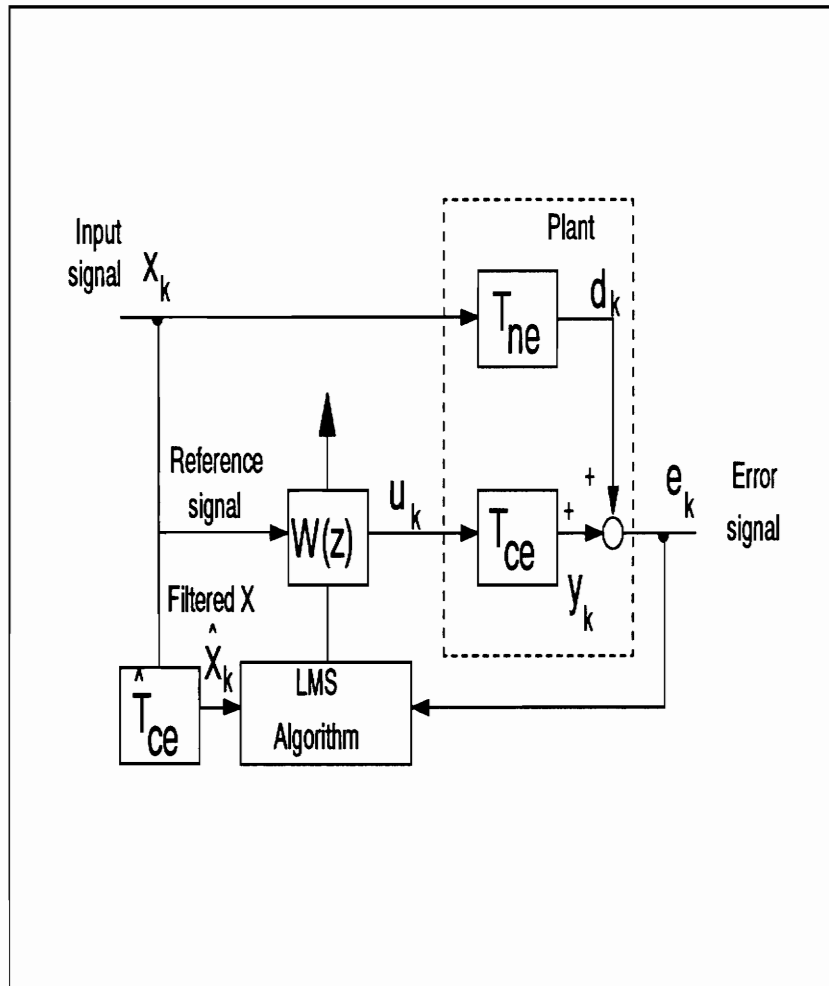
Figure 2.5: Schematic of the Filtered-X LMS adaptive control algorithm.

gradient descent technique. Differentiating the cost function in equation (2.40) with respect to a single weight, w_i, produces

$$\frac{\partial C}{\partial w_i} = 2\mathbf{E}[e_k \frac{\partial e_k}{\partial w_i}] \tag{2.42}$$

$$= 2\mathbf{E}[e_k T_{ce}(k) * x_{k-i}] \tag{2.43}$$

$$\approx 2e_k \hat{x}_{k-i} \tag{2.44}$$

where, for a shift-invariant system [24]

$$\hat{x}_{k-i} = T_{ce}(k) * x_{k-i} \tag{2.45}$$

using the right-shift theorem [31]. The sequence $\hat{x}_k$ is referred to as the filtered - x signal, and is generated by filtering the reference signal, x_k, by an estimate of the control loop transfer function, $\hat{T}_{ce}(z)$. The final update for the filtered-X LMS algorithm is

$$w_i(k+1) = w_i(k) - 2\mu e_k \hat{x}_{k-i} \quad i = 1, \ldots, N \tag{2.46}$$

where the convergence parameter μ can be estimated from the power of the filtered reference signal, $\hat{x}_k$ [27, 17].

For the adaptive linear combiner presented earlier, the output of the adaptive filter was subtracted from the desired response to form the error signal. In contrast, the error signal for the Filtered-X LMS control is formed by the summation of the desired response with the output of the adaptive filter after having been filtered by the plant control loop, T_{ce}. This transfer function must be taken into account for the reference sequence, x_k, to be correctly correlated with the error signal, e_k, in the

coefficient update equation (2.46) [17]. Otherwise, the correct gradient of the cost function will not be computed. An off-line system identification of the control-path was performed for the experimental implementation of the control systems. The system identification will be discussed further in chapter 3.

Since the plant is a linear, time-invariant structure with light damping, the transfer function T_{ce} can be most efficiently represented by an ARMA model. Such a model can best represent the resonances and anti-resonances typical of this type of structural frequency response function because it has both poles and zeros

$$T_{ce} = \frac{A}{(1 - B)} \tag{2.47}$$

The ARMA model is implemented as an IIR digital filter of the form

$$\hat{T}_{ce}(z) = \frac{\hat{A}(z)}{(1 - \hat{B}(z))} = \frac{\hat{Y}(z)}{U(z)} \tag{2.48}$$

$$\hat{T}_{ce}(z) = \frac{\sum_{i=0}^{N} \hat{A}_i z^{-i}}{(1 - \sum_{j=1}^{N} \hat{B}_j z^{-j})} \tag{2.49}$$

where $\hat{A}(z)$ and $\hat{B}(z)$ are polynomials in the complex variable z. The convolution sum resulting from the inverse z-transform of equation (2.48) can be written as

$$\hat{y}_k = \sum_{n=0}^{N_A} a_n u_{k-n} \sum_{n=1}^{N_B} b_n \hat{y}_{k-n} \tag{2.50}$$

Note that the infinite summation in equation (2.36) can be be achieved by a finite, compact summation when using an IIR digital filter.

Now, substituting equations (2.38) and (2.50) into equation (2.39), the error signal becomes

$$e_k = d_k + \sum_{n=0}^{N_A} a_n \sum_{m=0}^{N} w_m x_{k-n-m} + \sum_{n=1}^{N_B} b_n \hat{y}_{k-n} \tag{2.51}$$

26

For the filtered-x signal, $\hat{x}_k$, to be bounded such that the control algorithm will be stable, the measured transfer function, $\hat{T}_{ce}(z)$, must be stable. The stability of this filter is guaranteed if all of the measured poles, given by the roots of $(1 - \hat{B}(z))$ in equation (2.48), remain inside the unit circle in the complex z-plane.

2.3.1.2 Equation Error Control Configuration

The fact that the poles of the system represent global system properties can be taken advantage of to develop a second control configuration that will eliminate the stability requirements introduced by the IIR filter used in the Filtered-X LMS Control Configuration. As shown in Figure 2.6, the output of the plant is first filtered by the measured poles of the system, $(1 - \hat{B}(z))$, and then the LMS algorithm is used to minimize the filtered error signal rather than the error signal itself. Such a filtered version of the error signal is often referred to as equation error, hence the name Equation Error Filtered-x LMS Control Configuration. Typically, equation error forms are used to counter convergence problems of adaptive IIR filters as discussed in section 2.2.

The new error signal to be minimized is most easily represented in the z-domain. Taking the z-transform of equation (2.39) yields

$$E(z) \;=\; [D(z) + T_{ce}(z)W(z)]X(z) \tag{2.52}$$

The equation error signal can now be formed by multiplying equation (2.52) by the
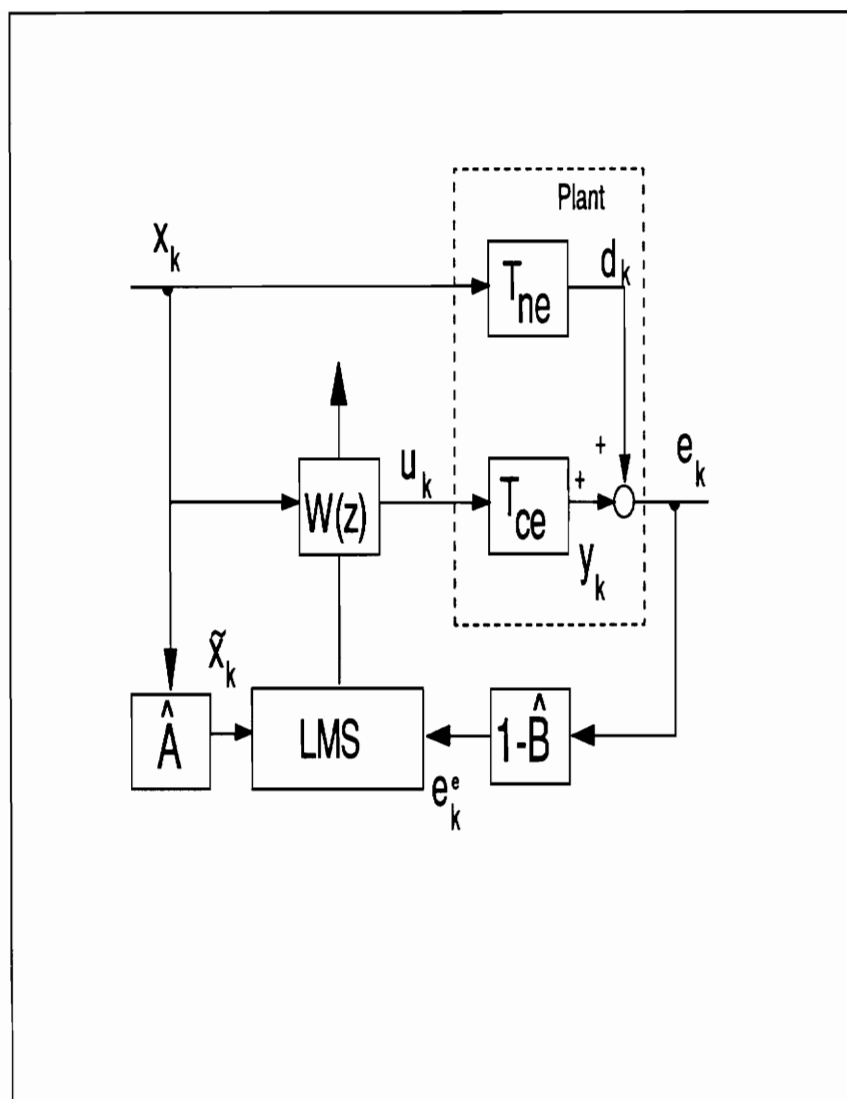
Figure 2.6: Schematic diagram of the filtered-x LMS equation error control configuration

estimated poles of the system, $(1 - \hat{B}(z))$

$$E^e(z) = [1 - \hat{B}(z)][D(z) + T_{ce}(z)W(z)]X(z) \tag{2.53}$$

The transfer function between the noise or disturbance signal x_k and its response d_k can be expressed as

$$T_{ne}(z) = \frac{C(z)}{(1 - B(z))}. \tag{2.54}$$

Thus, equation (2.53) can be also written as

$$E^e(z) = (1 - \hat{B}(z)) \left[\frac{C(z)}{1 - B(z)} + \frac{A(z)}{1 - B(z)} W(z) \right] X(z) \tag{2.55}$$

If an exact identification of the system poles is assumed equation (2.55) simplifies to

$$E^e(z) = [C(z) + A(z)W(z)] X(z) \tag{2.56}$$

which has the following discrete-time difference equation when the inverse z-transform is taken

$$e_k^e = \sum_{n=0}^{N_C} c_n x_{k-n} + \sum_{n=1}^{N_A} a_n \sum_{m=0}^{N} w_m x_{k-n-m} \tag{2.57}$$

where $(N_C + 1)$ is the number of coefficients in $C(z)$. Due to noise in the measurement and variation in the system's properties, in practice exact cancellation of poles and zeros is rarely possible. However, according to Kuo [32], the transient response of the compensated system will hardly be affected by residuals left from 'inexact' cancellation of the poles and zeros. Unfortunately, there was no quantification of his statement. However, the adaptive LMS algorithm was shown to tolerate errors in the system identification for harmonic control [30, 33] and similar error

tolerance was observed experimentally when operating the broadband controller. It was observed empirically that the natural frequencies of $\hat{T}_{ce}$ must be accurately represented within 5% to control that particular mode, where phase information was not important. This behavior is attributed to the robust nature of the LMS algorithm. Equation (2.56) shows that by forward filtering the output of the plant with $(1 - \hat{B}(z))$, the effect of the system poles are cancelled in the signal e_k^e. The reader should notice that this control structure is only possible because again, the poles $(1 - B(z))$ represent global properties of the system (i.e. natural frequencies and modal damping).

The update equation for the adaptive filter coefficients is obtained with the same process as before, except the cost function is created from the filtered error signal in equation (2.56).

$$\mathbf{C}(w_i) \;=\; \mathbf{E}[(e_k^e)^2] \tag{2.58}$$

Differentiating equation (2.58) with respect to the weight, w_i, and considering equation (2.56)

$$\frac{\partial \mathbf{C}}{\partial w_i} \;=\; 2\mathbf{E}[e_k^e \frac{\partial e_k^e}{\partial w_i}] \tag{2.59}$$

$$\;=\; 2\mathbf{E}[e_k^e a_k \tilde{*} x_{k-i}] \tag{2.60}$$

where

$$\tilde{x}_{k-i} = \hat{a}_k * x_{k-i} \tag{2.61}$$

is the filtered-x signal required to compute the gradient and $\hat{a}_k$ is the unit sample

response of the feedforward portion of the filter $T_{ce}(z)$. This signal is obtained by filtering the disturbance signal with only the zeros of the measured transfer function of $\hat{T}_{ce}(z)$. Then, using instantaneous values to approximate expected values of the gradient, the update equation for w_i now becomes

$$W_i(k+1) \quad = \quad W_i(k) - 2\mu e_k^e \tilde{x}_{k-i} \qquad i = 1, \ldots, N \qquad (2.62)$$

The main advantage of this configuration is that two inherently-stable FIR filters are used to replace the potentially unstable IIR filter used for $T_{ce}(z)$ in the Conventional Filtered-X LMS controller. Thus, the stability requirements of the system identification are removed since the filtered-X signal $\tilde{x}_k$ will always be bounded, even when some or all of the poles of $\hat{T}_{ce}(z)$ are outside the unit circle. Such a result is useful for systems that apply a simultaneous on-line system identification and control. On-line system identification is carried out by injecting an additional, uncorrelated random signal into the control path while operating an LMS or RLMS algorithm in a typical system identification arrangement [21, 34, 35]. After updating the coefficients of $\hat{T}_{ce}(z)$, they are copied to the LMS algorithm and used to create the filtered-x signal. Stabilization of the recursive filter coefficients is not required when employing the Equation Error Control Configuration, reducing both the system complexity and computational overhead.

Again, this configuration is disadvantaged because a filtered version of the error signal is minimized instead of the error signal itself. However, according to reference [17] if the filter $(1 - B(z))$ is of adequate size, then minimizing e_k^e also minimizes e_k.

2.3.2 Recursive IIR Compensator

Taking another look at Figure 2.5, the z-transform of the plant error signal can be written in terms of the transfer functions and the z-transform of the input signal, $X(z)$ as follows

$$E(z) \quad = \quad [T_{ne}(z) + W(z)T_{ce}(z)]X(z) \tag{2.63}$$

Because the cost function is quadratic and has only a single solution for the minimum, the optimal compensator $W(z)^*$ which will make equation (2.63) equal to zero can be determined from inspection as

$$W(z)^* \quad = \quad -\frac{T_{ne}(z)}{T_{ce}(z)} \tag{2.64}$$

Substituting equations (2.48) from page 26 and (2.54) from page 29 into equation (2.64) yields

$$W(z)^* \quad = \quad -\frac{C(z)}{A(z)} \tag{2.65}$$

since the poles are common to both transfer functions and they cancel. What equation (2.65) reveals is that optimal filter solution has an ARMA structure which could only be crudely approximated by the low-order FIR compensator in section 2.3.1. Full attenuation of the error signal is possible with an IIR compensator provided it is of adequate order (of equal or greater order of $C(z)$ and $A(z)$ in equation (2.65)) and all of the zeros of $A(z)$ are inside the unit circle.

Figure 2.7 shows a diagram of the filtered-X LMS algorithm which uses an adaptive recursive compensator, having poles represented by the polynomial

32

$(1 - Q(z))$. There are many problems connected with adapting the poles of IIR filters that would deter one from using them. First, left in their conventional form IIR filters produce a nonquadratic, multi-modal cost function of which it is difficult to find the global minimum. Also, the poles must be factored and checked for stability which requires significant computational effort. Further, the convergence tends to be more sensitive to noise in the gradient. The equation error technique from section 2.2 could be used to avoid stability problems, but there will be some bias error introduced into the solution. However, another inspection of equation (2.65) reveals that an IIR compensator with adaptable poles could be avoided since the polynomial $A(z)$ is the zeros of the transfer function $T_{ce}(z)$ and they are measured before the controller is implemented. Therefore the poles of the compensator should be assigned such that

$$1 - Q(z) \quad \propto \quad \hat{A}(z) \tag{2.66}$$

which can be achieved by the following equation

$$Q(z) \quad = \quad \sum_{j=1}^{N} -\frac{\hat{a}_j}{\hat{a}_0} z^{-j} \tag{2.67}$$

$$Q(z) \quad = \quad \frac{\hat{A}(z)}{\hat{a}_0} - 1 \tag{2.68}$$

or

$$1 - Q(z) \quad = \quad \frac{1}{a_0}[A(z)] \tag{2.69}$$

By assigning the poles of the compensator to be proportional to $A(z)$, the problems associated with adapting IIR filters are avoided. The control system has only a single LMS algorithm with much nicer convergence properties than would be possible

33
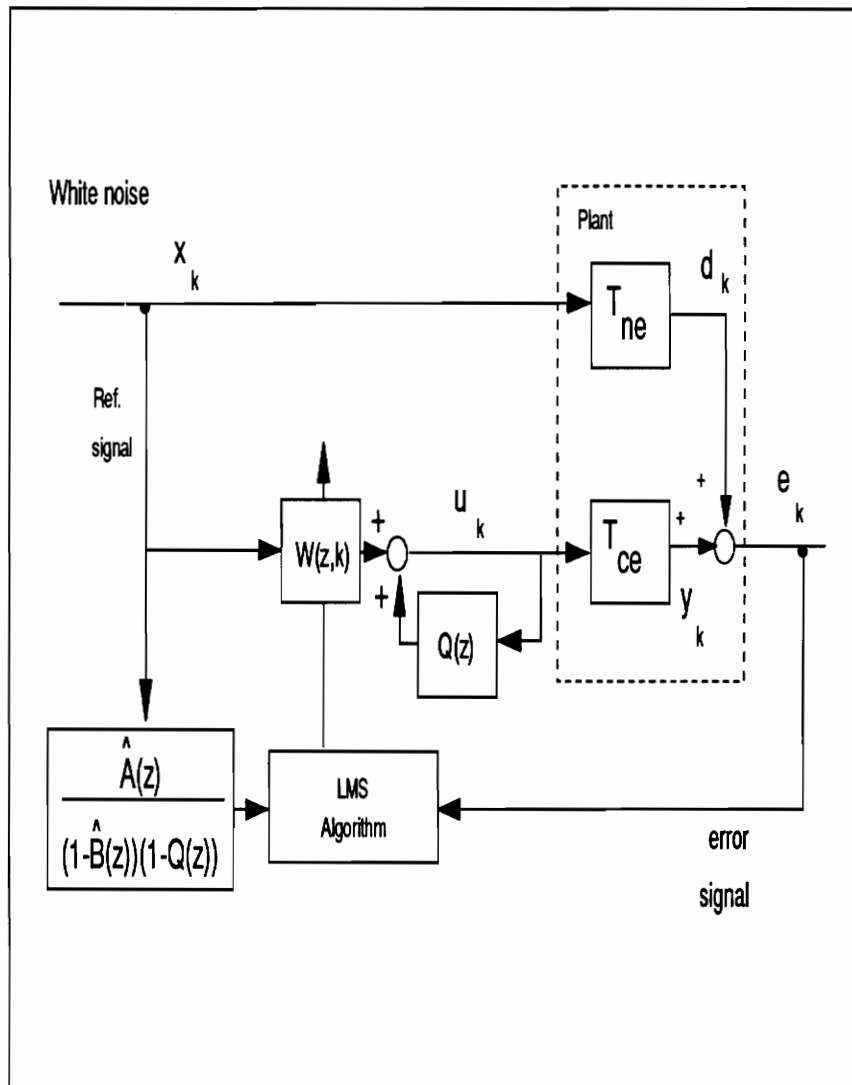
Figure 2.7: Schematic showing the filtered-X LMS adaptive plant control using a recursive filter as a compensator.

34

with an RLMS algorithm. The disadvantage of the method is that the roots of $A(z)$ must all lie inside the unit circle for the compensator output to be bounded. If the zeros of $T_{ce}(z)$, or the roots of $A(z)$, are all inside the unit circle, then the system is said to be a minimum-phase system, and a stable inverse exists. Nonminimum-phase systems occur naturally in cases where actuator and sensor are not colocated. A nonminimum-phase system may also result from discretizing a minimum-phase plant for digital implementation and is independent of the sampling rate [36]. For the analysis, it will be assumed that the $T_{ce}(z)$ is a minimum-phase transfer function.

The error signal in Figure 2.7 can be written as follows

$$e_k = d_k + y_k \qquad (2.70)$$

$$e_k = \mathcal{Z}^{-1}\left\{[T_{ne}(z) + \frac{W(z)}{1 - Q(z)}T_{ce}(z)]\right\} * x_k \qquad (2.71)$$

where $\mathcal{Z}^{-1}\{\}$ denotes the inverse z-transform.

2.3.2.1 Conventional Filtered-X LMS Configuration

The quadratic cost function in $W(z)$ is created by squaring the random variable e_k and taking the expected value

$$\mathbf{C} = \mathbf{E}[(e_k)^2] \qquad (2.72)$$

Compute the gradient of the cost function by differentiating with respect to the adaptive weight, w_i

$$\frac{\partial C}{\partial w_i} = 2\mathbf{E}[e_k \frac{\partial e_k}{\partial w_i}] \tag{2.73}$$

$$= 2\mathbf{E}[e_k \mathcal{Z}^{-1} \left\{ \frac{\hat{T}_{ce}(z)z^{-i}}{1 - Q(z)} \right\} * x_k] \tag{2.74}$$

$$\approx 2e_k^e \hat{x}_{k-i} \tag{2.75}$$

where

$$\hat{x}_{k-i} = \mathcal{Z}^{-1}\{\frac{\hat{T}_{ce}(z)}{1 - Q(z)}z^{-i}\} * x_k \tag{2.76}$$

is the filtered-X signal required to update the filter coefficients of $W(z)$ with the following Widrow-Hoff LMS update equation

$$w_i(k+1) = w_i(k) - 2\mu e_k \hat{x}_{k-i} \tag{2.77}$$

$$\tag{2.78}$$

By examining equation (2.63), the optimal compensator that will make the error signal zero is

$$W(z)^* = -\frac{C(z)(1 - Q(z))}{A(z)} \tag{2.79}$$

and considering equation (2.69), if perfect cancellation of poles and zeros is assumed, the numerator will adapt to

$$W(z)^* = k_a C(z) \tag{2.80}$$

where $k_a = \frac{-1}{a_0}$ is a constant. Therefore, the zeros of the compensator adapt to the zeros of the disturbance loop, $T_{ne}(z)$, differing only by a constant. Now, the only

requirements to reduce the error signal to zero is for $(1 - Q(z))$ to be stable and that the adaptive numerator of the compensator, $W(z)$, be of the same or greater order than $C(z)$.

2.3.2.2 Equation Error Configuration

Using the equation error minimization technique described in section 2.2, the filtered-x filter can again be reduced to an FIR as shown in Figure 2.8. The error signal can be filtered with both the compensator and plant poles to produce

$$E^e(z) \ = \ [1 - B(z)][1 - Q(z)]E(z) \tag{2.81}$$

Now substituting equations (2.48), (2.54), and (2.63) into equation (2.81) and simplifying

$$E^e(z) \ = \ [C(z)(1 - Q(z)) + A(z)W(z)]X(z) \tag{2.82}$$

which can be written as

$$e_k^e \ = \ [c_k - c_k * q_k + s_k * w_k] * x_k \tag{2.83}$$

when the inverse z - transform is taken, where q_k is the unit sample response of the poles of the compensator. Now, the cost function becomes

$$\mathbf{C} \ = \ \mathbf{E}[(e_k^e)^2] \tag{2.84}$$
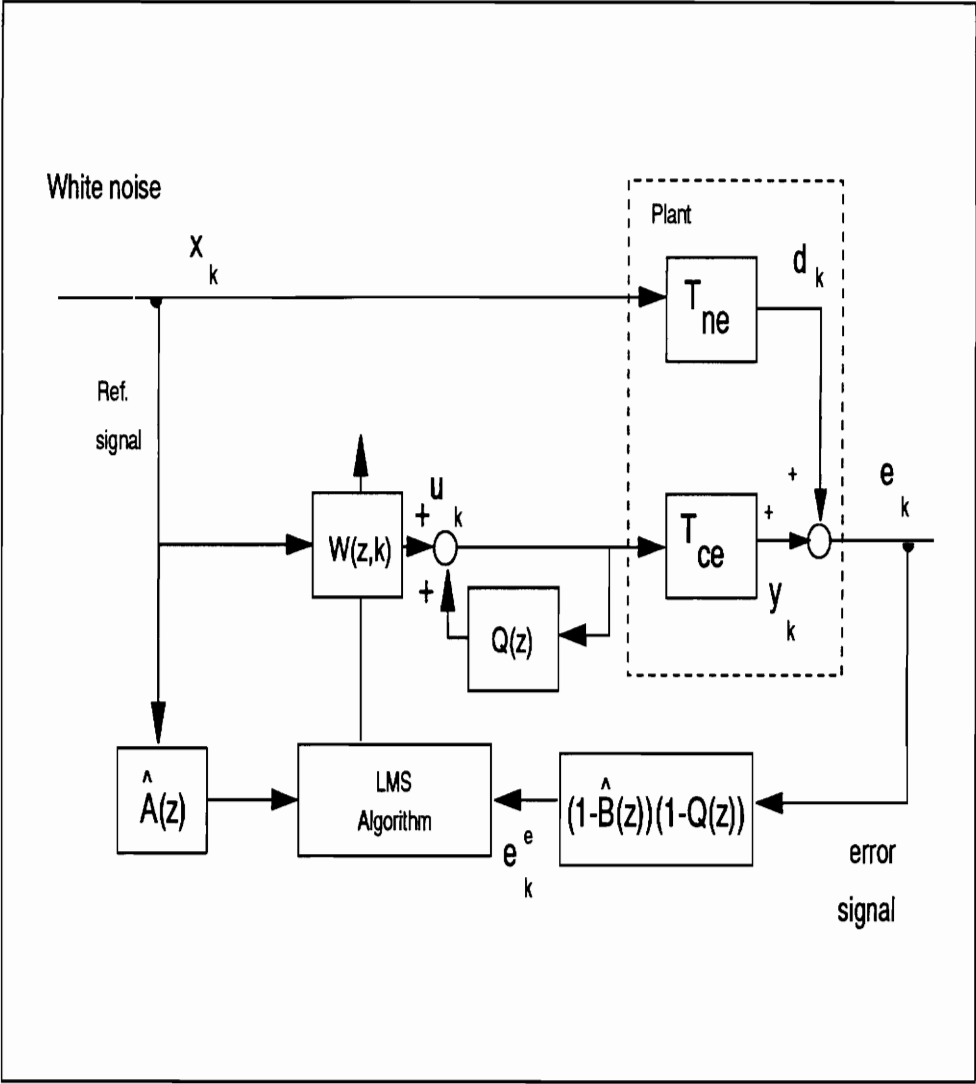
Figure 2.8: Equation error configuration of control system with a recursive compensator.

Computing the gradient of the cost function by differentiating with respect to the adaptive weight, w_i

$$\frac{\partial \mathbf{C}}{\partial w_i} = 2\mathbf{E}[e_k^e \frac{\partial e_k^e}{\partial w_i}] \tag{2.85}$$

$$= 2\mathbf{E}[e_k^e \hat{a}_k * x_{k-i}] \tag{2.86}$$

$$\approx 2e_k^e \tilde{x}_{k-i} \tag{2.87}$$

where

$$\tilde{x}_{k-i} = \hat{a}_k * x_{k-i} \tag{2.88}$$

is the filtered-X signal used in the instantaneous gradient approximation for the Widrow-Hoff algorithm:

$$w_i(k+1) = w_i(k) - 2\mu e_k^e \tilde{x}_{k-i} \tag{2.89}$$

$$\tag{2.90}$$

In the event that $\hat{T}_{ce}(z)$ is a nonminimum-phase transfer function, some of the poles of the compensator, $(1 - Q(z))$ as formed by equation (2.67) will lie outside the unit circle, making the compensator output unbounded. Therefore, the polynomial $(1 - Q(z))$ must be factored to discover the unstable roots in order to stabilize them. A simulation of such a nonminimum-phase system was performed and the unstable poles were found. Using the reciprocation technique from section 2.2 to reflect the unstable poles inside the unit circle produced a stable controller, but it did not minimize the error signal. One can see from equations (2.79) and (2.80) that if any of the unstable poles were reciprocated, the adaptive numerator would then need to

converge to

$$W(z)^* = k_a \frac{C(z) \prod_{i=1}^{m}(z - \frac{1}{z_i})}{\prod_{i=1}^{m}(z - z_i)} \tag{2.91}$$

for m unstable roots, z_i. The discrepancy between being able to successfully stabilize the identified transfer function $\hat{T}_{ce}(z)$ and unsuccessfully stabilizing $(1 - Q(z))$ results from the roots of $(1 - Q(z))$ being much further outside the unit circle that the roots of $(1 - \hat{B}(z))$. Another attempt to solve the stability problem was to cancel only the stable zeros of $\hat{A}(z)$ with $(1 - Q(z))$, but this technique also failed to yield any control of the plant response in simulations. Using the conventional practice of representing $\hat{T}_{ce}$ as a rational transfer function in z (equation (2.47)) will always yield an unstable inverse for nonminimum-phase systems. Perhaps this problem could be solved by using another representation for the plant inverse such as an artificial neural network (ANN) or other feedforward structure that is inherently stable.

2.3.3   Remarks on Broadband Versus Harmonic Control

Most of the research in adaptive, feedforward control has been for harmonic disturbances, due in part to the large number of applications and partly because of the simplicity. If a structure is undergoing a harmonic excitation, the response is also harmonic in the same frequency, but typically with a change in phase and magnitude. This transfer function is represented by the vertical line on the sample frequency response function (FRF) shown in Figure 2.9. The measured structural transfer function, $\hat{T}_{ce}(z)$, for a harmonic excitation can be represented with a two-weight
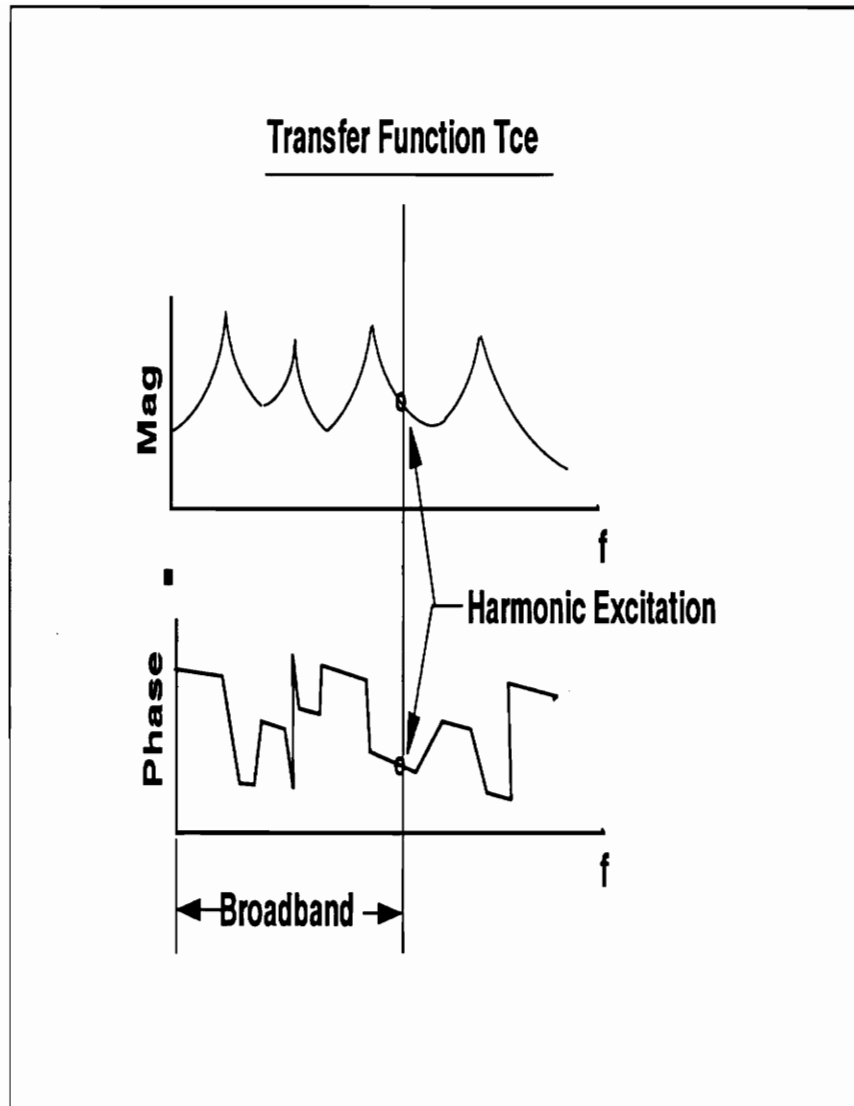
Figure 2.9: Example frequency response plot of the control–error path transfer function showing the difference between harmonic and broadband control on a structure.

FIR filter capable of changing the two degrees-of-freedom, phase and magnitude. When broadband vibration is controlled, the magnitude and phase information for the plant control loop, $\hat{T}_{ce}(z)$, is needed across a wide bandwidth of frequencies. Again, this point is illustrated in Figure 2.9.

Another point of interest that can be inferred from section 2.3.2 is that since the optimal control compensator is an ARMA structure, the control compensator will need to be either an IIR of low but sufficient order or a very high order FIR filter. In contrast, a single harmonic tone can again be cancelled by a two-weight FIR filter which is capable of changing phase and magnitude of the deterministic reference signal until it cancels the response due to the disturbance at the error sensor location.

2.4   Simulation of Control Algorithms

Each of the four control algorithms presented earlier in this chapter were simulated on a computer using the Matlab software by MathWorks [37]. A simply-supported steel beam with dimensions 380 x 40 x 0.2 mm was chosen for the plant. The mass was chosen to be 0.232 kg and the damping ratio was assumed to be 1% for each mode. The beam and actuator properties are equivalent to the real beam to be used in the experimental analysis described in chapter 4. Figure 4.2 in on page 63 illustrates the locations of the accelerometer and the piezoelectric patches used as the sensor and actuators, respectively. An equivalent loading diagram is also shown at the bottom of that figure. The error sensor was assumed to be located 238mm

from the left edge of the beam. A pair of line moments, 150 and 188mm from the left edge of the beam, were applied by the disturbance actuator. Chapter 4 describes the action of piezo actuators in more detail. The control moments were applied 265 and 303mm from the left edge. A Gaussian white noise sequence was used for the input signal. Table 2.1 lists the analytical natural frequencies of the beam, the first three of which were included in the model. Appendix A provides details on how the discrete model of the beam was obtained for the simulations.

Table 2.1: Analytical Natural Frequencies

Mode	Analytical f_n (Hz)
1	31.73
2	127.0
3	285.6
4	507.8
5	793.5
6	1142.6
7	1555
8	2031

The simulation results will be presented in the same order that the algorithms were developed. The simulation results from the Conventional Filtered-X FIR control are shown in Figure 2.10. This particular simulation used an adaptive filter with 20 coefficients, a convergence parameter of $\mu = 1e^{-5}$, and a sample rate of 2000 Hz. Although the error signal was not completely minimized, a reduction of 13 dB in the error signal power was observed. Similar results were observed for the Equation Error FIR Control, using 20 adaptive coefficients, a sampling frequency of 2 kHz, and a convergence parameter of $3e^{-3}$. The uncontrolled and controlled
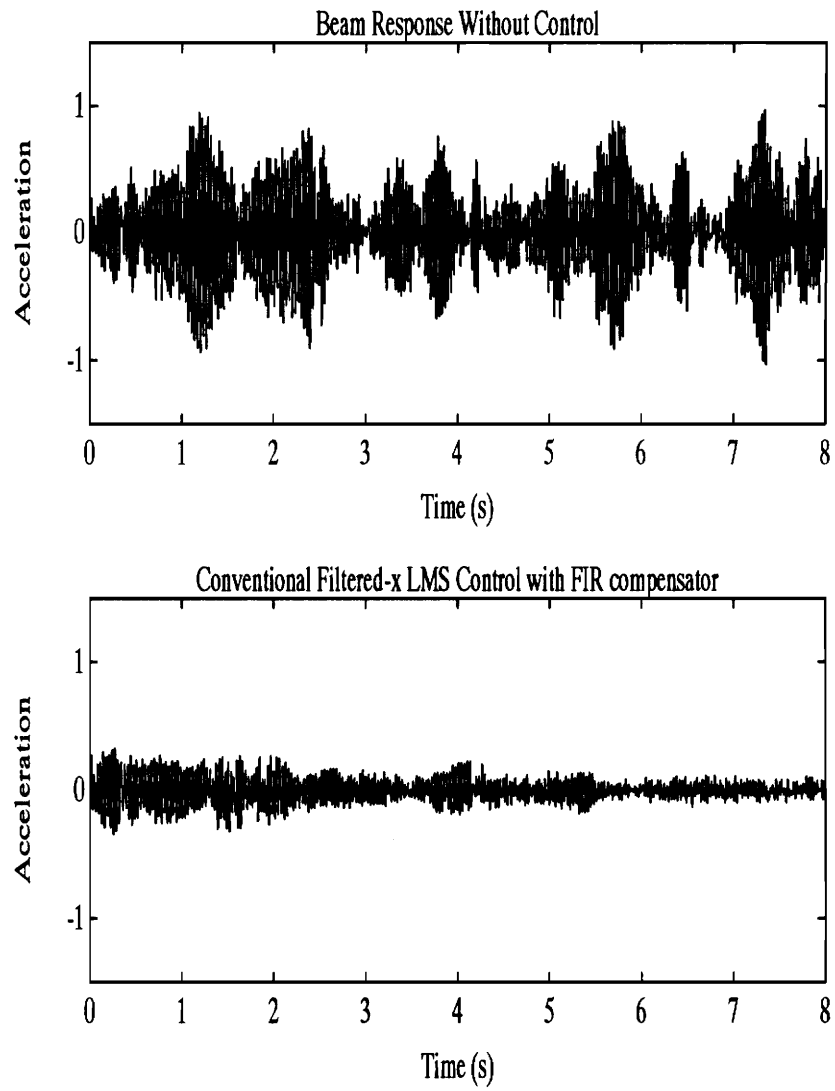
Figure 2.10: Simulation of Conventional Filtered-X FIR Control algorithm when applied to the discrete-time model of a simply-supported beam.

time histories are compared in Figure 2.11, where the power of the controlled error signal is 8 dB less than the uncontrolled plant response. Although the largest signal oscillations are attenuated, control is generally not as good as that observed for the Conventional FIR Controller.

For the simulations of the Filtered-X algorithms incorporating a recursive compensator, the error sensor location was moved to correspond with the center of the control actuator, 285mm from the left edge. The colocation of the error sensor and control actuator provided a minimum-phase transfer function for the control loop. Simulation results from the Conventional Filtered-X IIR Controller can be found in Figure 2.12. Here, the adaptive compensator has only 6 coefficients, one order higher than the order of numerator of $T_{ne}(z)$. As anticipated, the error signal almost completely diminished, with an attenuation of 23 dB. Simulation results from the Equation Error recursive algorithm show a 27 dB reduction in the error signal as shown in Figure 2.13. Again, the error signal was almost driven to zero. The same sampling rate and adaptive filter order as above were used, along with a convergence parameter of $5e^{-5}$.

Two additional simulations were performed using the recursive controller. Firstly, the moduli of all the compensator poles were perturbed by 10% to determine how the errors in estimating $\hat{T}_{ce}(z)$ would affect control performance. The error signal was still minimized almost completely, although convergence was slower. Secondly, the same analysis was repeated with 20% error in the poles. Complete attenuation was no longer possible, but a very significant reduction was observed. The robust behavior of the LMS algorithm allowed the unconventional practice of

45
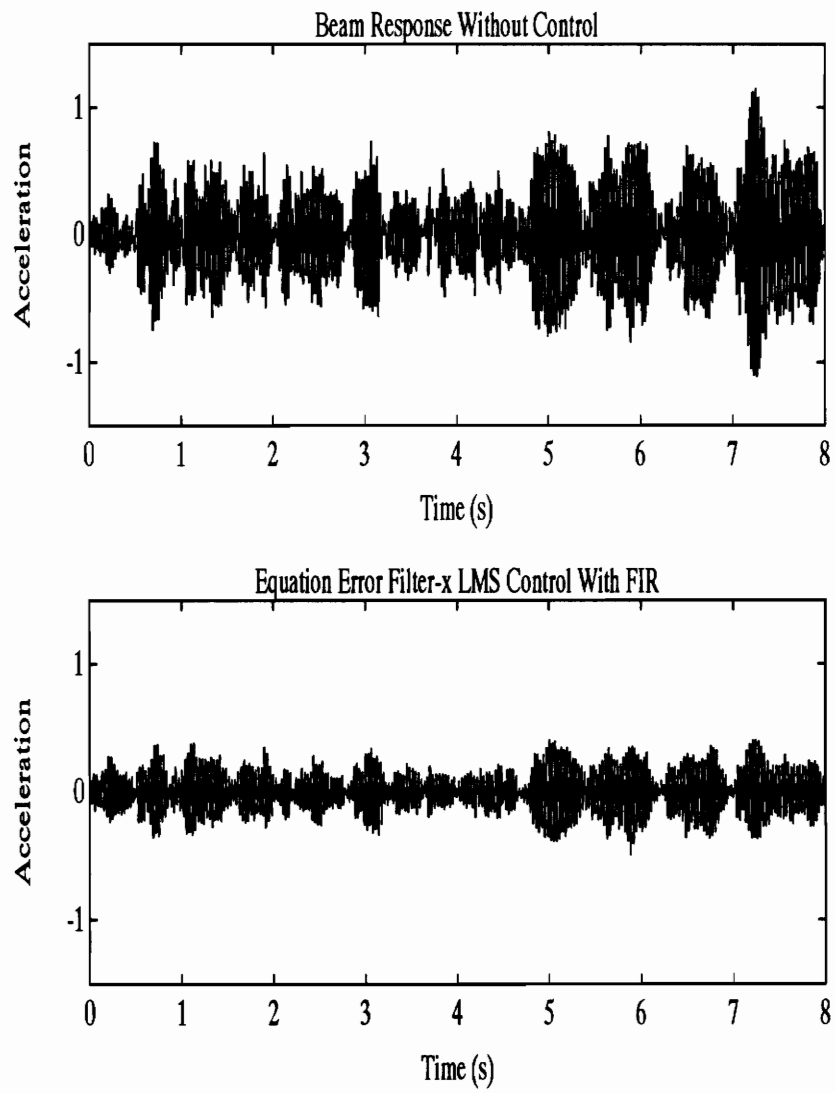
Figure 2.11: Simulation of Equation Error Filtered-X LMS FIR control algorithm when applied to a simply-supported beam.

46
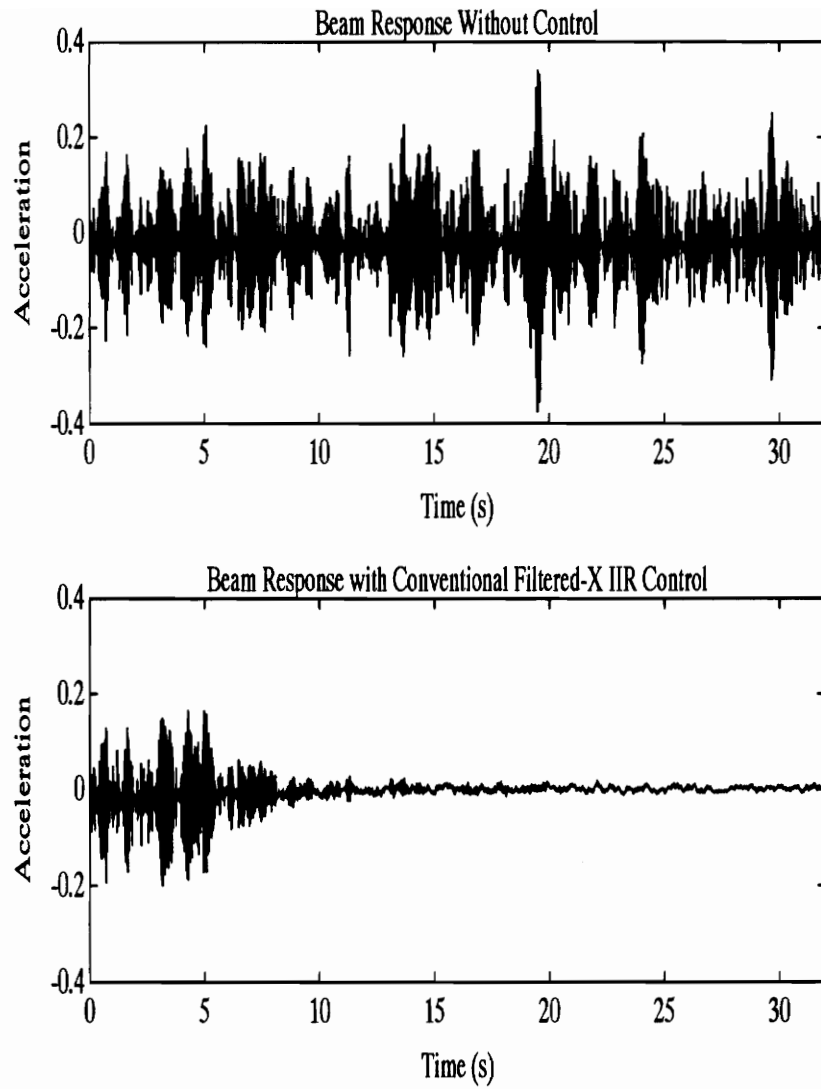
Figure 2.12: Simulation of the Conventional Filtered-X LMS algorithm using a recursive compensator on a minimum-phase plant.

47

pole-zero cancellation to be feasible.
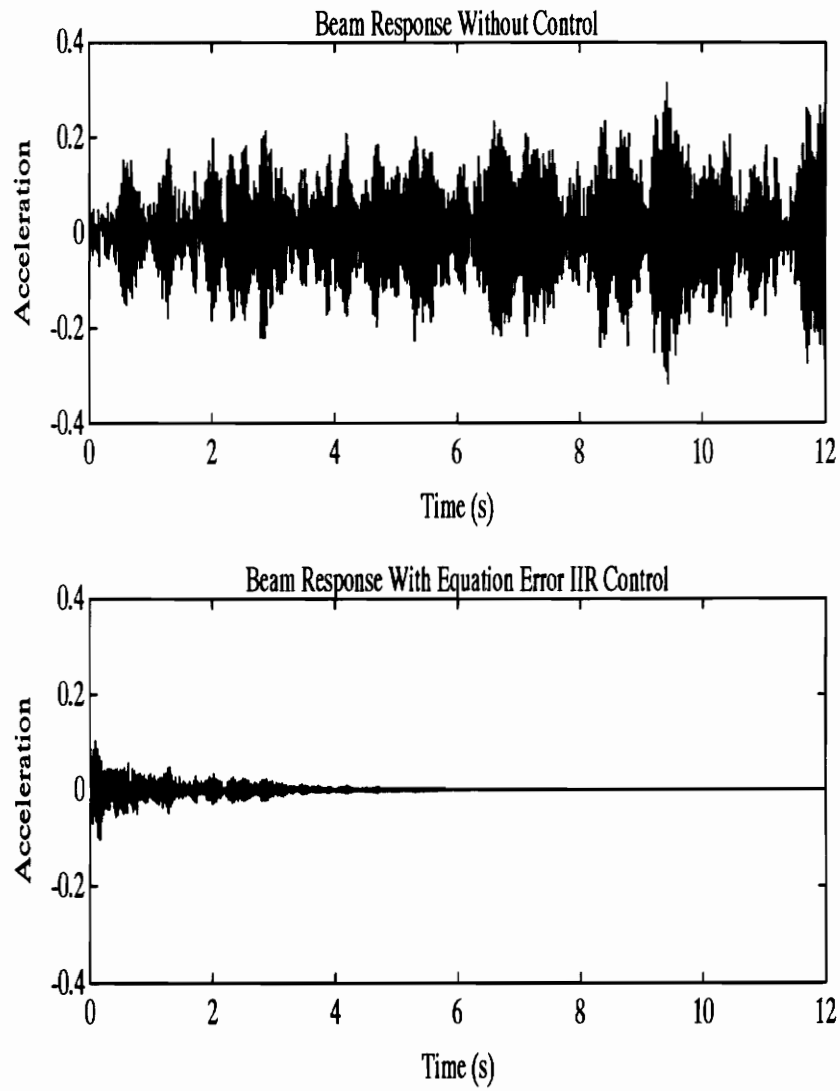
Figure 2.13: Simulation of the Equation Error Filtered-X LMS algorithm using a recursive compensator on a minimum-phase plant.

Chapter 3

System Identification of Control-loop Transfer Function

It was shown in section 2.3 that a system identification of the control loop must be performed before filtered-X LMS adaptive control can be implemented. The system identification can be implemented either on-line simultaneously with control or off-line, as was done for this research. Once the transfer function is known, it can be used to predict the response of the control loop when excited by the reference signal. This 'filtered-X signal' is then correlated with the measured error signal so that the appropriate gradient can be estimated for the LMS coefficient update (e. g. equations (2.46) and (2.62). Section 2.3.3 discussed the differences in the system identification when broadband disturbances are present as opposed to harmonic excitations of a system.

A linear dynamic system can be identified by examining the properties of both a spectrally-rich input noise and the corresponding plant response. Figure 3.1 shows an unknown system and the response, y_k, and the white noise input, x_k. An

alternative system identification is shown in Figure 3.2 where the parameters of a system model are adapted to minimize the output error. The plant is identified when the error signal is driven to zero. With either method of system identification, a proper-order system model must first be realized before the model parameters are estimated. The conclusion of section 2.3.3 was that an autoregressive moving-average (ARMA) model will most efficiently model a lightly damped structural plant. ARMA models, which are synonymous with IIR filters, can be approximated with a high-order MA model [18] and have the advantage that they are always stable. Before an ARMA filter was used for the system identification an FIR (MA model) filter with 40 coefficients was first used to model the dynamics of the beam. The FIR filter produced unsatisfactory results and a filter of any larger order was deemed undesirable.

3.1 Least-Square Solution of ARMA Model

Recursive filters representing plants with both poles and zeros as shown in equation (2.47) are often referred to a autoregressive-moving average (ARMA) models. A time series ARMA model of order N can be written as

$$y_k \;=\; \sum_{i=0}^{N} a_i x_{k-i} + \sum_{j=1}^{N} b_j y_{k-j} \tag{3.1}$$

where y_k is the filter output, x_k is the input sequence, a_i and b_i are respectively the coefficients of the MA and AR portions of the IIR filter.

Multiplying each side of equation (3.1) consecutively by each element from
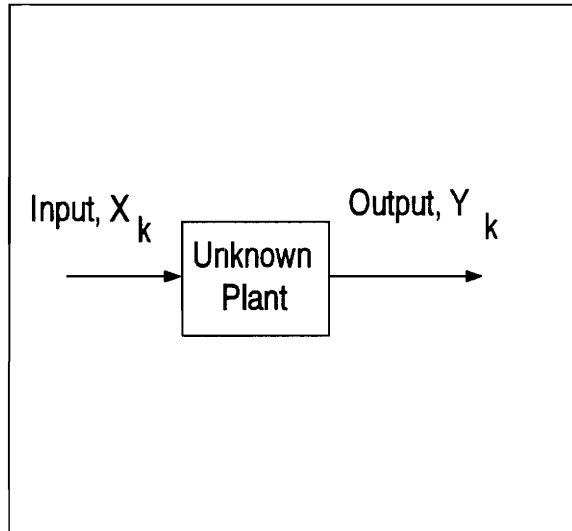
Figure 3.1: System identification of the impulse response of an unknown system through time domain analysis.
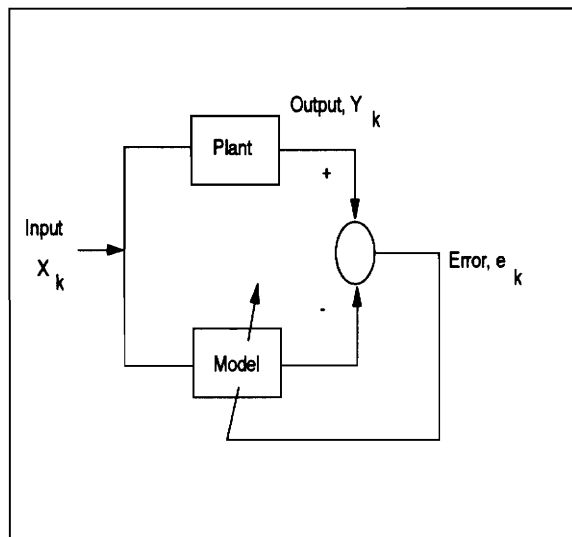
Figure 3.2: System identification of a plant via an adaptive model.

the sequences $\{x_k\}$ and $\{y_k\}$ (e.g. $\{x_k, x_{k-1}, \ldots, x_{k-N}, y_{k-1}, \ldots, y_{k-N}\}$) and taking the expected value, the following linear system of equations results

$$\left\{ \begin{array}{c} \{R_{xy}\} \\ \{R_{yy}\} \end{array} \right\} = \left[\begin{array}{cc} [R_{xx}] & [R_{xy}] \\ [R_{yx}] & [R_{yy}] \end{array} \right] \left\{ \begin{array}{c} [\{A\}] \\ [\{B\}] \end{array} \right\} \tag{3.2}$$

The components in this equation are defined in terms of the auto and cross correlation functions of the sequences $\{x_k\}$ and $\{y_k\}$ as

$$\{R_{xy}\} = \left\{ \begin{array}{c} R_{xy}(0) \\ R_{xy}(1) \\ \vdots \\ R_{xy}(N) \end{array} \right\} \tag{3.3}$$

$$\{R_{yy}\} = \left\{ \begin{array}{c} R_{yy}(1) \\ R_{yy}(2) \\ \vdots \\ R_{yy}(N) \end{array} \right\} \tag{3.4}$$

$$[R_{xx}] = \left[\begin{array}{cccc} R_{xx}(0) & R_{xx}(-1) & \cdots & R_{xx}(-N) \\ R_{xx}(1) & R_{xx}(0) & \cdots & R_{xx}(-N+1) \\ \vdots & \vdots & \ddots & \vdots \\ R_{xx}(N) & R_{xx}(N-1) & \cdots & R_{xx}(0) \end{array} \right] \tag{3.5}$$

$$[R_{xy}] = \left[\begin{array}{cccc} R_{xy}(-1) & R_{xy}(-2) & \cdots & R_{xy}(-N) \\ R_{xy}(0) & R_{xy}(-1) & \cdots & R_{xy}(-N+1) \\ \vdots & \vdots & \ddots & \vdots \\ R_{xy}(N-1) & R_{xy}(N-1) & \cdots & R_{xy}(1) \end{array} \right] \tag{3.6}$$

$$[R_{yx}] = \left[\begin{array}{cccc} R_{yx}(1) & R_{yx}(0) & \cdots & R_{yx}(1-N) \\ R_{yx}(2) & R_{yx}(1) & \cdots & R_{yx}(2-N) \\ \vdots & \vdots & \ddots & \vdots \\ R_{yx}(N) & R_{yx}(N-1) & \cdots & R_{yx}(0) \end{array} \right] \tag{3.7}$$

53

$$[R_{yy}] = \begin{bmatrix} R_{yy}(0) & R_{yy}(-1) & \cdots & R_{yy}(-N+1) \\ R_{yy}(1) & R_{yy}(0) & \cdots & R_{yy}(-N+1) \\ \vdots & & \ddots & \vdots \\ R_{yy}(N-1) & R_{yy}(N-1) & \cdots & R_{yy}(0) \end{bmatrix} \quad (3.8)$$

where the correlation functions and some of their properties are defined as

$$\begin{array}{rcl} R_{xx}(m) & = & E[x_k x_{k+m}] = R_{xx}(-m) \\ R_{xy}(m) & = & E[x_k y_{k+m}] = R_{yx}(-m) \end{array} \quad (3.9)$$

The unknown filter coefficients a_i and b_i are the components of the vectors

$$\{A\} = \left\{ \begin{array}{c} A_0 \\ A_1 \\ \vdots \\ A_N \end{array} \right\} \quad (3.10)$$

$$\{B\} = \left\{ \begin{array}{c} B_1 \\ B_2 \\ \vdots \\ B_N \end{array} \right\} \quad (3.11)$$

Solving the system in equation (3.2) will produce a least square (LS) solution for the IIR filter coefficients, which represent a complex polynomial in z. This type of solution provides the advantage that the poles do not have to be broken into second order sections and checked for stability during the identification process (as described in Section 2.2). Rather, the poles can be factored and stabilized after the parameter estimation is complete and before the filter is implemented in the control system.

The denominator polynomial of the transfer function in equation (2.47) can

be factored into the form

$$1 - B(z) \; = \; 1 - b_1 z^{-1} - b_2 z^{-2} \ldots - b_N z^{-N} \qquad (3.12)$$

$$= \; z^{-N}(z - z_1)(z - z_2)(z - z_3) \cdots (z - z_N) \qquad (3.13)$$

where $z_i, (i = 1, 2, \ldots, N)$, are the roots or poles of the structure. They occur in complex conjugate pairs, representing the individual second order sections of the structure. A pole, and therefore the filter, is stable when its modulus is less than one. Poles can be made stable by reciprocation, a process where each unstable root is reflected it back inside the unit circle [17]. This procedure approximately preserves the magnitude response of the transfer function, but alters the phase response. An accurate estimate of the phase could be needed for response prediction of the control loop when excited by the disturbance input (generation of the filtered-x reference signal). If necessary, the phase corruption can be remedied by using the adaptive IIR configuration for system identification as explained in section 3.2.

3.2 Adaptive IIR Filters Applied to System Identification

The adaptive IIR configuration discussed in section 2.2 can be used to correct the phase corruption which may occur during stabilization of the least-squares ARMA solution described in section 3.1. In this case, the coefficients of the stabilized ARMA model provide the first guess to the LMS solution where only the numerator coefficients of the IIR filter, a_i, are adapted using equation (2.33). A schematic of this process is shown in Figure 3.3. A simulation of RLMS phase-correction process

was carried out and the results are shown in Figure 3.4. As can be seen by the bottom plot, the error signal diminishes as the numerator coefficients are adapted. Correcting the ARMA model will be more difficult in a real implementation, since the RLMS is more sensitive to noise. The RLMS can also introduce bias error into the estimate of $\hat{T}_{ce}(z)$, potentially worsening the model. It is not known how the accuracy of $\hat{T}_{ce}(z)$ affects the convergence and stability of the algorithms.
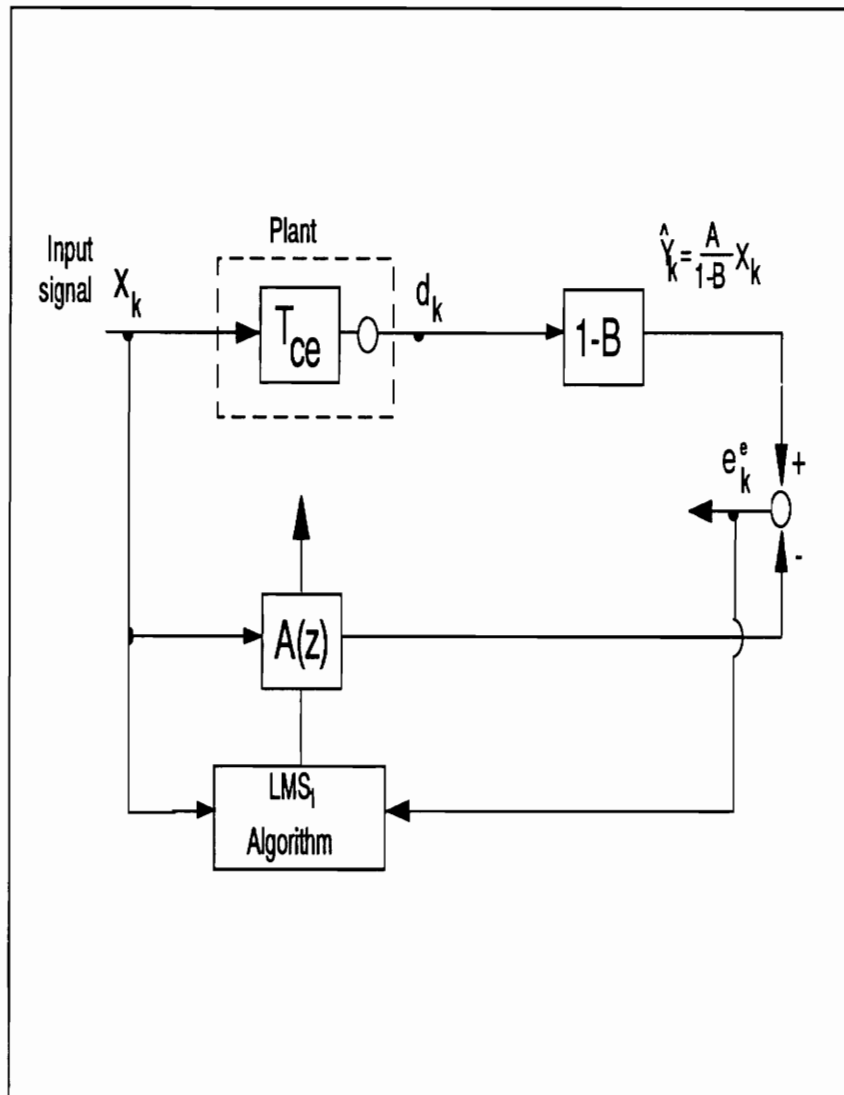
Figure 3.3: Adaptive IIR filter used to correct phase corruption of stabilized ARMA model.
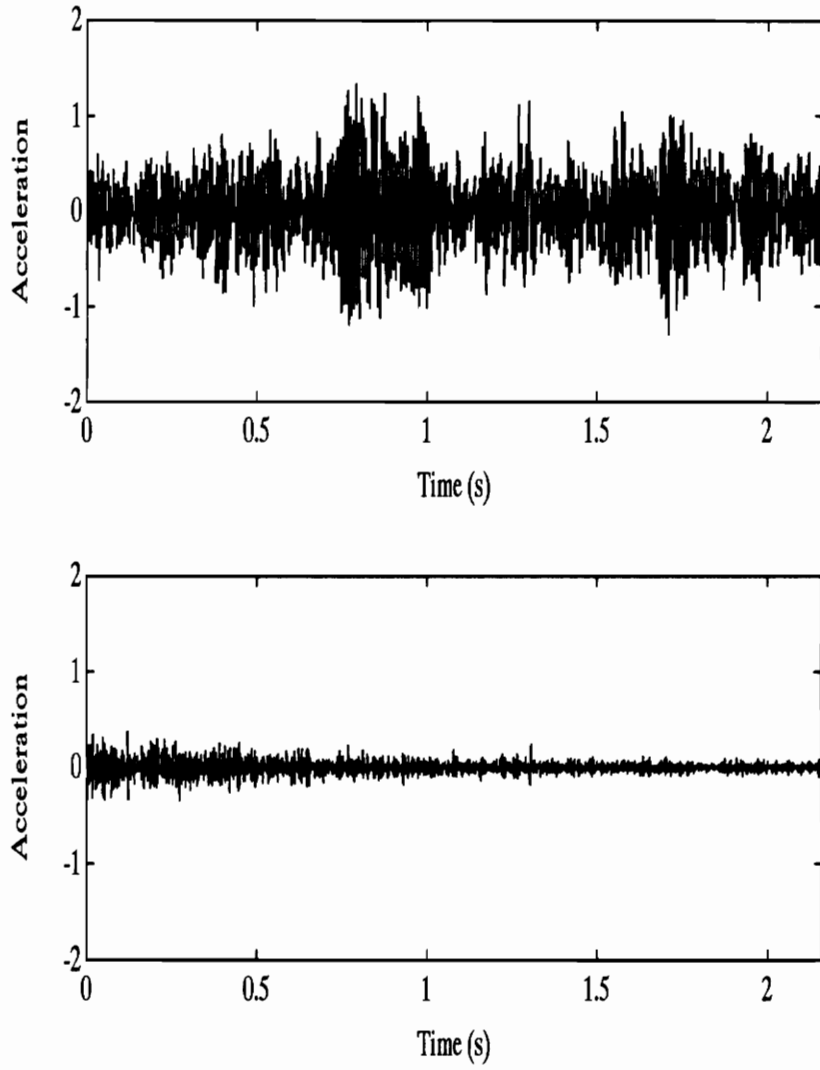
Figure 3.4: Convergence process when the adaptive phase-correction scheme shown in the previous figure was employed: (top) plant response, (bottom) difference between actual and estimated plant response (e_k).

58

Chapter 4

Experimental Setup and Procedure

Theoretical analyses and simulations are important tools for the understanding and development of controls and other processes. However they are limited since real–world applications are plagued by noise, measurement errors, nonstationarities and the like. Therefore, experimental demonstration of the control algorithms is essential to show that they will be useful for real applications. The performance of the control algorithms are demonstrated with active vibration control on a simply-supported beam. However, these algorithms should be able to control acoustic radiation as well as vibration, with the only difference being the effects of the structural–acoustic coupling.

4.1 Test Rig

A small, simply–supported beam was used in all of the broadband vibration control experiments. The beam is made of plain carbon steel and has dimensions

380 x 40 x 2 mm. Two thin, flexible metal shims connect the beam to a heavy support stand, providing the desired simply-supported end conditions. A picture of the test rig is shown in Figure 4.1. Table 4.1 lists the first six natural frequencies which were obtained experimentally. They agree within 6% with the analytical natural frequencies listed in Table 2.1. The experiment was limited to control of the first three bending modes because the location of the control actuator pair rendered the fourth mode uncontrollable. Two separate actuator and sensor configurations were used depending on whether the control system employed and FIR or IIR compensator since the IIR system requires a minimum-phase control-loop. Both are illustrated in Figures 4.2 and 4.3 along with their effective loading diagrams.

Table 4.1: Experimental Natural Frequencies

Mode	Experimental f_n (Hz)
1	32.9
2	126.9
3	282.3
4	498.6
5	768.7
6	1077.0

4.1.1 Configuration 1: Setup for Systems Using an FIR Compensator

The error sensor was a Brüel & Kjær mini-accelerometer located 238 mm from the left edge of the beam, a location capable of sensing the modes of interest. Control action was applied by a co-located set of Piezo Products' G1195 piezoelectric strips.
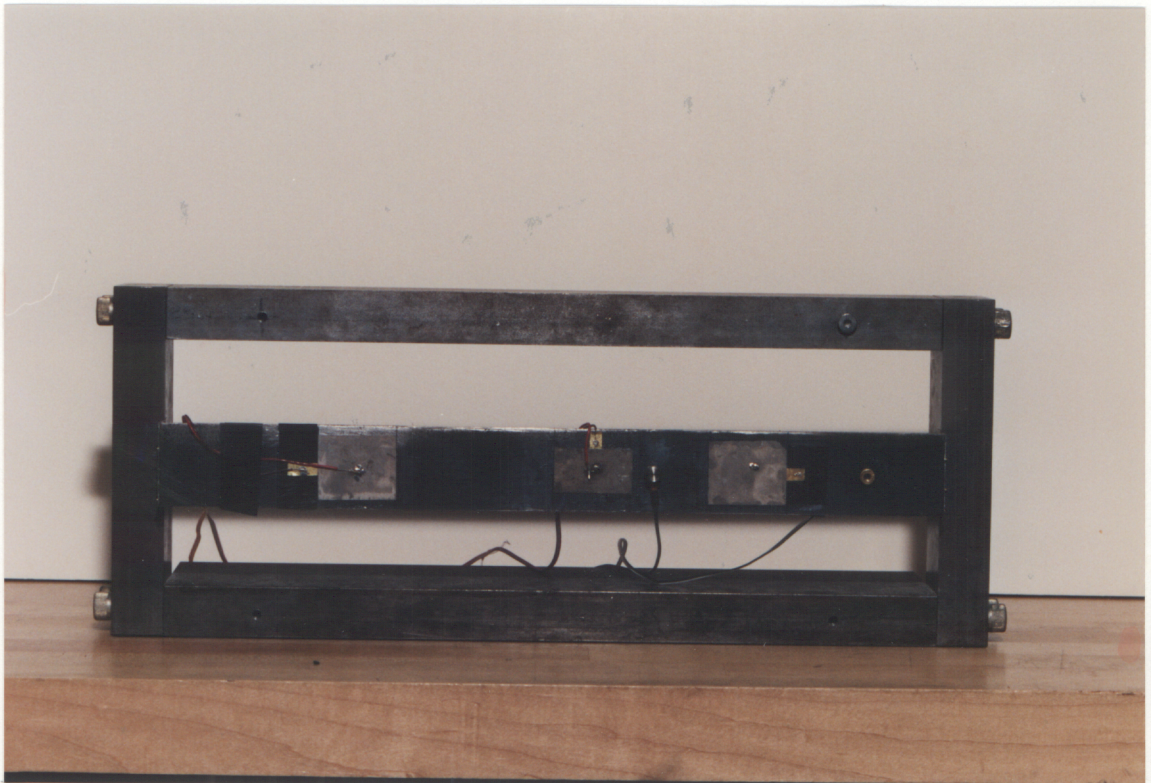
60

Figure 4.1: Picture of test rig showing beam and piezo-electric patches. The square piezo patch on the far right is the control actuator, the center, rectangular patch is the disturbance actuator, and the far left patch was not used in these experiments. The accelerometer can be seen between the disturbance and control patches.

The piezoelectric strips measured 38.1 x 32.0 x 0.2 mm and their closest edge was located 265 mm from the left edge of the beam. Figure 4.2 shows the layout of the actuators and sensor, along with the equivalent schematic diagram of the loading. Piezo patches apply an in-plane strain at the patch/beam interface. Since the two control-actuator patches have the same geometry and are connected out of phase, equal and opposite strains are applied to each side of the beam. The net effect of the actuator (pair of patches) is to apply two line moments, M_c, at each edge of the piezo patches, which excite the beam in pure bending [38, 39]. The disturbance or input actuator was applied by a single piezoelectric strip. It measured 38 x 22 x 0.2mm and was affixed 150mm from the left edge of the beam, where it is capable of exciting the first three modes. A single patch results in both bending and extensional excitations (M_d and F_d in Figures 4.2 and 4.3).

4.1.2 Configuration 2: Setup for Systems Using an IIR Compensator

A minimum-phase plant can be achieved by co-locating the control actuator with the error sensor. Hence a point-force input was achieved with an electrodynamic shaker which was mounted opposite the accelerometer at the same axial location on the beam, 327 mm from the left edge. Again, this arbitrary location renders the first three bending modes observable and controllable. The disturbance input was achieved with the same piezo strip described in Configuration 1. Figure 4.3 illustrates the locations of the sensors and actuators for the second configuration described above.
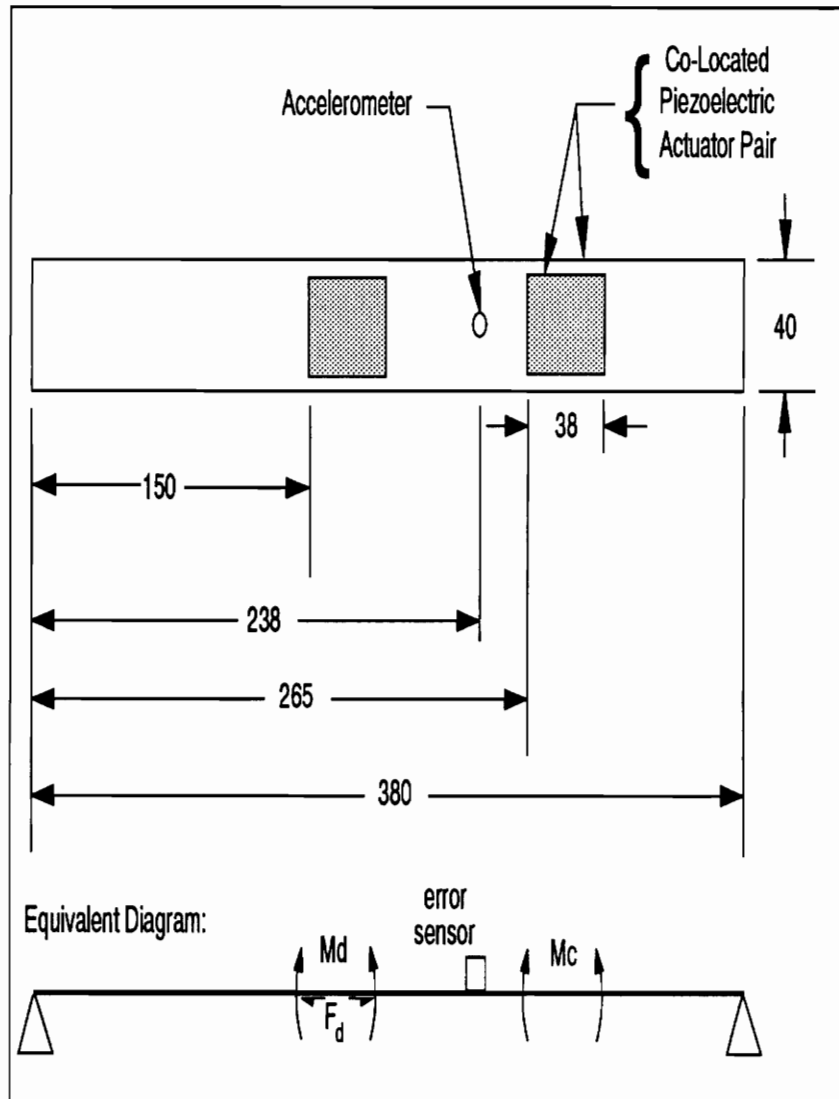
62

Figure 4.2: Sensor and Actuator locations on the simply–supported beam used for the experimental analysis of the control systems incorporating and FIR compensator. All dimensions are in mm.
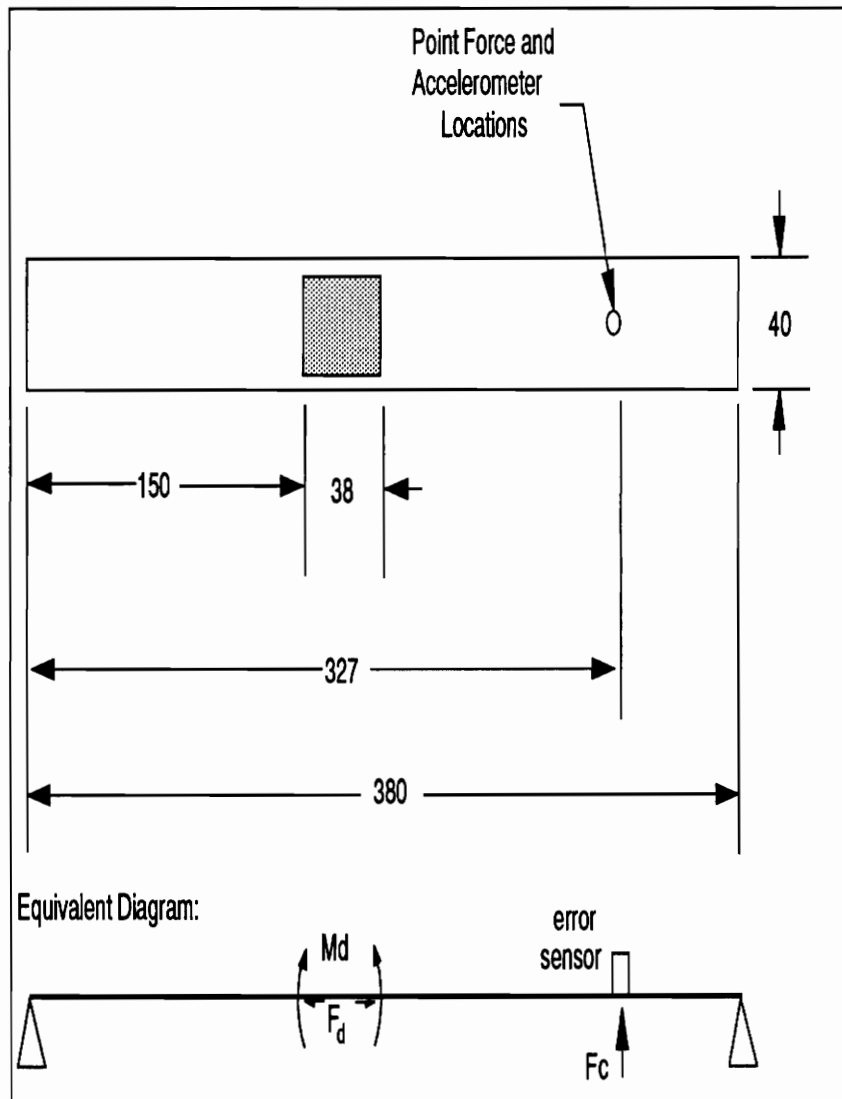
Figure 4.3: Sensor and Actuator locations on the simply–supported beam used for the experimental analysis of the IIR control systems. All dimensions are in mm.

4.2 Instrumentation

The control approaches presented in chapter 2 were implemented in a Texas Instruments TMS320C30 (C30) digital signal processor (DSP) board which was resident in a host 80386–based personal computer (PC). All of the DSP programs were written in Assembly language and compiled into stand-alone executables for the C30. Additional programs were written for the PC in 'C'-language to direct different tasks such as: 1) downloading C30 executables, 2) starting/stopping execution of the C30, and 3) passing parameters between the PC and C30 (e.g. convergence parameter, sampling rate, system identification parameters, etc.).

Although this is a SISO control system, a second input to the DSP was required for the reference signal. Figure 4.4 shows the complete experimental setup including the details about the two inputs (reference, error) and one output (control) of the DSP. A second DSP board (TMS320C20) was used to provide a pure delay in the disturbance signal for Configuration 1 to achieve a causal control system. The accelerometer signal was conditioned with a Brüel & Kjær type 2635 charge amplifier which also performed an analog integration of it. It was observed that the controller produced better results when velocity rather than acceleration was used as the error signal. This result is believed to be due to the removal of the low-frequency noise occurring below the first mode, since the cut-off frequency of the high-pass filter in the accelerometer charge amp is 10 Hz for a velocity signal compared to 2 Hz for an acceleration signal. A Frequency Devices 9002 low-pass filter was used as an anti-aliasing filters for the error signal and two additional FD9002 low-pass

filters were used to smooth the control signal and delayed disturbance signal before driving the structure with them. All three of these filters were removed to analyze the recursive control systems because their large phase shift made the control loop have nonminimum phase. A fourth FD9002 low-pass filter was used to band-limit the input random noise signal generated by a Brüel & Kjær analyzer to 400 Hz. All time and frequency domain analysis was done by the Brüel & Kjær 2032 and was downloaded to a PC via an IEEE-488 interface. A programmable digital delay z^{-d} was implemented in the disturbance path using a TMS320C20 (C20) DSP board installed in a separate computer. By selecting the number of delay taps in conjunction with the sample rate of the C20, an appropriate delay can be added to the disturbance signal to make the control system causal, if needed. Figure 4.4 shows a schematic diagram of the complete experimental setup.

4.3   Experimental Procedure

Both control configurations were checked for causality before implementing the control systems. Propagation times from both the disturbance and control inputs to the error output were measured by computing the cross correlation functions across each path while they were excited by white noise. The propagation time for each path is found at the largest peak on the respective cross correlation functions and it is discovered that the disturbance path has a propagation time that is 3 ms longer than that of the control path in Configuration 1. A 3.9 ms delay was added to the disturbance signal by selecting a sample rate of 15 kHz and 59 delay taps for the C20 DSP. Delaying the disturbance signal with respect to the control input allowed
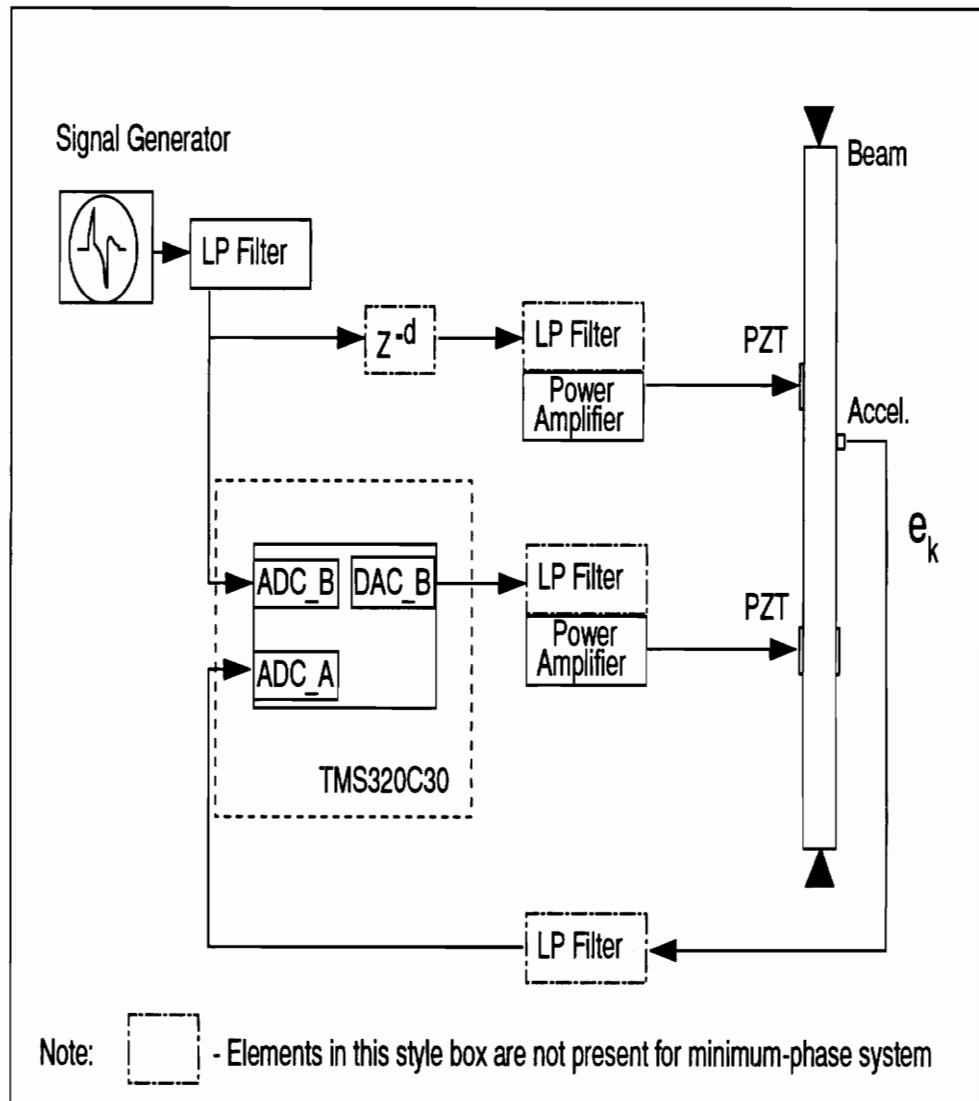
66

Figure 4.4: Block diagram showing the experimental setup.

the acausal optimal control solution for the system to be implemented. The second configuration was naturally causal because of the co-location of the control actuator and error sensor, in addition to the removal of the low-pass filters. Although the low-pass filters do not produce a pure time delay, they provide enough phase-shift in the higher-frequency content of the time-domain signal to make the optimal control filter acausal.

Before the control algorithms can be implemented, one must first perform the off-line system identification. A random signal is fed into the reference input channel of the DSP and echoed back out the control output channel. A DSP code measured the two signals and computed the statistics for the ARMA model shown in equation (3.2). Approximately 30,000 points were used to compute the correlation functions, which were sent back to the PC to form the linear system shown in equation (3.2) on page 53 and solve for the filter coefficients $\hat{a}_i$ and $\hat{b}_i$ of $\hat{T}_{ce}(z)$. The poles were then computed by solving for the zeros of $(1 - \hat{B}(z))$, and the unstable poles were stabilized by reciprocation, as described in Section 2.2. In the event that the stabilized model has accurately identified the system natural frequencies but does not provide adequate performance for the control system, the phase corruption occurring from the pole reciprocation can be remedied by using the adaptive IIR configuration shown in Figure 3.3 from section 3.2, to adapt only the numerator coefficients of the filter, $\hat{a}_i$. In this case, the coefficients of the stabilized ARMA model provided the first guess to the LMS solution. When evaluating the performance of the Conventional FIR control, the "phase-corrected" ARMA model did not appear to provide any better control than an uncorrected model. Therefore, the RLMS phase-correction process was not performed for any of the experiments

which will be presented in the next chapter. A comparison between the autospectra of the filtered-x signal and the real output error for Configuration 1 (FIR Control System) are presented in Figure 4.5, and they show very good agreement. The IIR filter coefficients were stored on the hard-disk to be loaded into the memory of the DSP and be used by the control codes at a later time. The off-line system identification process was *necessarily repeated* when Configuration 2 of the test rig was implemented since a different error/control actuator combination was used. Next, the random input signal was applied to the disturbance actuator and the performance of the different control configurations was investigated. The sampling rate used for the system identification and control experiments was 2000 Hz.
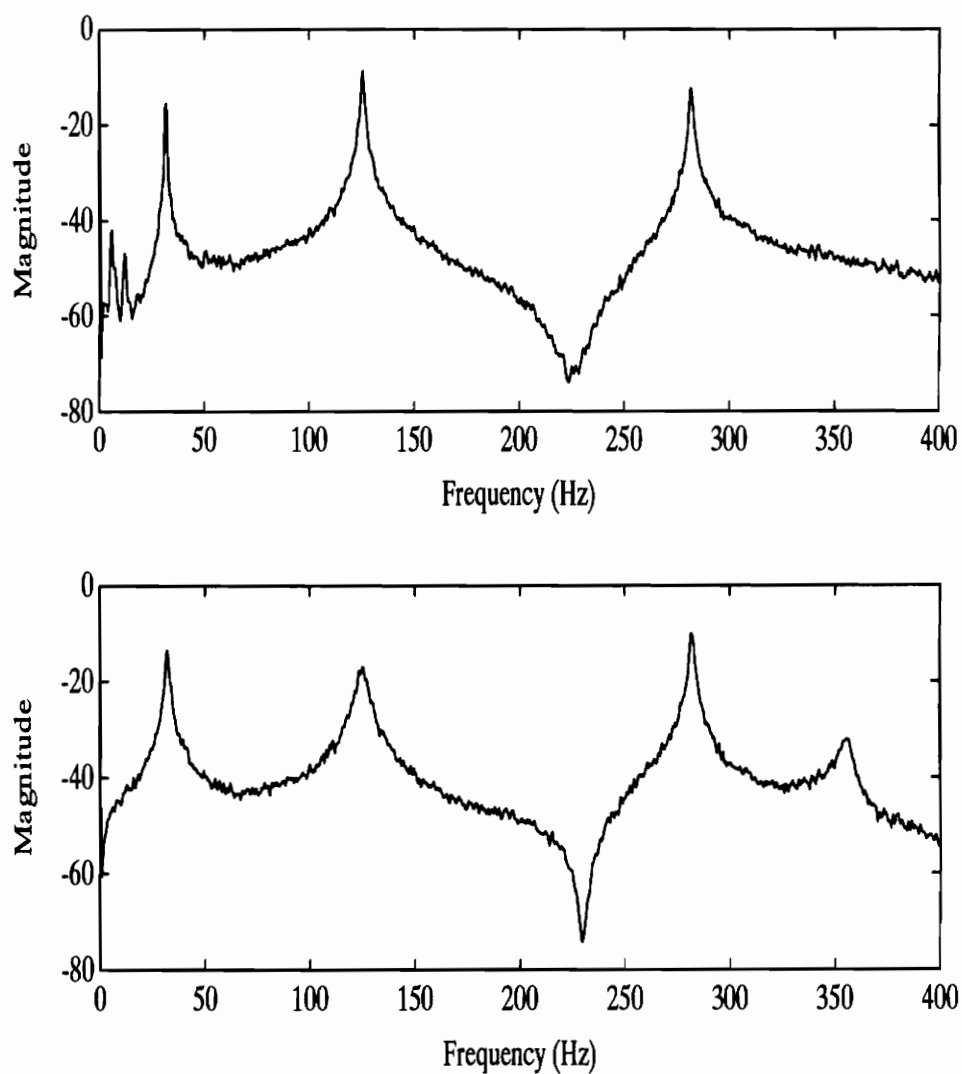
Figure 4.5: Comparison of autospectra between plant control-loop response (top) and the filtered-x signal (bottom) for a white noise input.

70

Chapter 5

Experimental Results

The experimental results are presented in the same order as the theoretical developments in chapter 2. Results will be displayed in both the time and frequency domains. All experiments are performed with a causal control system except for the indicated experiments with the Conventional FIR Controller, where an acausal system was experimentally examined.

5.1 Conventional Filtered-X LMS Control With FIR Compensator

Figure 5.1 shows a comparison of the steady-state error signal measured from the beam both before and after the Conventional Filtered-X LMS Control was applied with a 24th order adaptive FIR. Although the error signal was not reduced to zero, a large amount of vibration attenuation was achieved by the controller. A comparison of the graphs of the power spectral density of the two error signals is shown in Figure 5.2, and it gives additional insight into the control mechanism. Despite an

Figure 5.1: Measured error signal from the plant. (top) before control; (bottom) after convergence of Conventional Filtered-X LMS Control using an FIR.

Figure 5.2: Auto Spectrum of the error signal. —— before control; - - - after applying Conventional Filtered-X LMS Control using an FIR.

increase of the spectrum in some of the off–resonance frequency bands, the spectrum displays a reduction of approximately 20-25 dB at the system resonances. The net reduction in mean–square error over the bandwidth was 19.4 dB. Thus, the controller behaves as a wide-band controller r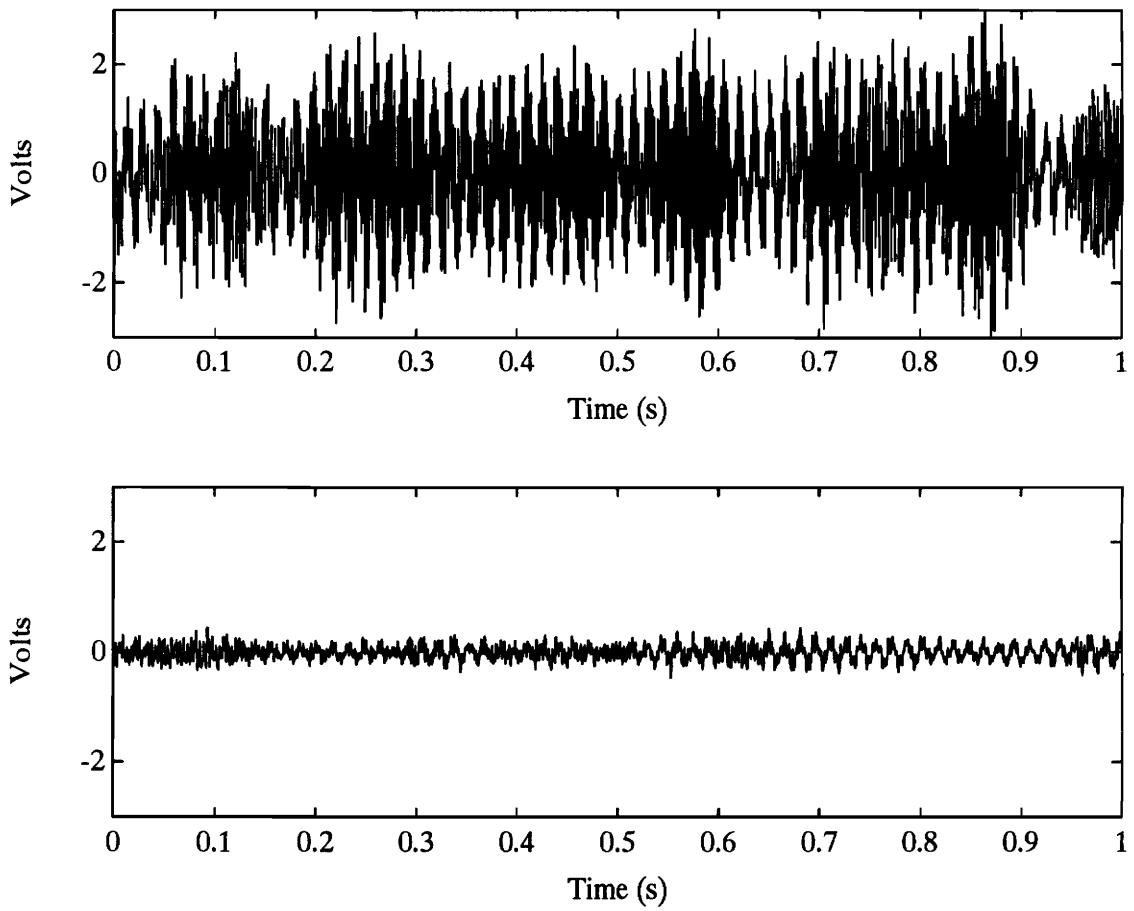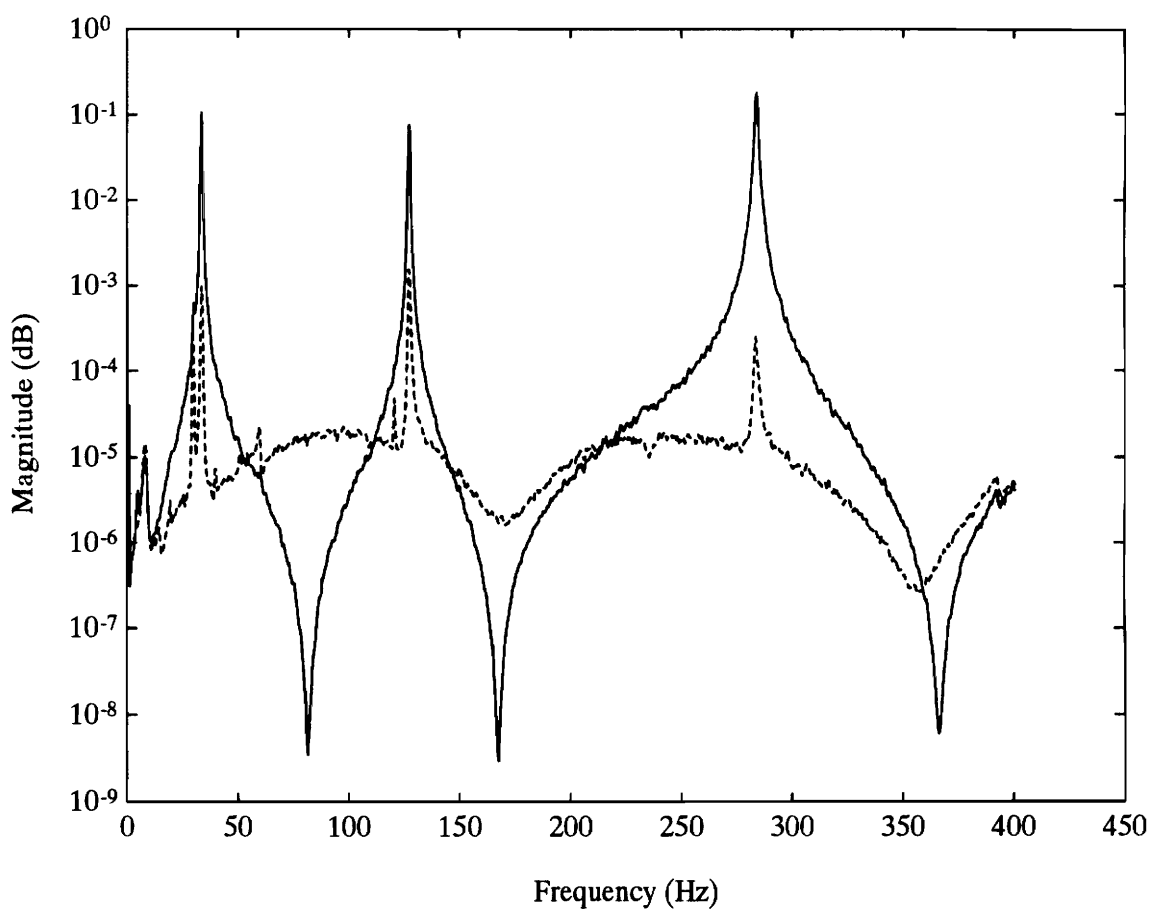ather than a true broadband controller, attenuating the larger frequency components that occur near the structural resonances, while adding energy at the off-resonance frequencies. The reader should keep in mind that the areas under the two curves can not be compared directly, because of the log scaling. Convergence of the adaptive algorithm occurred in approximately three seconds as shown by the time histories of the control and error signals in Figure 5.3.

The influence of the adaptive FIR filter size on the controller performance was then investigated by varying the filter order N, from 12 to 80 coefficients. This process was performed first for a causal control system. The reduction in the mean square error as function of the filter size is plotted in the top curve of Figure 5.4. It is seen that the control performance quickly improves with larger filters to reach a nearly constant reduction of 20 dB after 24 weights.

The programmable disturbance-path delay d was then set to zero to repeat the above experiments for an 'acausal' control system. More correctly stated, a causal filter was used to approximate an acausal optimal control filter solution. The results of these tests are shown by the bottom curve in Figure 5.4. The performance of the 'acausal' controller is severely compromised for small size adaptive filters compared with the causal controller. However, for larger filter size, the 'acausal' controller shows significant reduction of the MSE, which is only 3 dB below that of
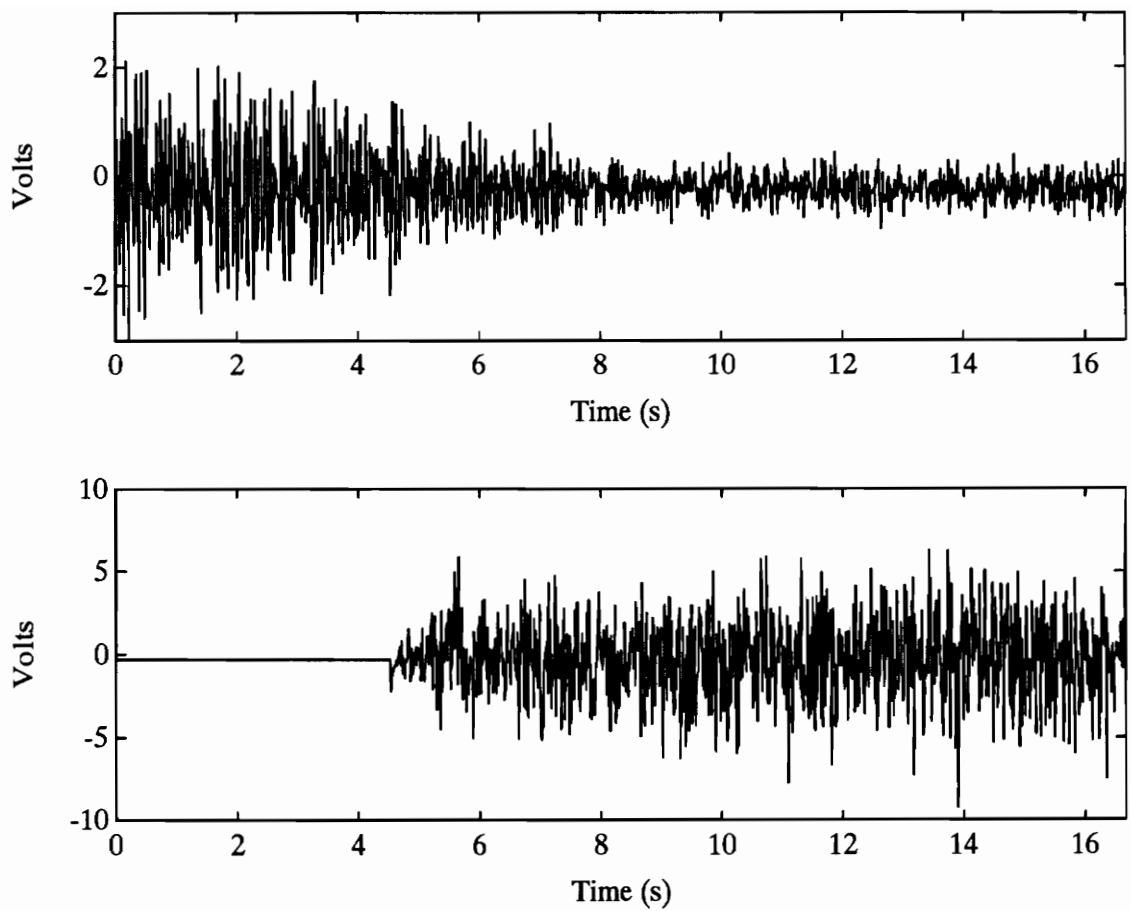
Figure 5.3: Time histories showing the convergence rate of the Conventional Filtered-X FIR adaptive controller. (top) error signal; (bottom) control signal.

75
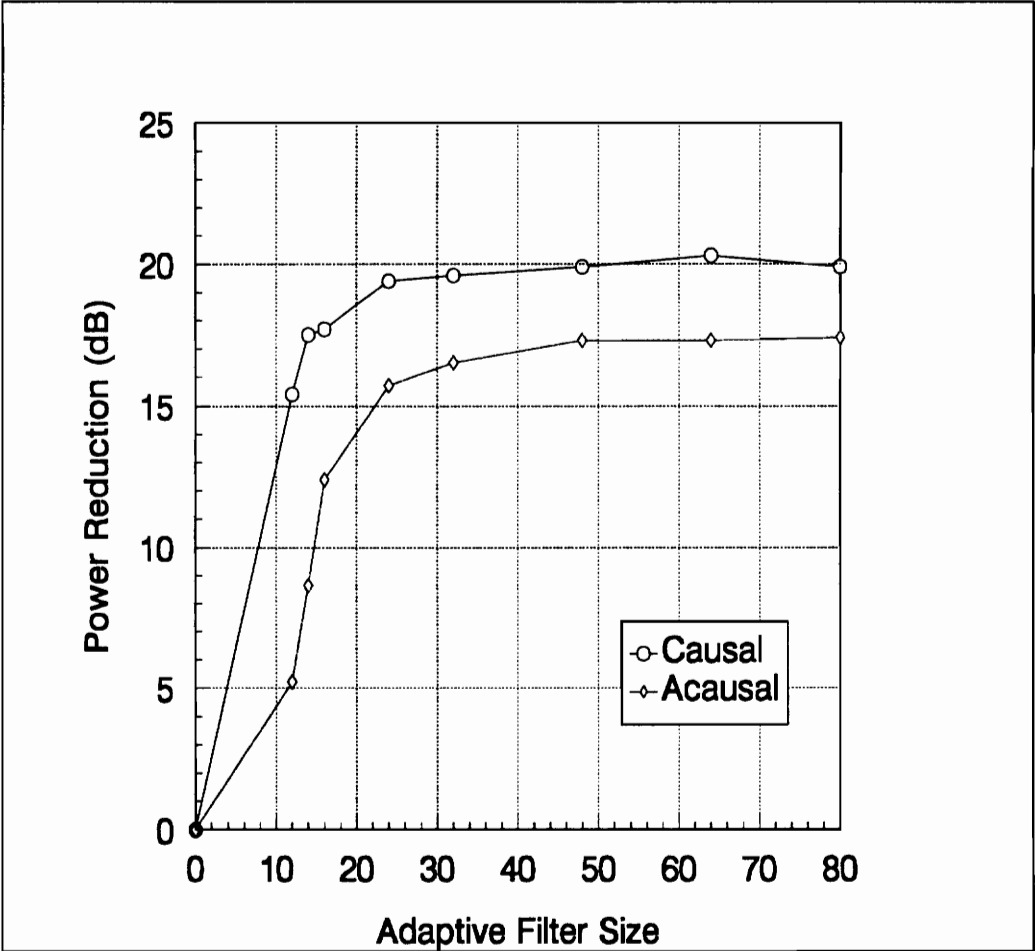
Figure 5.4: Performance of Filtered-X LMS FIR Controller as the adaptive filter size is increased.

.

the causal controller.

5.2 Equation Error Control Configuration with FIR

The Equation Error Control structure was demonstrated by performing two experiments with a causal control system having 24 adaptive coefficients. In the first test, the error signal was filtered with the same stabilized poles, $(1 - \hat{B}(z))$, used for the Conventional Filtered-X FIR Control in Section 5.1. This configuration did not produce as much reduction in the error signal as the Conventional Filtered-X LMS Control structure, nor did it converge as quickly. In Figure 5.5, a comparison of the error signal time histories before and after control is presented. The autospectra of the error signal were similar to Figure 5.2, where the modal amplitudes were reduced while some off-resonance frequency bands increased in energy. The plots are shown in Figure 5.6. A reduction of 10 dB in the power of the error signal was measured in this case. For the second control experiment, some of the poles of $(1 - \hat{B}(z))$ were reflected outside the unit circle before being used to filter the error signal with the Equation Error Configuration. This test demonstrates that a stable system identification of the control loop is not necessary for the Equation Error Control Configuration. Total power reduction of the error signal for the last experiment was approximately 8.9 dB, which differs slightly from the results of the first Equation Error Control experiment. Again, the before and after control error signals are compared as shown in Figure 5.7. Both of these experiments displayed much lower power reductions than the corresponding causal, 24th-order Conventional

77
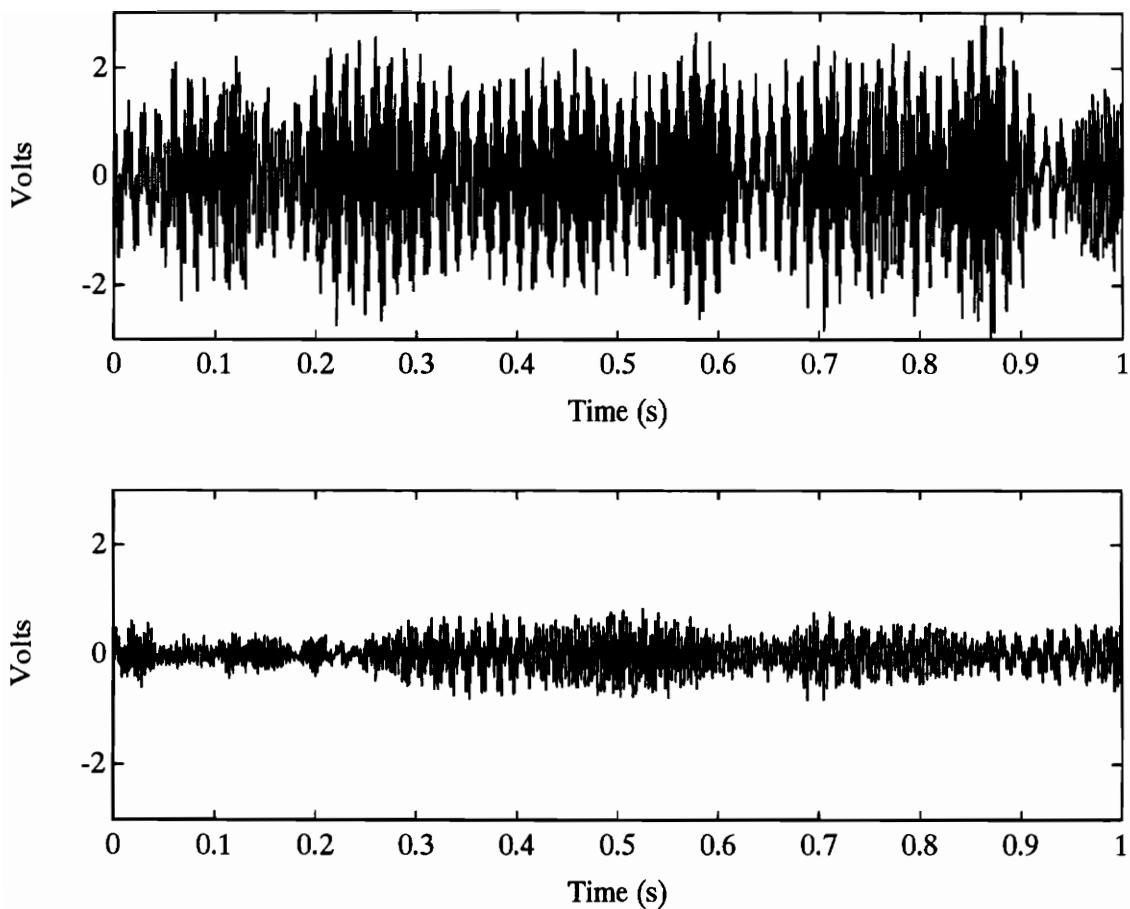
Figure 5.5: Actual error signal time histories during application of the Equation Error Control using an FIR. (top) without control; (bottom) after application of the Equation Error Control configuration.
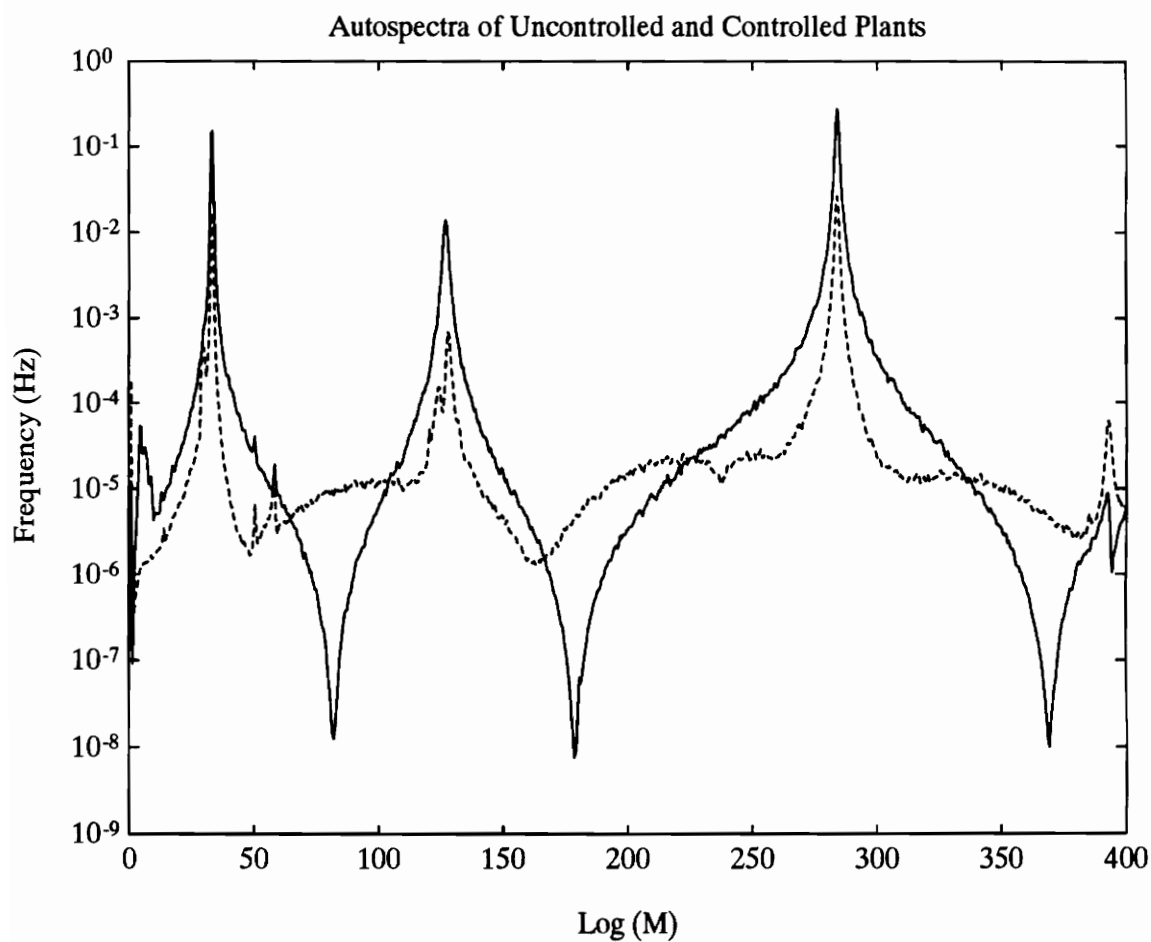
Figure 5.6: Autospectra of uncontrolled plant and Equation Error FIR control. ———
Uncontrolled; - - - - Controlled.
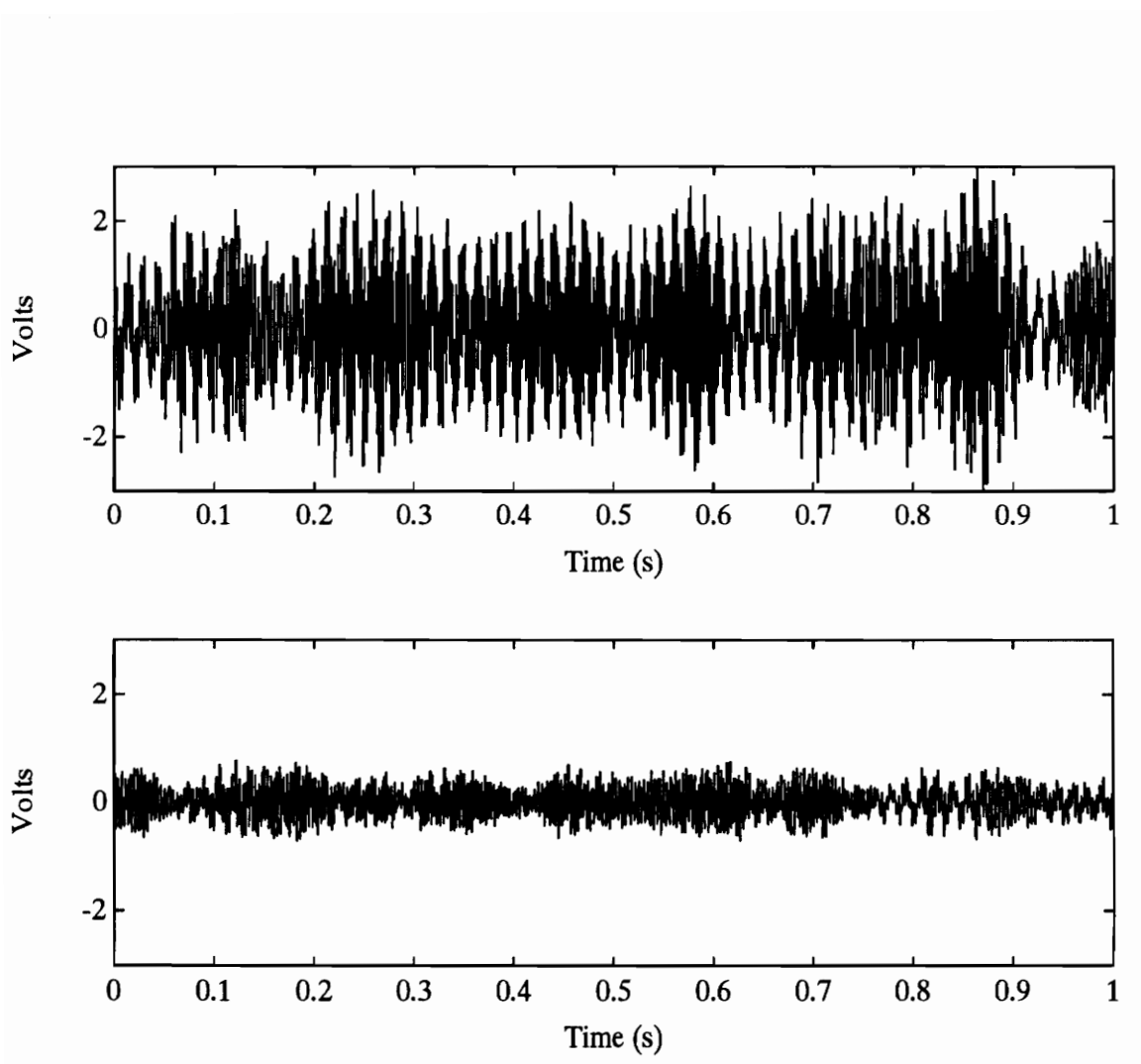
Figure 5.7: Error signal time histories showing effects of applying the Equation Error FIR Control form with unstable 'poles'. (top) without control; (bottom) after control convergence.

80

Filtered-X LMS Controller, which exhibited 20 dB of attenuation. However, the experiments demonstrate the advantage that a highly accurate system identification with stable poles is not necessary when using the Equation Error Control structure. The penalty for the relaxation on the system identification is a deterioration of the control performance. The difference between the results of the three test cases can be explained simply by the fact that a different cost function is minimized for all three test cases. Table 5.1 summarizes these test results.

Table 5.1: Comparison of Three Different Control Structures Having a 24th-Order Causal Adaptive FIR Filter

Control Configuration	Reduction (dB)
Conventional LMS Controller	19.4
Equation Error LMS Controller With Stable Poles	10.1
Equation Error LMS Controller With Unstable Poles	8.91

5.3 Conventional Filtered-X Control With IIR Compensator

In Figure 5.8 the time domain results of the Conventional IIR control are shown for an adaptive filter having 6 coefficients. Complete attenuation of the error signal did not occur as in the simulation. However, very good control was observed for much smaller adaptive filters. For example, the 6th-order adaptive filter produced over 13 dB of reduction. A comparison of the autospectra in Figure 5.9 shows that

81
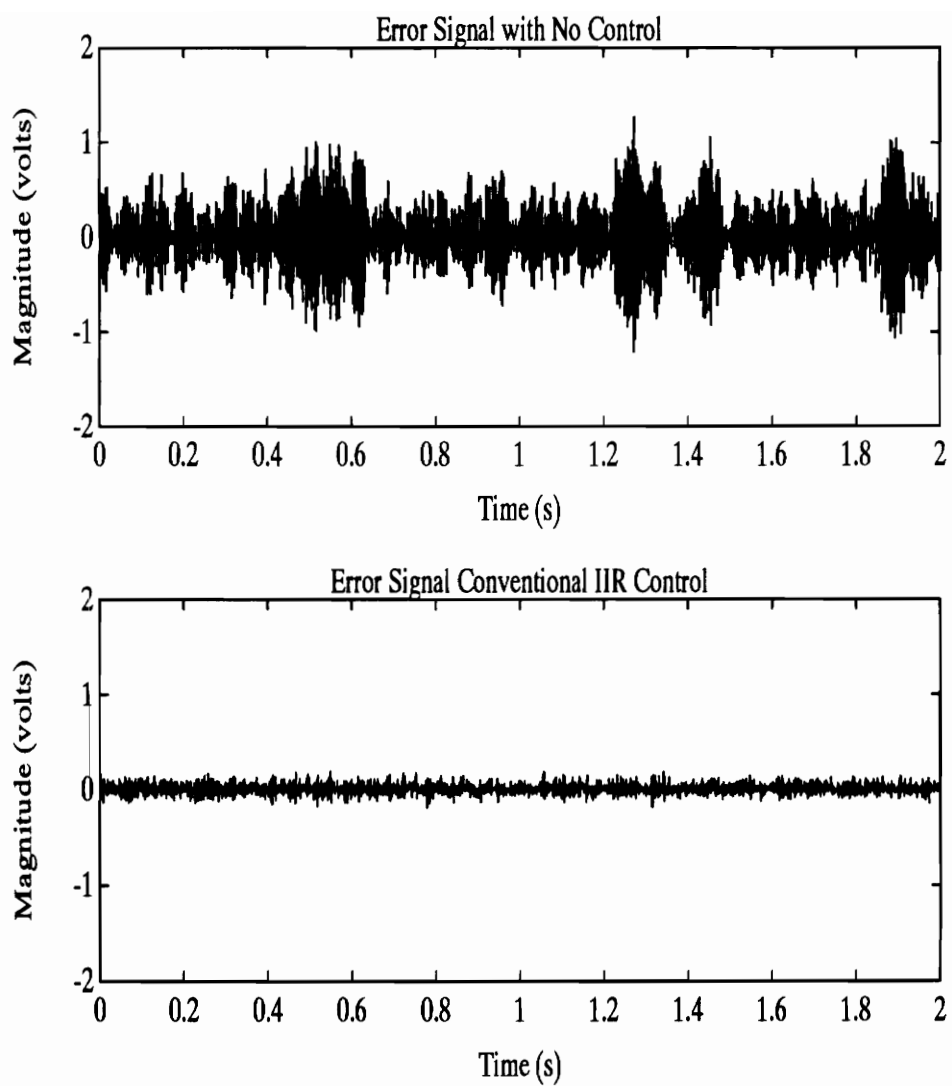
Figure 5.8: Measured error signal: (top) before control, and; (bottom) after convergence of the 6th-order Conventional Filtered-X IIR Control.

the recursive filter achieves more of a true broadband control, leaving the spectrum relatively flat after convergence. Note that this control system also increased the plant response at some of the off-resonance frequencies. The additional peaks at 16 and 44 Hz resulted from the interaction between the structure and the shaker used as a control actuator.

Last, the Conventional FIR control was applied to the same system (Configuration 2) in order to compare its performance with the recursive system. Figure 5.10 displays the control performance of both control systems for various adaptive filter sizes. As you can see, the conventional recursive filter performs much better than the FIR for small filter sizes, with comparable performance in the two systems occurring with a 16th order filter. Note that the IIR performance is nearly constant from a 4th order filter up to 16th order, where the FIR filter shows the familiar increasing asymptotic trend observed in the previous section. A noted disadvantage of the recursive filter is the very long convergence time, which is on the order of a few hours for each of the test cases. The nonrecursive system took longer to converge (15-30 minutes) than it did when applied to Configuration 1, presumably because of the removal of the low-pass filters.

5.4 Equation Error Filtered-X Control With IIR Compensator

As expected, the Equation Error Configuration was not as effective at minimizing the error signal as the conventional configuration when using the recursive compensator. About 7 dB of attenuation was observed for a 6th-order adaptive filter. The error

83
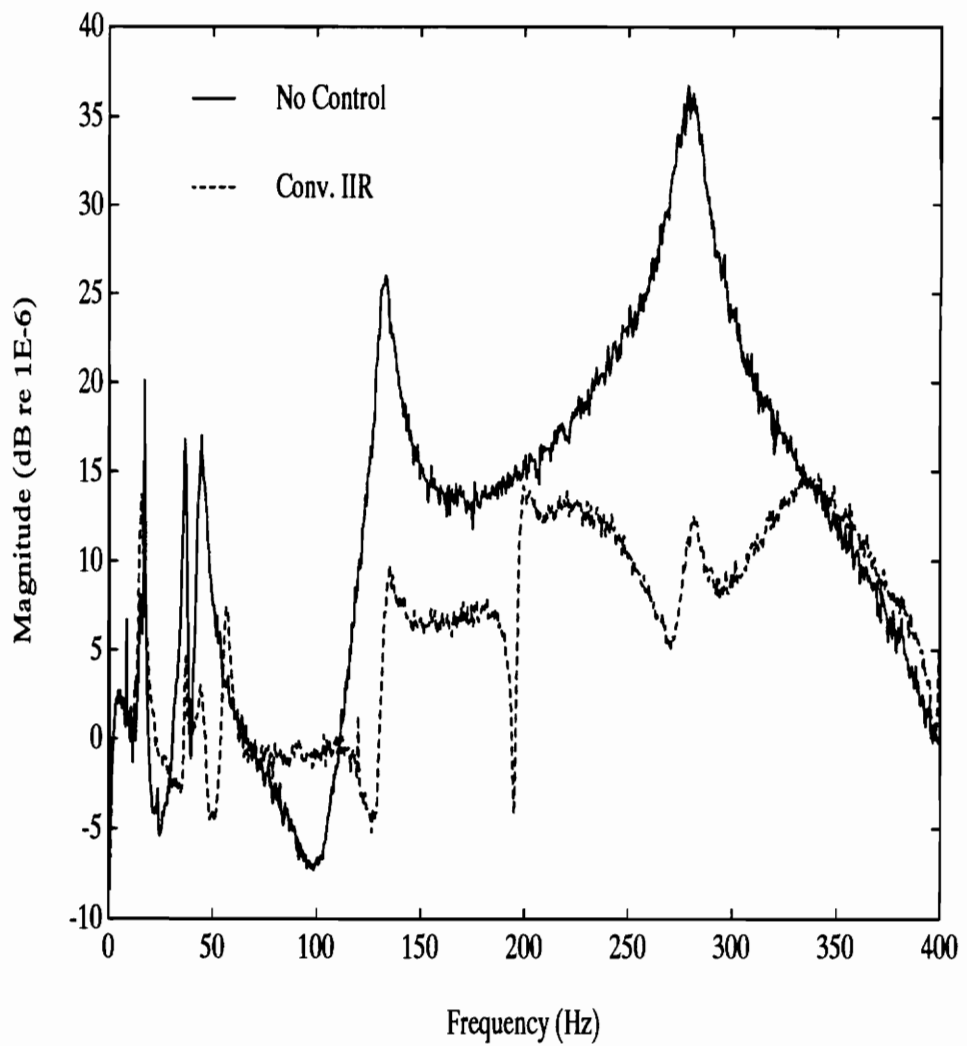
Figure 5.9: Frequency-domain representation of the error signal before control and after application of the Conventional IIR control using a 6th-order adaptive filter.
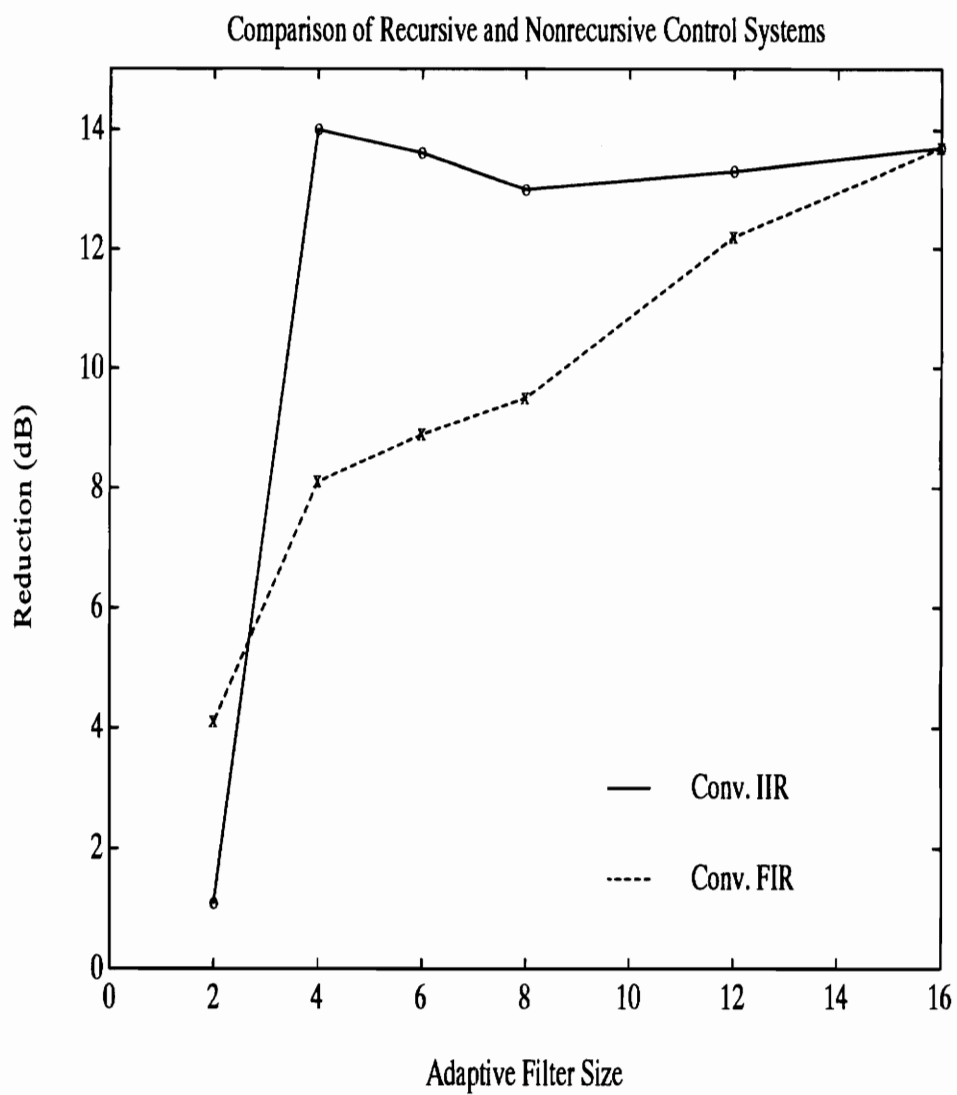
Figure 5.10: Experimental comparison of Conventional Filtered-X Control for: 1) an IIR compensator (Conv. IIR), and 2) an FIR compensator (Conv. FIR).

signal before and after control is shown in Figure 5.11. Figure 5.12 shows that the Equation Error IIR Control did not produce a flat spectrum unlike the Conventional Configuration. In fact, it looks similar to spectrum produced from the Conventional FIR Control.

Although the application of the recursive compensator is limited to only minimum-phase systems, the experiments demonstrate the potential for better control systems. This particular system has two advantages over the traditional RLMS filters: 1) the poles are not adapted and thus do not have to be checked for stability each time they are updated, and 2) no bias error is introduced as is the case for using an equation error minimization technique to adapt recursive filters.
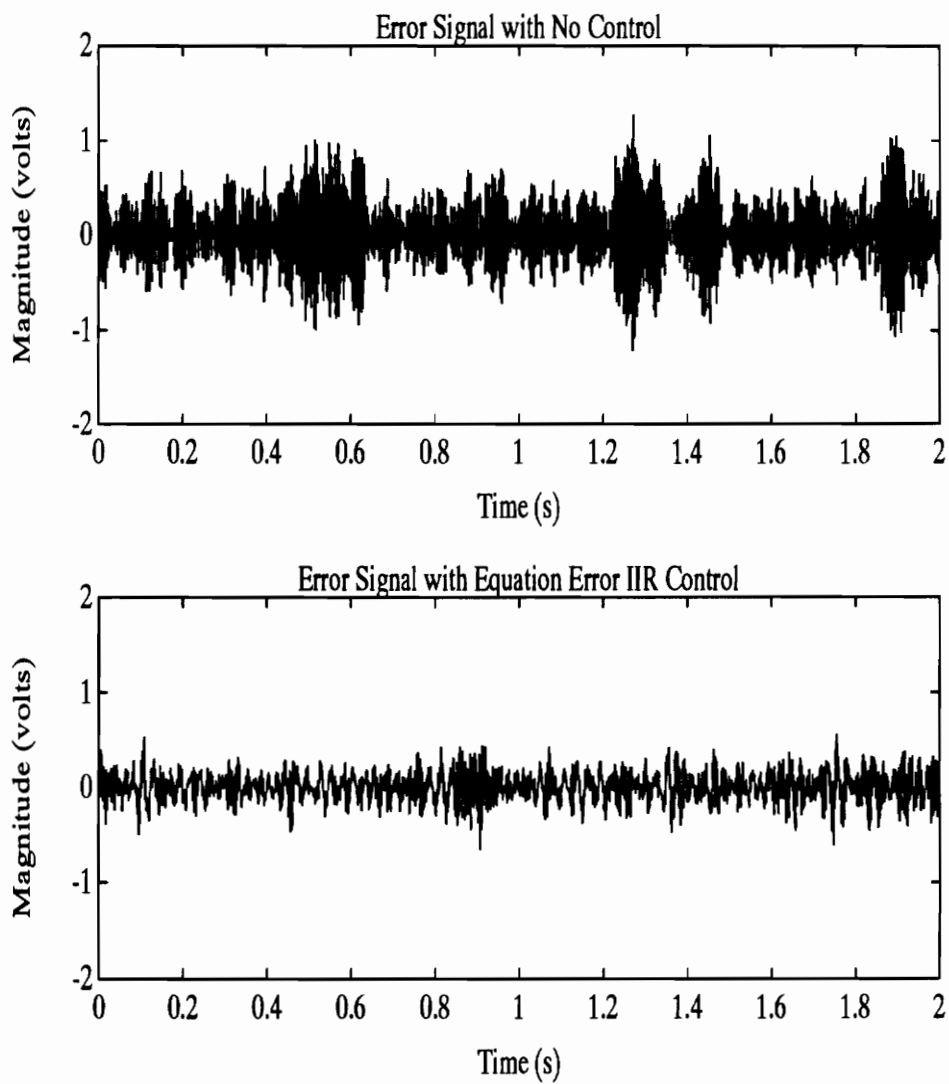
Figure 5.11: Error signal before and after applying Equation Error IIR Control.
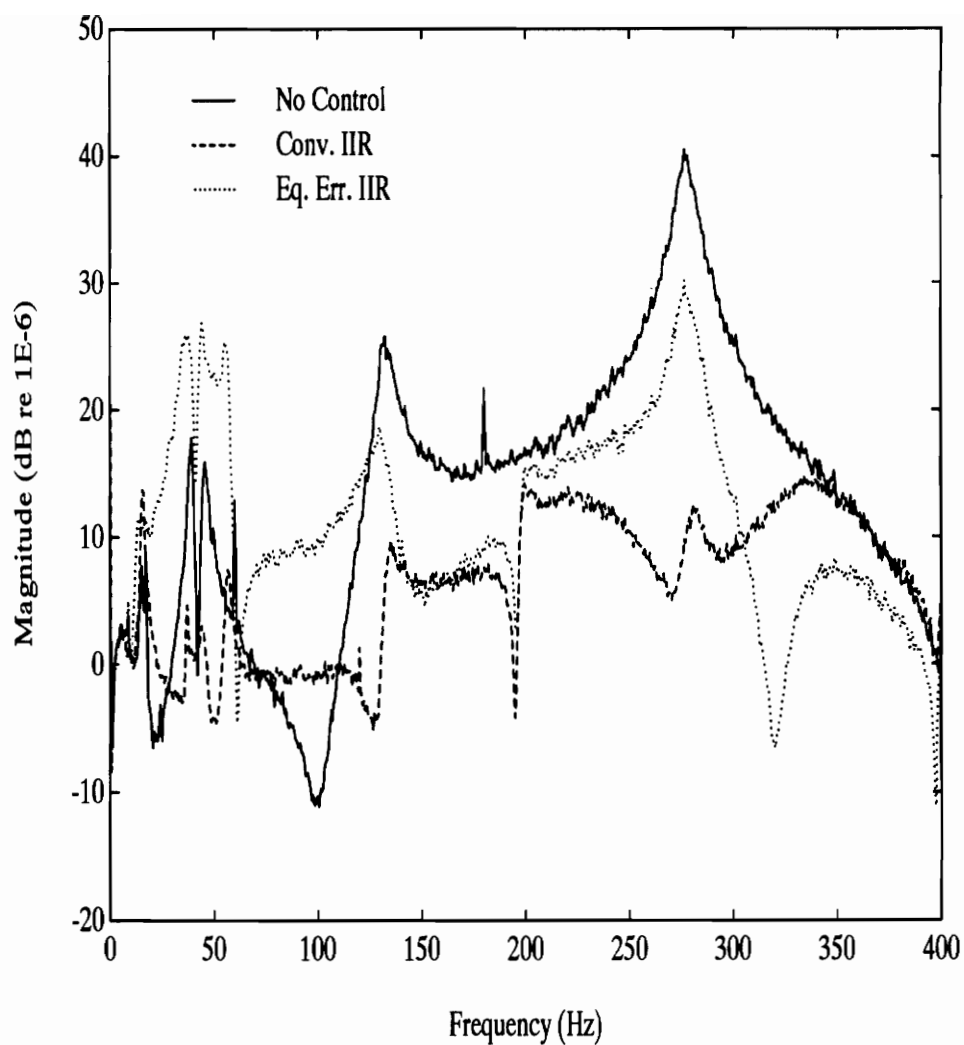
Figure 5.12: Autospectra of error signal for no control, Conventional IIR Control (Conv. IIR), and Equation Error IIR Control (Eq. Err. IIR).

Chapter 6

Analytical Study of System Causality

Previous literature discusses system causality for broadband feedforward control systems [16, 23]. The authors experimentally demonstrated that control system performance declines when delays are present in the control-path, rendering the optimal control filter acausal. For convenience, the complete *system* will be referred to as 'acausal' when, in actuality, the acausal optimal filter solution is being approximated with a causal compensator filter. In section 5.1, results of vibration control experiments using the Conventional Filtered-X LMS FIR Control showed about a 3 dB decrease in control system performance when a 2.7 ms delay was present in the control-path as compared to no delay. In the experiments, the disturbance signal was delayed to achieve the causal system since the 2.7 ms delay occurred naturally in the control loop [40]. The delays are dictated by the propagation times of the signal through each component of the control system, including the controlled plant. As seen in Figure 4.4, the control signal is delayed with respect to the disturbance signal in the experimental setup because of the sampling of the DSP and a larger

physical spacing between the actuator and error sensor. In addition, the low-pass smoothing filter provided a phase-shift in the control signal which cannot not be compensated for in the time-domain. Often systems can be made causal by simply decreasing the distance between the control actuator and error sensor, and if present, moving the reference sensor closer to the disturbance source.

The following analysis conducted on the Conventional Filtered-X LMS FIR Controller will exemplify that control is always achievable for any degree of 'acausality' in the optimal filter solution. A parametric study investigating filter order, system damping, and the delay time of the reference signal will be performed in order to provide better insight into the concept of causality and how it relates to broadband structural control. In addition, an attempt will be made to analytically predict the experimental observations shown in Figure 5.4 which relate system causality and adaptive filter size. Such an analysis will provide a tool to predict the degradation in performance of the control system for a given amount of system 'acausality' or control delay time. If desired, this analysis could be performed on the other three control structures as well.

6.1   Theory

We can study the effect of causality by adding a discrete delay, z^{-d}, into the control path as shown in Figure 6.1 where the pure delay is given by

$$z^{-d} \;=\; e^{-dt_s} \tag{6.1}$$

which provides a time delay of

$$\tau = dt_s \tag{6.2}$$

where

$$t_s = \text{sampling period of the digital delay}$$

When $d > 0$, the control system is said to be acausal because the signal through the control path trails behind the signal through the disturbance path. The control system can be made causal by selecting the delay $d = 0$, i.e. the disturbance takes the same time, in this ideal situation, to propagate through the control and disturbance paths. If $d < 0$, then the system is still causal, and a pure time delay will be needed in the control signal, which can be provided by additional filter taps.

The error signal can be written from Figure 6.1 as the superposition of the plant responses from both control and disturbance inputs as

$$e_k = d_k + y_k \tag{6.3}$$

Now, taking the z-transform of equation (6.3) and substituting the transfer functions from Figure 6.1

$$E(z) = [T_{ne}(z) + z^{-d}W(z)T_{ce}(z)]X(z) \tag{6.4}$$

In feedforward control, the optimum filter coefficients that define the control input signal are determined by minimizing the mean square value or variance of the plant output. The mean square value of e_k can be computed by a counterclockwise contour
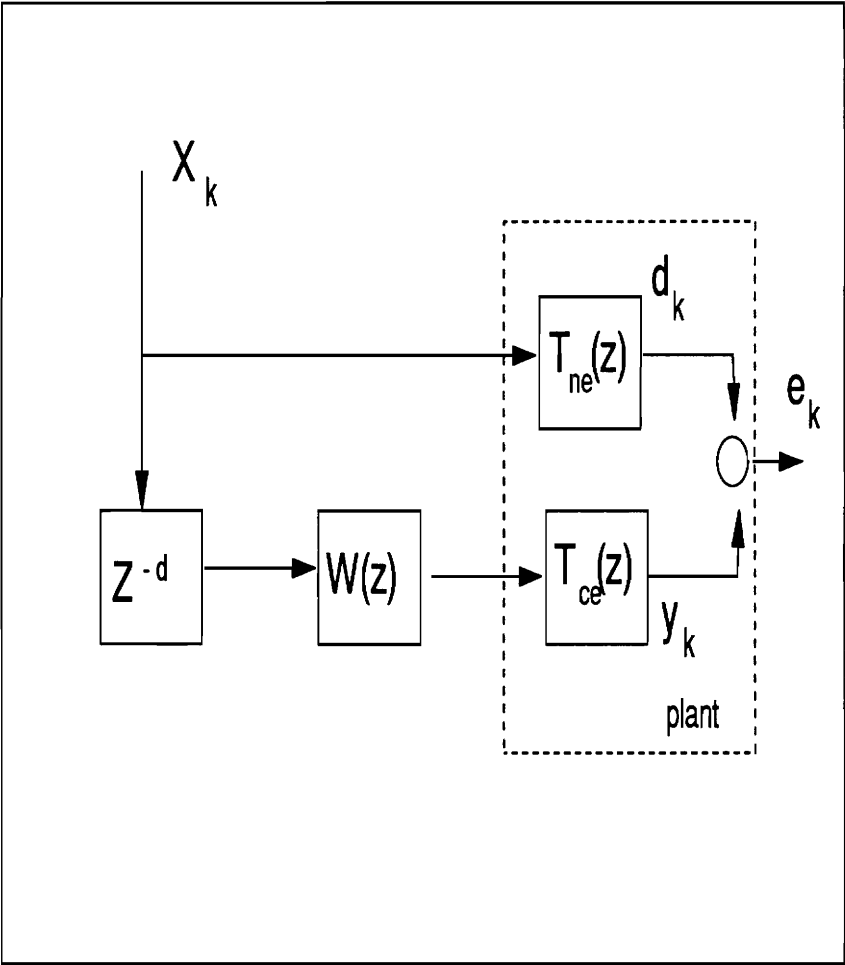
Figure 6.1: Block diagram of feedforward controller showing added delay in control path to make the system acausal.

integral around the unit circle in the complex z-plane as [17]

$$\sigma^2 = \frac{1}{2\pi j} \oint \Phi_{ee}(z) \frac{dz}{z} \qquad (6.5)$$

where

$\Phi_{ee}(z)$ = discrete power spectral density function (PSDF) of the error

sequence

The discrete Fourier transform of the PSDF in equation (6.5) can be found using
the relation [24]

$$z = e^{j\omega t_s} \qquad (6.6)$$

Using equation (6.6), the integral in equation (6.5) becomes

$$\sigma^2 = \frac{1}{2\pi} \int_{-\omega_{Ny}}^{\omega_{Ny}} \Phi_{ee}(e^{j\omega t_s}) d\omega \qquad (6.7)$$

where $\Phi_{ee}(\omega)$ is the error signal PSDF defined in the frequency domain, and ω_{Ny} is
the circular Nyquist frequency of the digital controller.

Again applying the transform of equation (6.6) to equation (6.4) gives the
frequency content of the sequence e_k as follows

$$e(\omega) = [T_{ne}(e^{j\omega t_s}) + e^{-j\omega t_s} \{W\}^T \{f\} T_{ce}(e^{j\omega t_s})] X(\omega) \qquad (6.8)$$

where

$$\{W\}^T = \{w_0, w_1, w_2, \ldots, w_L\} \qquad (6.9)$$

is the vector of filter coefficients, and

$$\{f\}^T \;\; = \;\; \{1, e^{-j\omega t_s}, \ldots, e^{-j\omega L t_s}\} \tag{6.10}$$

is known as the complex sinusoid vector in digital spectral analysis [18].

The power spectral density function of the error signal can be defined by

$$\Phi_{ee}(\omega) \;\; = \;\; \mathbf{E}[e(\omega)e(\omega)^*] \tag{6.11}$$

where * denotes the complex conjugate. Substituting equation (6.8) into (6.11) yields

$$\Phi_{ee}(\omega) \;\; = \;\; |[T_{ne}(e^{j\omega t_s}) + e^{-j\omega t_s}\{W\}^T\{f\}T_{ce}(e^{j\omega t_s})|^2 \Phi_{xx}(\omega) \tag{6.12}$$

Since the disturbance is a zero-mean white noise random process, the disturbance PSDF is a constant, $\Phi_{xx} = \Phi_o$. The mean square value of the error signal as a function of the filter weights, can now be computed by replacing equation (6.12) into (6.7), and expanding the complex modulus to yield

$$\sigma^2 \;\; = \;\; \sigma_d^2 + \{W\}^T[R]\{W\} + \{W\}^T(\{H\} + \{H\}^*) \tag{6.13}$$

where

$$\sigma_d^2 \;\; = \;\; \frac{1}{2\pi} \int_{-\omega_{Ny}}^{\omega_{Ny}} |T_{ne}(e^{j\omega t_s})|^2 \Phi_o d\omega \tag{6.14}$$

94

is the variance of the system response due to the disturbance input alone; matrix $[R]$ given by

$$[R] \;=\; \begin{bmatrix} R(0) & R(1) & R(2) & \cdots & R(L) \\ R(-1) & R(0) & R(1) & & \vdots \\ R(-2) & R(-1) & R(0) & & R(L) \\ \vdots & & & \ddots & R(1) \\ R(-L) & \cdots & & R(-1) & R(0) \end{bmatrix} \tag{6.15}$$

is a Hermitian Toeplitz matrix that is formed from the (L+1) coefficients

$$R(l) \;=\; \frac{1}{2\pi} \int_{-\omega_{N_y}}^{\omega_{N_y}} |T_{ce}(e^{j\omega t_s})|^2 e^{j\omega l t_s} \Phi_o d\omega \tag{6.16}$$

and the lth element of vector $\{H\}$ is given by

$$H(l) \;=\; \frac{1}{2\pi} \int_{-\omega_{N_y}}^{\omega_{N_y}} T_{ne}(e^{-j\omega t_s}) T_{ce}(e^{j\omega t_s}) e^{-j\omega(d+l)t_s} \Phi_o d\omega \tag{6.17}$$

Recall that the performance surface given by equation (6.13) is a quadratic function of the filter coefficients w_l and the optimum weights are those that minimize the error variance. Thus, differentiating equation (6.13) with respect to w_l and setting them to zero yields the following linear system of equations

$$[R]\{W\} \;=\; -\{H_r\} \tag{6.18}$$

where $\{H_r\}$ is the real part of the complex vector $\{H\}$.

Assuming matrix $[R]$ is nonsingular, solving for the optimum vector $\{W\}^*$ from equation (6.18), and replacing it back into equation (6.13) yields the minimum MSE

$$\sigma_{min}^2 \;=\; \sigma_d^2 - \{H_r\}^T [R]^{-1} \{H_r\} \tag{6.19}$$

The effectiveness of the control system can be measured by the performance ratio, defined by

$$\eta(dB) \quad = \quad 10\log\left(1 - \frac{\{H_r\}^T[R]^{-1}\{H_R\}}{\sigma_d^2}\right) \tag{6.20}$$

which gives the power reduction in decibels.

The minimum variance of the controlled output response is the difference between the variance due to the disturbance alone and the quadratic form $\{H_R\}[R]^{-1}\{H_r\}$. Thus, the control system performance will be completely determined by the properties of this quadratic form.

6.2 Control System Performance

A physical interpretation for the terms in matrix $[R]$ and vector $\{H\}$ can be derived by considering the two zero mean random processes depicted in Figure 6.2. The first process is the response of the system, d_k, when excited at the disturbance location by x_k (Figure 6.2 (a)), while the second process is the response of the system, y_k, when excited at the control location by the delayed sequence x_{k-d} (Figure 6.2 (b)). The term $R(l)$ represents the autocorrelation sequence of the response d_k as

$$R(l) \quad = \quad \mathbf{E}[d_k d_{k-l}] \tag{6.21}$$

$$R(l) \quad = \quad \frac{1}{2\pi}\int_{-\omega_{N_y}}^{\omega_{N_y}} \Phi_{dd}(\omega)e^{j\omega l t_s}\,d\omega \tag{6.22}$$
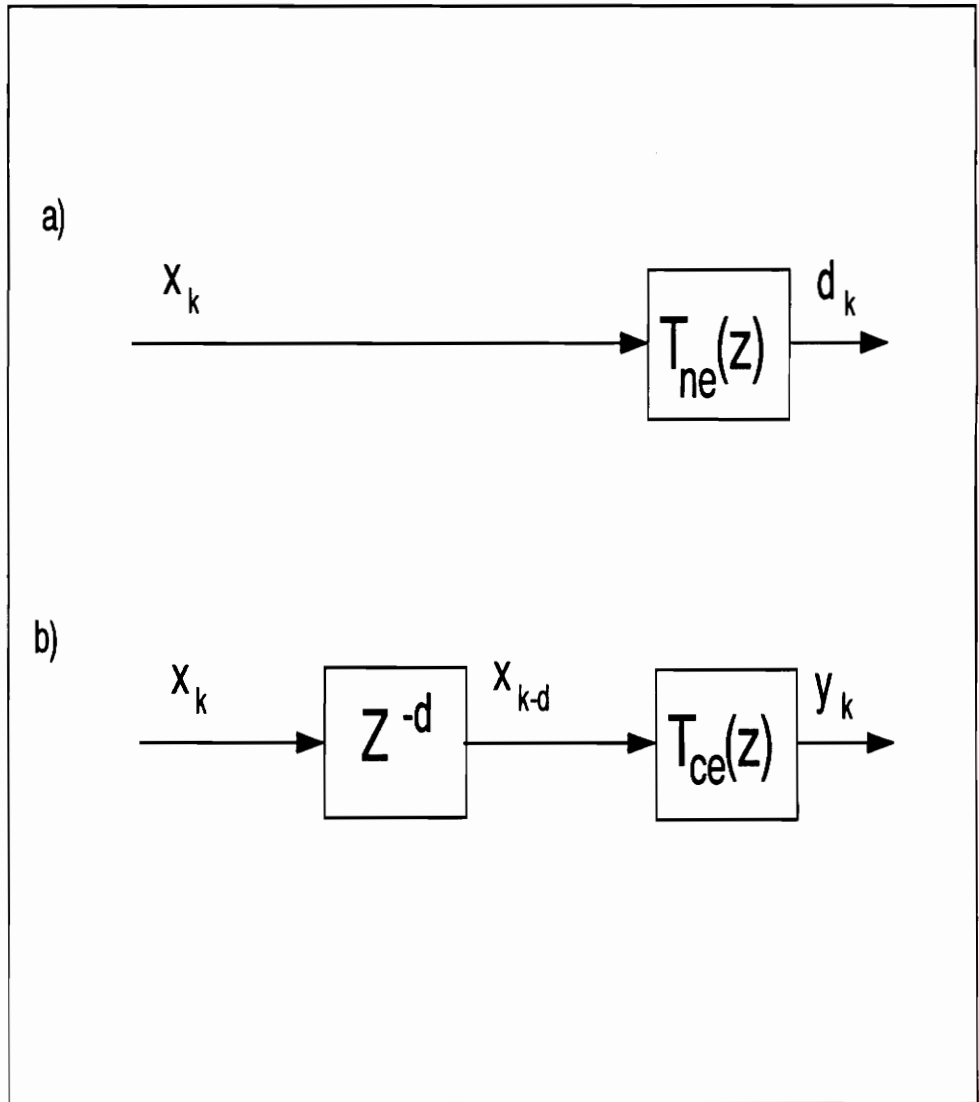
Figure 6.2: Diagram showing two Gaussian processes that comprise a feedforward broadband control system. a) Disturbance process; b) Control process.

where the PSDF in equation (6.22) is given in terms of the disturbance PSDF and the system dynamics as

$$\Phi_{dd}(\omega) \;=\; |T_{ne}(e^{j\omega t_s})|^2 \Phi_o \qquad (6.23)$$

Since the autocorrelation $R(l)$ is independent of the delay parameter d, the properties of the autocorrelation matrix of the random process d_k will also be independent of the control time delay. The properties of $[R]$ are a function of the system dynamics, through the control input and error output transfer function $T_{ce}(z)$, and the sampling period. Since the autocorrelation function of a real stationary random process is an even function $R(l) = R(-l)$, that renders matrix $[R]$ to be real and symmetric. Because of the nonnegative-definite property of the autocorrelation function, the autocorrelation matrix is positive semi-definite. That is $\{a\}^T[R]\{a\} \geq 0$ for any arbitrary $(L+1)$ vector $\{a\}$.

The term $H(l)$ in equation (6.17) represents the crosscorrelation sequence between the random processes d_k and y_k. as follows

$$H(l) \;=\; \mathbf{E}[d_k y_{k-l-d}] \qquad (6.24)$$

$$= \; \frac{1}{2\pi} \int_{-\omega_{N_y}}^{\omega_{N_y}} \Phi_{dy}(\omega) e^{j\omega(l+d)t_s} d\omega \qquad (6.25)$$

where the cross PSDF in equation (6.25) is given by

$$\Phi_{dy}(\omega) \;=\; T_{ne}(e^{-j\omega t_s}) T_{ce}(e^{j\omega t_s}) \Phi_o \qquad (6.26)$$

Unlike the autocorrelation, the crosscorrelation sequence of a real random process is a complex variable. From equation (6.26), $H(l)$ is a function of the system dynamics

through the transfer functions $T_{ne}(z)$ and $T_{ce}(z)$, the selected sampling frequency and the control path time delay $\tau = dt_s$. To graphically illustrate the dependance of $H(l)$ with the delay parameter, d, the real part of the crosscorrelation sequence is plotted in Figure 6.3 as a continuous line for a causal system by setting $d = 0$. Assuming the control path has a delay, d, the crosscorrelation sequence for the acausal system is the same crosscorrelation of the causal system shifted towards the left as shown in Figure 6.3 in dashed lines.

The previous analysis relinquishes very limited qualitative information of the controlled system behavior. To gain further insight into the controller performance, we consider the special case of sinusoidal random process. In this process, the white noise random sequence is approximated as the sum of M real sinusoids as

$$x_k = \sum_{m=1}^{M} A_M \sin(\omega_m k t_s + \theta_m) \tag{6.27}$$

where A_m is the real amplitude of the mth sinusoid of circular frequency ω_m, and the associated phase θ_m is a uniformly distributed random variable on the interval 0 to 2π. The amplitude A_m is related to the magnitude of the PSDF at frequency ω_m. The number and frequency of the sinusoids can be arbitrary. For the sake of clarity in the presentation, we select a uniform distribution for the sinusoid frequencies as $\omega_m = m\delta\omega$ that results in $A_m = 2\sqrt{\Phi_o \delta\omega}$. In the limiting case as $M \to \infty$ and $\delta\omega \to 0$, the sequence in equation (6.27) will be a true white noise random sequence.

Replacing equation (6.27) into the processes described in Figure 6.2, it is not
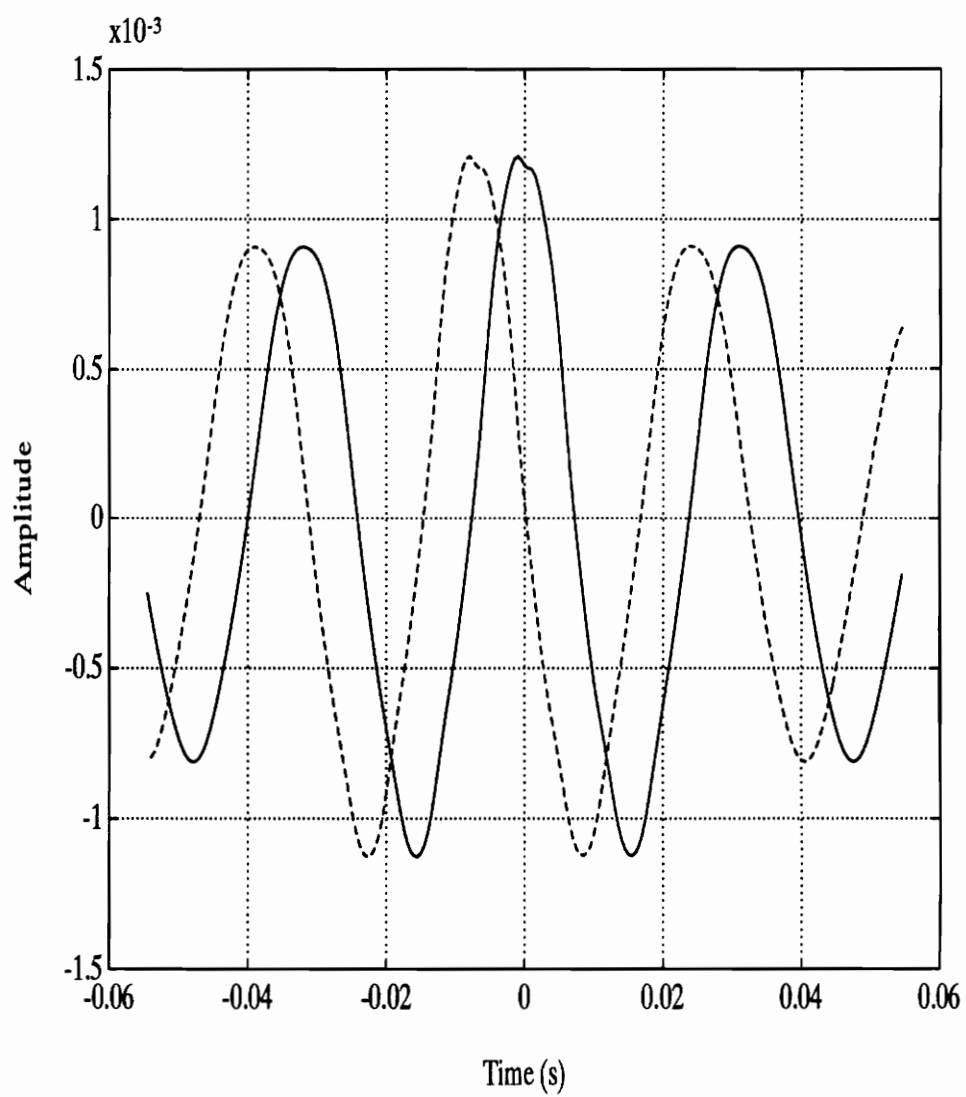
Figure 6.3: Crosscorrelation functions between disturbance and control responses: (———) for a causal system; (- - - -) for an acausal system.

difficult to show that the responses are also the summation of M sinusoids as

$$d_k = \sum_{m=1}^{M} D(k)_m \sin(\omega_m k t_s + \phi_m + \theta_m) \qquad (6.28)$$

and

$$y_k = \sum_{m=1}^{M} Y(k)_m \sin(\omega_m k t_s + \gamma_m + \theta_m) \qquad (6.29)$$

where the magnitudes of the sinusoids are

$$D(k)_m = = 2\sqrt{\Phi_o \delta\omega} |T_{ne}(\omega_m)| \qquad (6.30)$$

$$Y(k)_m = = 2\sqrt{\Phi_o \delta\omega} |T_{ne}(\omega_m)| \qquad (6.31)$$

and the phase shift of the sinusoids ϕ_m and γ_m are the phase of the transfer function $T_{ne}(\omega_m)$ and $T_{ce}(\omega_m)$ at frequency ω_m, respectively.

The autocorrelation sequence of this sinusoidal process can be easily computed in closed form as

$$R(l) = \Phi_o \delta\omega \sum_{m=1}^{M} |T_{ce}(\omega_m)|^2 \cos(\omega_m l t_s) \qquad (6.32)$$

and the associated autocorrelation matrix becomes

$$[R] = \Phi_o \delta\omega \sum_{m=1}^{M} |T_{ce}(\omega_m)|^2 \{S_m\}\{S_m\}^T \qquad (6.33)$$

where $\{S_m\}$ is

$$\{S_m\}^T = \{1, \cos(\omega_m t_s), \cos(2\omega_m t_s), \ldots, \cos(L\omega_m t_s)\} \qquad (6.34)$$

Again, the autocorrelation matrix $[R]$ is real, symmetric and in general, pos-

101

itive semi-definite, or in other words the eigenvalues of matrix $[R]$ are real and nonnegative. The rank of the autocorrelation matrix can be shown to be $2M$. Two cases can be investigated concerning the matrix $[R]$ dimension that it also is the filter size $(L + 1)$. If $(L + 1)$ is smaller or equal to $2M$, the eigenvalues of $[R]$ are all real and positive and matrix inverse in equation (6.19) exists. If $(L + 1)$ is greater than $2M$, there will be $(L + 1) - 2M$ zero eigenvalues and matrix $[R]$ is singular. A physical interpretation can be gained by considering the limiting case of $(L + 1) = 2M$, the number of coefficients in the filter is twice the number of sinusoids included in the process. Thus, there are enough coefficients to adjust the phase and magnitude of each tone to drive the output variance to zero, $(\sigma_{min}^2 = 0)$. Clearly, by increasing the filter size no further reduction can be achieved and this is mathematically depicted by the rank of $[R]$ to be $2M$. For the case of $(L+1) < 2M$, the positive definite property of $[R]$ and of its inverse allows us to write

$$\{H_r\}^T [R]^{-1} \{H_r\} > 0 \tag{6.35}$$

for any arbitrary vector, $\{H_r\}$, which has the important implication that there will always be some degree of reduction in the output variance in equation (6.19) in spite of any delay in the control path. Because of the positive definite property, it is not difficult to show that the quadratic form in equation (6.35) is a monotonically increasing function. That is,

$$(\{H_r\}^T [R]^{-1} \{H_r\})_{L+1} > \{H_r\}^T [R]^{-1} \{H_r\})_L \tag{6.36}$$

Therefore, the deterioration in the control performance due to the time delay could at least be partially compensated for by increasing the filter size. This phenomenon was observed in both the numerical and experimental studies of causality.

6.3   Parametric Analysis

To analytically verify the measured results, a model of the experimental beam was derived by solving the eigenvalue problem for a simply supported beam. The flexural rigidity is EI=5.329 $N\text{--}m^2$ and mass per unit length m=0.626 kg/m that corresponds to the experimental beam properties. The system is assumed to have 0.2% damping in each mode, and only the first three modes are included in the response analysis. The well known natural frequencies and normalized mode shapes are given by

$$\omega_n^2 \;=\; \left(\frac{n\pi}{L}\right)^4 \frac{EI}{m} \qquad\qquad (6.37)$$

$$\Phi_n(x) \;=\; \sqrt{\frac{2}{mL}}\,\sin\left(\frac{n\pi x}{L}\right) \qquad\qquad (6.38)$$

The analytical natural frequencies were tabulated in table 2.1 and the first three frequencies agree within 4% with the experimentally measured ones given in table 4.1. These eigenproperties are used to compute the transfer functions $T_{ne}(z)$ and $T_{ce}(z)$ needed for the analysis. The derivation of these transfer functions is detailed in Appendix B.

The response of the beam for a 'causal' system is obtained by setting the delay parameter $d = 0$ in the analysis. The integrals in equations (6.14), (6.16), and (6.17) are numerically solved as described in Appendix B. The power reduction at the error sensor location computed from equation (6.20) is plotted in Figure 6.4 as a function of filter size. Similarly, the 'acausal' control system of the experiment is simulated by setting $d = 6$, $(\tau = 3ms)$ in the analysis. The power reduction is again plotted int Figure 6.4. The analytical prediction shows the same general trend
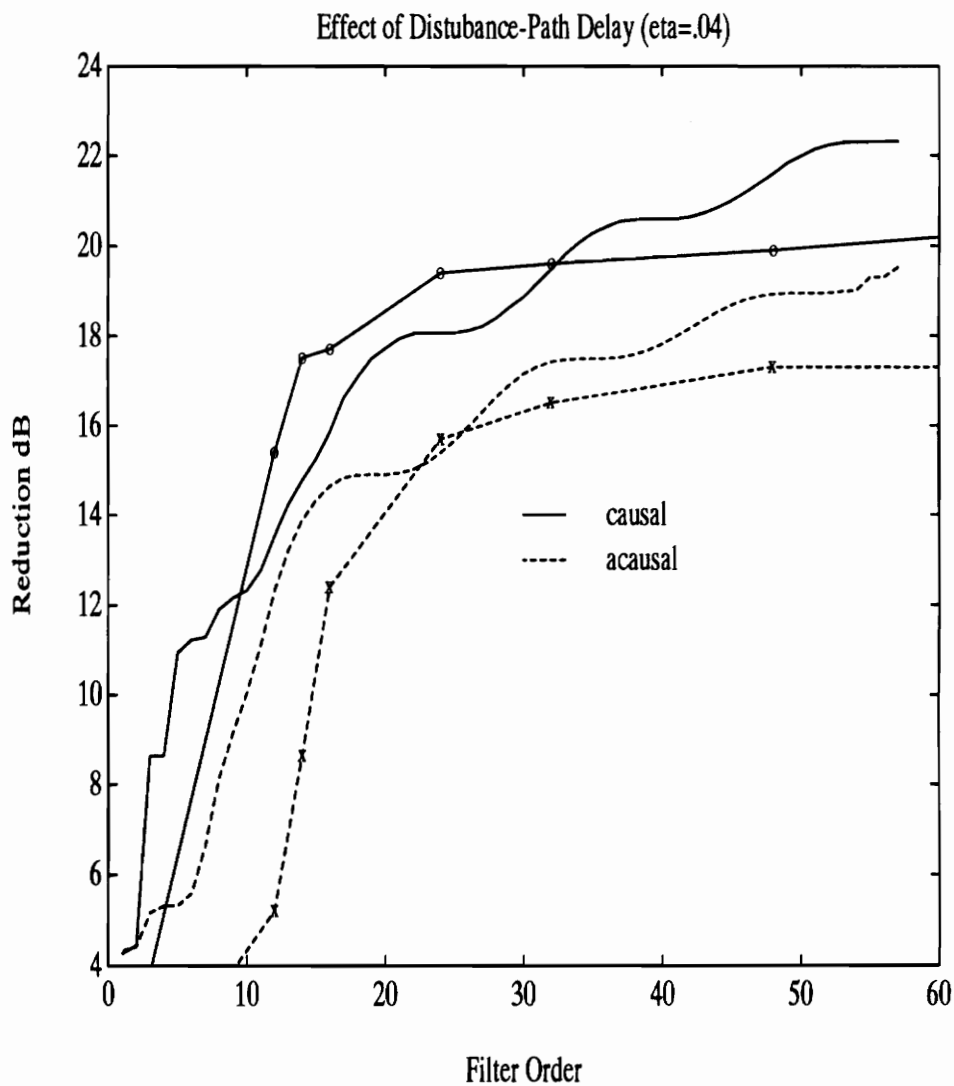
103

Figure 6.4: Analytical system performance as the order of the control compensator in increased for (——) causal system, and (- - - -) acausal system. The experimental observations are plotted with the symbols 'o' and 'x' for comparison.

as the experimental observations (also plotted in Figure 6.4) with two exceptions. Firstly, the analytical curves display some oscillation in the monotonically increasing performance function which is not observed from the experiments. The period of this oscillation is related to the period of the first natural mode of the beam, which dominates the response. Secondly, the analytical model displays better control for larger filter size than in the experimental observations. This probably due to the fact that the controller may not have completely converged at the time of the response measurement since larger filters require longer convergence times. However, the general agreement between the analytical and experimental results validates the proposed formulation as an analytical tool to predict control system performance.

The effect of system damping is investigated by increasing the uniform modal damping ratio β from 2% to 10%. As shown in Figure 6.5, less damping results in better attenuation of the error output variance. This behavior is due to the enhanced notch filtering effect of the structure that yields the response to resemble the superposition of multiple sinusoids whose frequencies are the natural frequencies of the structure. In the limiting case of the modal damping approaching zero, a filter with the number of coefficients equal to twice the number of modes to control would be sufficient to completely cancel the error signal. Figure 6.6 presents the parametric study of damping in an acausal system having delay of 3 ms ($d = 6$). The plot reflects the same general deterioration in control performance as system damping is increased.

A tool was developed to carry out causality analysis of feedforward controlled elastic systems subjected to broadband excitations. As an example, the analysis
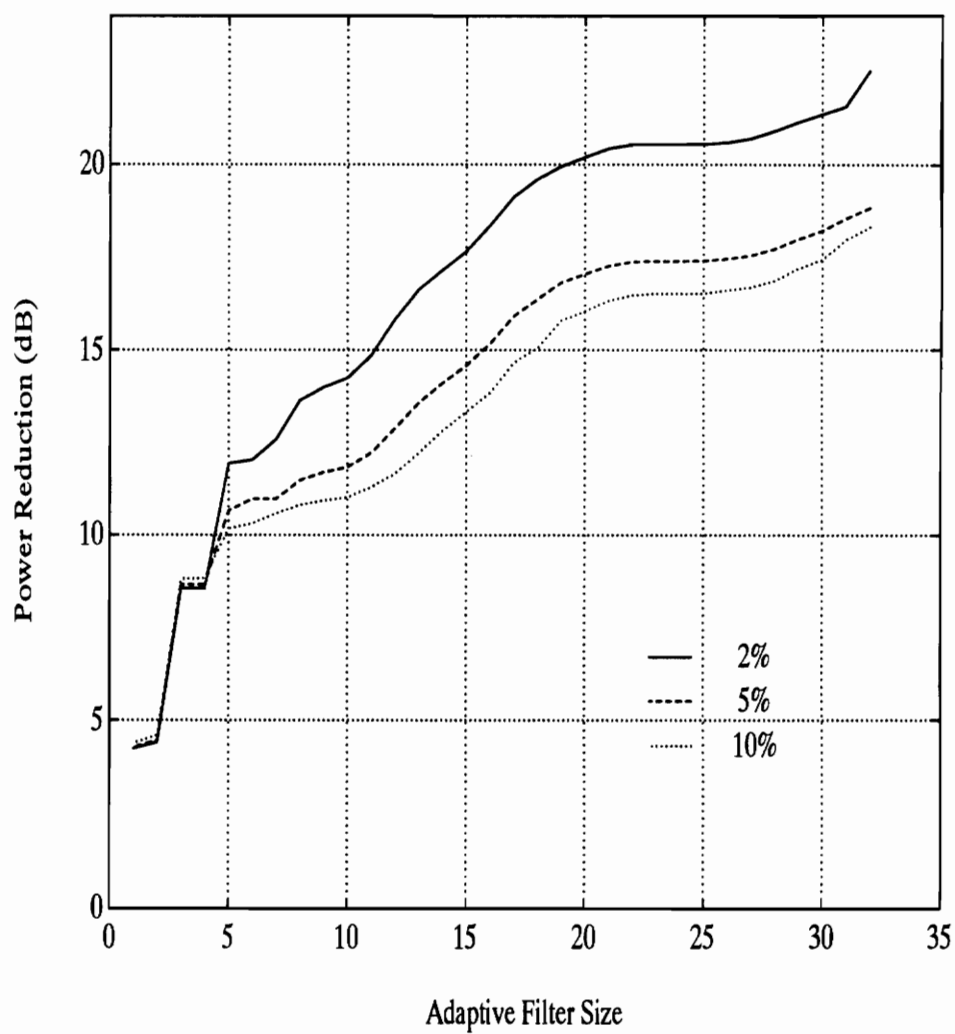
Figure 6.5: Plots of performance versus adaptive filter size comparing system damping of 2, 5, and 10 percent for a causal system.
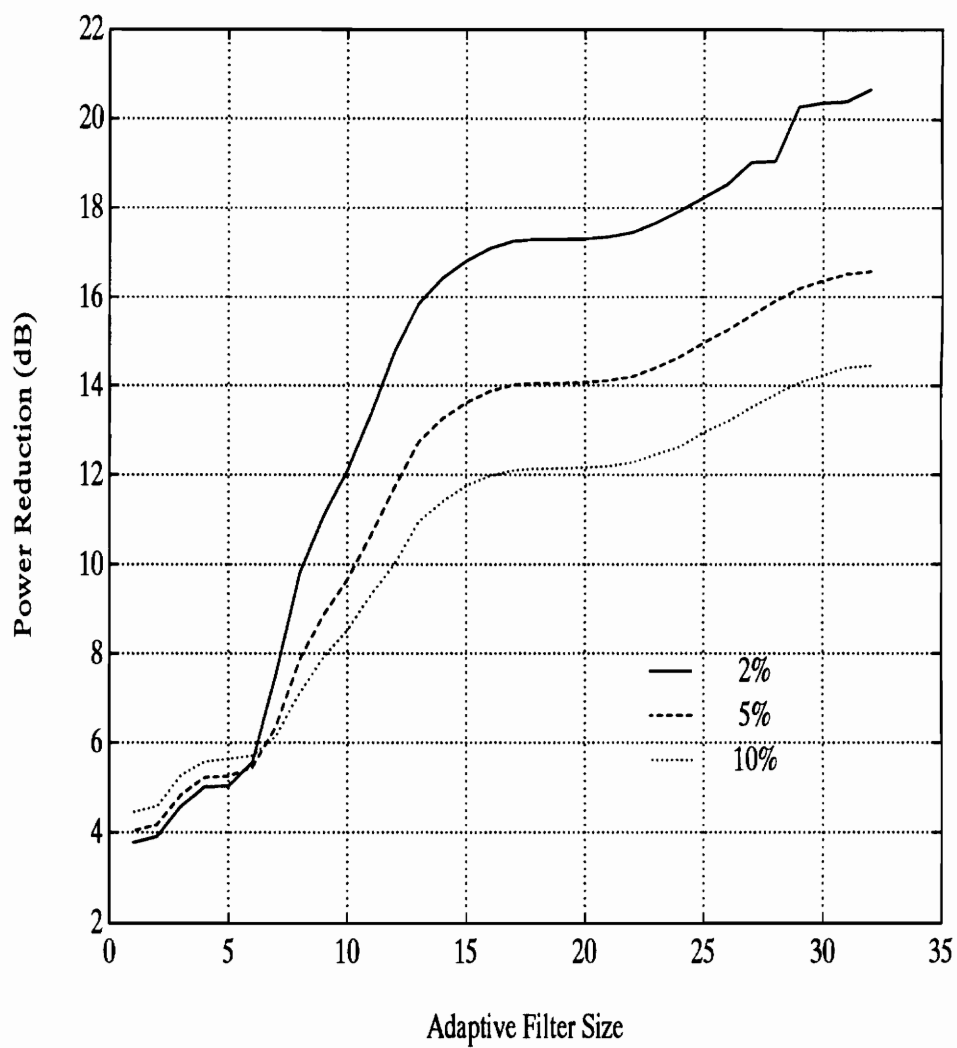
Figure 6.6: Plots of performance versus adaptive filter size comparing system damping of 2, 5, and 10 percent for a acausal system.

was carried out on the Conventional FIR Control applied to a simply-supported beam. The proposed analytical tool can be used to predict the performance of any of the feedforward control systems in terms of system parameters such as delay time, damping, filter size, etc. It is demonstrated that reduction in the error output variance is always achievable for any acausal control system. The analysis also shows that the deterioration in the control performance due to a delay in the control path can be at least partially compensated for by increasing the order of the compensator. The numerical results are also corroborated experimentally. Good agreement is observed between the numerically predicted and measured results, thus validating the proposed formulation.

Chapter 7

Conclusions and Recommendations

7.1   Conclusions

Four adaptive feedforward algorithms were developed for control of broadband response from finite structural systems. The algorithm uses an IIR filter to model the control loop transfer function between the control input and error sensor. The advantages and disadvantages of using a recursive or nonrecursive filter for the control compensator were addressed and demonstrated experimentally on a simply-supported beam. A variation of these two algorithms was developed which minimizes a filtered or equation error signal. These algorithms provided the advantage of not requiring a stable system identification of the control loop.

The effects of control system causality was addressed for finite, elastic structures. A model was developed which allows one to predict the system performance for various system damping ratios, adaptive filter sizes, and sample rates. The model

109

was verified experimentally.

The key conclusions from this research are:

1. Adaptive feedforward control of structural response resulting from broadband excitation is possible using the Filtered-X LMS control approach.

2. Control performance improves asymptotically as the order of the adaptive compensator is increased.

3. Large attenuations (up to 20 dB) were observed experimentally for adaptive FIR compensators which had 24 or more coefficients.

4. A new adaptive recursive approach was developed which uses fixed poles. The recursive approach provides better attenuation for small adaptive filters, but takes much longer to converge. It is also limited to use on nonminimum-phase plants.

5. Using an equation-error minimization approach provides the advantage of removing the need for a stable system identification of the control-loop, but sacrifices control performance.

6. An analytical tool was developed to investigate causality of feedforward control systems that are applied to elastic structures. It was concluded that any degree of acausality in the system will degrade performance, but this can be at least partially compensated for by increasing the compensator order.

7.2 Recommendations

In order to expand and improve this area of research, the following tasks are suggested:

1. Investigate applying the broadband controller to active structural-acoustic control (ASAC), to control broadband noise radiating from structures.

2. Analyze the error tolerance of the system identification to examine the required accuracy of the natural frequencies, damping, magnitudes, zero locations, etc., and how they influence the stability and convergence properties of each algorithm.

3. Develop a generalized recursive control approach that will work for any plant. Perhaps an artificial neural network (ANN) could be used to model the unstable inverse of a nonminimum-phase plant. One would not have constraints on filters, actuator/sensor locations, etc. as is the case when achieving a minimum-phase system.

4. Extend the control algorithms to multi-input, multi-output (MIMO) broadband control in order to achieve better global spatial reduction of the cost. This will be an arduous task, requiring much memory and computational overhead from the DSP.

5. Search for increased convergence performance both for the SISO and MIMO controllers. The very long convergence time which is characteristic of MIMO systems will be compounded by the fact that the adaptive compensators for

broadband control are much larger than ones used for harmonic control, increasing the time required for convergence. Possible suggestions are to use an intelligent first guess to the adaptive filter coefficients instead of adapting the coefficients from zero.

6. Repeat the causality analysis for the other three control algorithms and compare the results with a corresponding experimental investigation of them.

Bibliography

[1] L. Meirovitch and H. Baruh. Optimal control of damped flexible gyroscopic systems. *Journal of Guidance and Control*, 4:157–163, 1981.

[2] J. S. Burdess and A. V. Metcalfe. The active control of forced vibration produced by arbitrary disturbances. *Journal of Vibration, Acoustics, Stress, and Reliability in Design*, 107:33–37, 1985.

[3] S. Lee and A. Sinha. Design of an active vibration absorber. *Journal of Sound and Vibration*, 109:347–352, 1986.

[4] G. E. Warnaka. Active attenuation of noise: the state of the art. *Noise Control Engineering*, 18(3):100–110, 1982.

[5] R. J. Silcox and H. C. Lester. An evaluation of active noise control in a cylindrical shell. *Journal of Vibration Stress, and Reliability in Design*, 111:337–342, 1989.

[6] C. R. Fuller. Active control of sound radiation from a vibrating rectangular panel by sound sources and vibration inputs: an experimental comparison. *Journal of Sound and Vibration*, To be published.

[7] W. Redman–While, P. A. Nelson, and A. R. D. Curtis. Experiments on active control of flexural wave power. *Journal of Sound and Vibration*, 112(1):181–187, 1987.

[8] A. H. Von Flowtow and B. Schafer. Wave–absorbing controller for a flexible beam. *Journal of Guidance, Control, and Dynamics*, 9(6):673–680, 1986.

[9] S. J. Elliot, I. M. Stothers, and L. Billet. Adaptive feedforward control of flexural wave propagating in a beam. In *Proceedings of the Institute of Acoustics*, pages 613–622, 1990.

[10] J. Scheuren. Active attenuation of bending waves in beams. In *Proceedings of the Institute of Acoustics*, pages 623–629, 1990.

[11] G. P. Gibbs and C. R. Fuller. Experiments on active control of vibrational power flow using piezoceramics actuators and sensors. In *AIAA*, 1990.

[12] C. R. Fuller, G. P. Gibbs, and R. J. Silcox. Simultaneous active control of flexural and extensional power flow in beams. In *Proceedings of International Congress on Recent Developments in Air and Structure-borne Sound and Vibration, Auburn University, AL.*, pages 657–662, 1990.

[13] C. F. Ross. An algorithm for designing a broadband active sound control system. *Journal of Sound and Vibration*, 80(3):373–380, 1982.

[14] L. J. Erikson and M. C. Allie. A digital sound control system for use in turbulent flows. In *Noise–Con 87*, pages 365–370, 1987.

[15] L. J. Erikson, M. C. Allie, and R. A. Greiner. The selection and application of an iir adaptive filter for use in active sound attenuation. In *IEEE Transactions on Acoustics, Speech, and Signal Processing*, pages 433–437, 1987.

[16] J. V. Warner and R. J. Bernhard. Digital control of sound fields in three-dimensional enclosures. In *AIAA 11th Aeroacoustics Conference*, pages 1–8, 1987.

[17] B. J. Widrow and S. D. Stearns. *Adaptive Signal Processing*. Prentice–Hall, Englewood Cliffs, NJ 07632, 1985.

[18] S. Lawrence Marple Jr. *Digital Spectral Analysis With Applications*. Prentice–Hall, Englewood Cliffs, NJ 07632, 1987.

[19] P. L. Feintuch. An adaptive recursive lms filter. In *Proc. IEEE*, pages 1622–1624, 1976.

[20] J. R. Treichler, M. G. Larimore, and Jr. C. R. Johnson. Simple adaptive iir filtering. In *IEEE Transactions on Acoustics, Speech, and Signal Processing*, pages 118–122, 1978.

[21] L. J. Erikson and M. C. Allie. System considerations for adaptive modelling applied to active noise control. In *Proceedings ISCAS 88*, pages 2387–2390, 1988.

[22] J. V. Warner and R. J. Bernhardt. Digital control of local sound fields in an aircraft passenger compartment. *AIAA Journal*, 28(2):284–289, Feb 1990.

[23] T. J. Sutton, S. J. Elliot, P. A. Nelson, and I. Moore. Active control of multiple-source random sound in enclosures. In *Proceedings of the Institute of Acoustics*, pages 689–693, Southampton, 1990.

[24] A. V. Oppenheim and R. W. Schafer. *Digital Signal Processing*. Prentice–Hall, Inc., Englewood Cliffs, NJ 07632, 1975.

[25] P. A. Nelson, T. J. Sutton, and S. J. Elliot. Performance limits for the active control of random sound from multiple primary sources. In *Proc. IOA Spring Conference*, Southampton, 1990.

[26] B. J. Widrow, Jr. J. R. Glover, J. M. Mc Cool, J. Kaunitz, C. S. Williams, R. H. Hearn, J. R. Zeidler, Jr. E. Dong, and R. C. Goodlin. Adaptive noise cancelling: principles and applications. In *Proceedings of the IEEE*, pages 1692–1716, 1975.

[27] Scott D. Snyder. *A Fundamental Study of Active Noise Control System Design*. PhD thesis, University of Adelaide, Adelaide, South Australia 5001, 1991.

[28] Lynn A. Poole, Glenn E. Warnaka, and Richard C. Cutter. The implementation of the widrow-hoff algorithm for the adaptive cancellation of acoustic noise. In *Proceedings of IEEE*, 1984.

[29] R. A. David. A cascade structure for equation error minimization. In *Asilomar Conference on Circuits, Systems, & Computers, IEEE*, pages 182–186, 1982.

[30] S. J. Elliott, I. M. Stothers, and P. A. Nelson. A multiple error lms algorithm and its application to the active control of sound and vibration. In *IEEE Transactions on Acoustics Speech and Signal Processing*, pages 1423–1434, 1987.

[31] J. Ackermann. *Sampled-Data Control Systems*. Springer-Verlag, Berlin, Germany, 1985.

[32] B. C. Kuo. *Automatic Control Systems*. Prentice–Hall, Englewood Cliffs, NJ 07632, 1982.

[33] J. C. Burgess. Active adaptive sound control in a duct: a computer simulation. *Journal of Acoustical Society of America*, 70:715–726, 1981.

[34] L. J. Erikson and M. C. Allie. Use of random noise for on-line transducer modeling in an adaptive active attenuation system. *Journal of Acoustical Society of America*, 85(2):797–802, 1989.

[35] L. J. Erikson, M. C. Allie, C. D. Bremigan, and J. A. Gilbert. Active noise control of systems with time-varying sources and parameters. *Sound and Vibration*, 23(7):16–21, 1989.

[36] K. J. Åström, P. Hagander, and J. Sternby. Zeros of sampled systems. In *Proceedings of IEEE Conference on Decision and Control*, pages 1077–1081, Sweden, 1980.

[37] *PC–Matlab for MS–DOS Coputers*. The MathWorks, Inc., South Natick, MA 01760, February 1989.

[38] E. F. Crawley and J. de Luis. Use of piezoelectric actuators as elements of intelligent structures. *AIAA Journal*, 25(10):1373–1385, 1987.

[39] E. K. Demetriadis, C. R. Fuller, and C. A. Rogers. Piezoelectric actuators for distrubuted vibration excitaion of thin plates. *Journal of Vibration and Acoustics*, 113:100–113, 1991.

[40] J. S. Vipperman, R. A. Burdisso, and C. R. Fuller. Active control of broadband structural vibration using the lms adaptive algorithm. *Journal of Sound and Vibration*, Accepted for publication.

Appendix A

Simulation of Beam and Control Algorithms

As mentioned in section 6.3, solving the eigenvalue problem for a simply-supported beam in bending produced the following natural frequencies and normalized mode shapes

$$\omega_n^2 = \left(\frac{n\pi}{L}\right)^4 \frac{EI}{m} \tag{A.1}$$

$$\phi_n(x) = \sqrt{\frac{2}{mL}} \sin\left(\frac{n\pi x}{L}\right) \tag{A.2}$$

where

n = modal index

L = length of the beam

EI = bending stiffness of the beam = $5.329 \; N-m^2$

m = mass per unit length = $0.626 \; kg/m$

x = spatial coordinate along beam length

The transfer function of the beam between two points can be represented by

$$H(x, \omega) = \sum_{n=1}^{N} \mathbf{u}_n \epsilon_n H_n(\omega) \tag{A.3}$$

where

$$N = \text{number of modes} \tag{A.4}$$

$$\mathbf{u}_n = \frac{d\phi_n(x_{c2})}{dx} - \frac{d\phi_n(x_{c1})}{dx} \tag{A.5}$$

$$\epsilon_n = \phi_n(x_e) \tag{A.6}$$

$$H_n(w) = \frac{1}{\omega_n^2 - \omega^2 + 2j\zeta_n\omega\omega_n} \tag{A.7}$$

where the modal components for a piezo patch actuator are represented by $\mathbf{u}_n$, and the point-sensor modal components by ϵ_n, where x_{c2} and x_{c1} are the coordinates of the leading and trailing edge of the piezo patch. Taking the z-transform of the frequency response function in equation (A.7) yields the following discrete function

$$H_n(z) = \frac{b_{1,n}z^{-1}}{1 - a_{1,n}z^{-1} - a_{2,n}z^{-2}} \tag{A.8}$$

where

$$b_{1,n} = \exp(-\zeta_n\omega_n T)\frac{1}{\omega_n\sqrt{1 - \zeta_n^2}}\sin(\omega_n\sqrt{1 - \zeta_n^2}T) \tag{A.9}$$

$$a_{1,n} = 2\exp(-\zeta_n\omega_n T)\cos(\omega_n\sqrt{1 - \zeta_n^2}T) \tag{A.10}$$

$$a_{2,n} = \exp(-2\zeta_n\omega_n T) \tag{A.11}$$

where T is the discrete-time sample period. Equation (A.8) can now be substituted into equation (A.3) for $H_n(\omega)$ to obtain the discrete transfer function for the beam.

$$H(x, z) = \sum_{n=1}^{N} \mathbf{u}_n \epsilon_n H_n(z) \tag{A.12}$$

The second-order sections resulting from each mode, n, in equation (A.12) were then convolved to produce a rational transfer function of the form

$$H(z) = \frac{A(z)}{1 - B(z)} \tag{A.13}$$

where $A(z)$ and $B(z)$ are polynomials in the complex variable z. The appropriate values for x_{c1}, x_{c2}, and x_e from chapter 4 can be substituted into equations (A.5) and (A.6) to form the transfer functions $T_{ce}(z)$ and $T_{ne}(z)$. Filtering a white noise process with $T_{ne}(z)$ produced the plant response, d_k in Figure 2.5, to broadband excitation. Similarly the filtered-x signal can be formed by filtering the reference signal, the disturbance input in this case, by the transfer function $T_{ce}(z)$. It was assumed the estimate $\hat{T}_{ce}(z)$ used to create the filtered-x signal was exact. The simulation was carried out by performing the following sequence of events during each step through time, k: a) Compute control input, u_k from equation (2.38); b) filter u_k with $T_{ce}(z)$ to compute to control loop response to the control input, y_k in Figure 2.5; c) Sum the two plant responses, y_k and d_k to form the error signal; d) use the error signal in conjunction with the filtered-x signal to update the adaptive filter weights according to equation (2.46).

Appendix B

Integration of Linear System for Causality Analysis

The integrals in equations (6.14), (6.16), and (6.17) from page 94 do not have a closed form solution. A direct numerical integration poses some difficulties because of the peaked nature of the typical structural transfer functions and also due to the oscillatory behavior of the term $e^{j\omega lt_s}$ in equations (6.16) and (6.17). Here a detailed description is presented for the numerical evaluation of these integrals.

From Appendix A, it was seen that the transfer function between the control input and error sensor can be represented as follows

$$T_{ce}(z) = \sum_{n=1}^{N} \mathbf{u}_n \epsilon_n H_n(z) \tag{B.1}$$

where $\mathbf{u}_n$, ϵ_n, and $H_n(z)$ are given by equations (A.5) - (A.7) in Appendix A Solving for the roots of the denominator of equation (A.8), $H_n(z)$ can be written

$$H(z) = \sum_{n=1}^{N=3} \frac{b_{1,n}z^{-1}}{(z - z_n)(z - z_n^*)} \tag{B.2}$$

where the roots are

$$z_n = e^{-\zeta \omega_n t_s}[\cos(\sqrt{1 - \zeta_n^2}\omega_n t_s) + j\sqrt{1 - \cos^2(\sqrt{1 - \zeta_n^2}\omega_n t_s)}] \qquad \text{(B.3)}$$

The squared modulus of the transfer function $T_{ce}(z)$ is computed as

$$|T_{ce}(z)|^2 = |T_{ce}(z)T_{ce}(z^{-1})| \qquad \text{(B.4)}$$

$$|T_{ce}(z)|^2 = \sum_{n=1}^{N}\sum_{m=1}^{N} u_n u_m \epsilon_n \epsilon_m H_n(z)H_m(z^{-1}) \qquad \text{(B.5)}$$

where by replacing z by z^{-1} is equivalent to taking the complex conjugate in the frequency domain.

Replacing equation (B.2) into (B.5) and using partial fraction expansions, the product of the modal FRFs can be expanded as follows

$$H_n(z)H_m(z^{-1}) = \frac{A_{nm}}{z - z_n} + \frac{B_{nm}}{z - z_n^*} + \frac{C_{nm}}{z - \frac{1}{z_m}} + \frac{D_{nm}}{z - \frac{1}{z_m^*}} \qquad \text{(B.6)}$$

where the coefficients in the partial fractions are easily computed. Replacing equation (B.6) into (B.5) results in

$$R(l) = \frac{1}{2\pi}\sum_{n=1}^{N}\sum_{m=1}^{N} u_n u_m \epsilon_n \epsilon_m I_{nm}(l) \qquad \text{(B.7)}$$

where

$$I_{nm}(l) = A_{nm}\int_{-\omega_{Ny}}^{\omega_{Ny}} \frac{e^{j\omega l t_s}}{e^{j\omega t_s} - z_n}d\omega + B_{nm}\int_{-\omega_{Ny}}^{\omega_{Ny}} \frac{e^{j\omega l t_s}}{e^{j\omega t_s} - z_n}d\omega +$$

$$= C_{nm}\int_{-\omega_{Ny}}^{\omega_{Ny}} \frac{e^{j\omega l t_s}}{e^{j\omega t_s} - \frac{1}{z_m}}d\omega + D_{nm}\int_{-\omega_{Ny}}^{\omega_{Ny}} \frac{e^{j\omega l t_s}}{e^{j\omega t_s} - \frac{1}{z_m}}d\omega \qquad \text{(B.8)}$$

Now each integral in equation (B.7) is better conditioned than the original integral in equation (6.16). The numerical solution of the integrals in equation (B.7) does

not pose any problems for wide range of the parameters l and t_s.

Similarly, the integral of equation (6.14) becomes

$$\sigma_d^2 \;=\; \frac{1}{2\pi} \sum_{n=1}^{N} \sum_{m=1}^{N} \mathbf{f}_n \mathbf{f}_m \epsilon_n \epsilon_m I_{nm}(0) \tag{B.9}$$
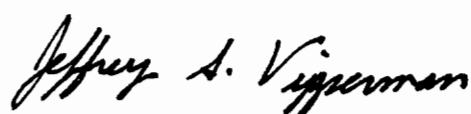
and equation (6.17)

$$H(l) \;=\; \frac{1}{2\pi} \sum_{n=1}^{N} \sum_{m=1}^{N} \mathbf{f}_n \mathbf{u}_m \epsilon_n \epsilon_m I_{nm}(d+l) \tag{B.10}$$

where the disturbance modal force vector is given by

$$\mathbf{f} \;=\; \frac{d\phi_n(x_{n2})}{dx} - \frac{d\phi_n(x_{n1})}{dx} \tag{B.11}$$

Vita

Jeffrey Stuart Vipperman was born March 12, 1968 in Lincoln, Nebraska. He completed undergraduate studies in mechanical engineering at Va. Tech. in August of 1990. During that period he worked part-time at Ingersoll-Rand in Roanoke, Va as a development engineering assistant. In addition, Jeffrey has performed undergraduate research in acoustics at Va. Tech. Following undergraduate school, a Master of Science was pursued and completed in June of 1992. He accepted a one-year position as a research associate at Va. Tech. upon completion of his M. S. degree.